

Universidade Federal de Juiz de Fora  
Engenharia Elétrica  
Programa de Pós-Graduação em Engenharia Elétrica

**Guilherme Ribeiro Colen**

**Resource Allocation and Time-Frequency Modulation for Power Line  
Communication**

Juiz de Fora

2016

**Guilherme Ribeiro Colen**

**Resource Allocation and Time-Frequency Modulation for Power Line  
Communication**

Tese de doutorado apresentada ao Programa de Pós-Graduação em Engenharia Elétrica da Universidade Federal de Juiz de Fora, na área de concentração em sistemas eletrônicos, como requisito parcial para obtenção do título de Doutor em Engenharia Elétrica.

Orientador: Moisés Vidal Ribeiro

Juiz de Fora

2016

Ficha catalográfica elaborada através do programa de geração automática da Biblioteca Universitária da UFJF, com os dados fornecidos pelo(a) autor(a)

Ribeiro Colen, Guilherme.

Resource allocation and time-frequency modulation for power line communication / Guilherme Ribeiro Colen. -- 2016.

111 f. : il.

Orientador: Moises Vidal Ribeiro

Tese (doutorado) - Universidade Federal de Juiz de Fora, Faculdade de Engenharia. Programa de Pós-Graduação em Engenharia Elétrica, 2016.

1. Comunicação via rede elétrica. 2. Alocação de recursos. 3. Multiplexação por divisão ortogonal na frequência. I. Vidal Ribeiro, Moises, orient. II. Título.

Guilherme Ribeiro Colen

Resource Allocation and Time-Frequency Modulation for Power Line  
Communication

Tese de doutorado apresentada ao Programa de Pós-Graduação em Engenharia Elétrica da Universidade Federal de Juiz de Fora, na área de concentração em sistemas eletrônicos, como requisito parcial para obtenção do título de Doutor em Engenharia Elétrica.

Aprovada em: 31 de março de 2016

BANCA EXAMINADORA



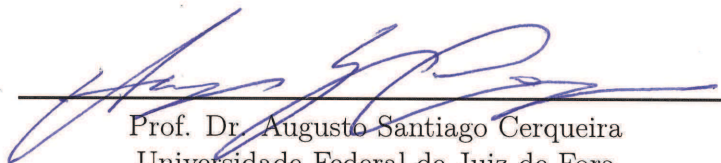
---

Prof. Dr. Moisés Vidal Ribeiro - Orientador  
Universidade Federal de Juiz de Fora



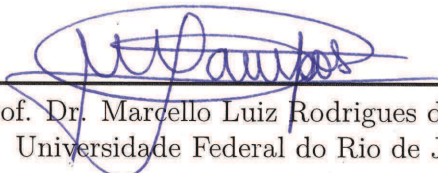
---

Prof. Dr. Carlos Augusto Duque  
Universidade Federal de Juiz de Fora



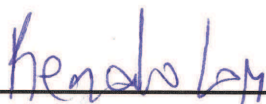
---

Prof. Dr. Augusto Santiago Cerqueira  
Universidade Federal de Juiz de Fora



---

Prof. Dr. Marcello Luiz Rodrigues de Campos  
Universidade Federal do Rio de Janeiro



---

Prof. Dr. Renato da Rocha Lopes  
Universidade Estadual de Campinas

*To my mother Angelina*

*To my father Eloi*

*To my sister Denise*

*To my wife Fernanda*

## ACKNOWLEDGMENTS

First of all, I thank God, for He has given me strength and courage to overcome all challenges that have come into my way ever since I started my doctorate. Second, I thank my parents, Eloi and Angelina, for all lessons they have taught me and for all support they gave me so I could go through my learning journey up to the doctorate. I am grateful to my sister Denise, for her support in many moments throughout my life. Particularly, I thank my beloved wife Fernanda, for her support and companionship during my entire doctorate, including the time we were in Germany, in which it was crucial. I should express my gratitude towards all my friends and family who supported me and were patient when I could not be present for having to concentrate on my studies.

I also thank my advisor, Professor Moisés, for all guidance from the end of my bachelor's course to the conclusion of my doctorate. Moreover, I am very grateful for the advice and knowledge he gave me over this period. Furthermore, I would like to thank Professor Han Vinck for having accepted me into his research group in Germany and for his many contributions to my work. I must thank the members of the doctoral examination board, who with wisdom analyzed, rated and contributed to the writing of this thesis. I should also thank all my colleagues at the laboratory, professors and workers at the university who contributed in any way to this work. Among these colleagues, I must mention and thank especially Lucas for his help, support and companionship during my stay in Germany and after my return to Brazil.

“A new idea comes suddenly and in a rather intuitive way.  
But intuition is nothing but the outcome of earlier intellectual experience.”

Albert Einstein

## RESUMO

Esta tese concentra-se na redução da complexidade computacional e na necessidade de largura de banda associada com a utilização de técnicas de alocação de recursos em sistemas de comunicação via rede elétrica (*power line communication* – PLC) com base no esquema de multiplexação por divisão ortogonal na frequência (*orthogonal frequency division multiplexing* – OFDM). Neste contexto, é introduzida a técnica sub-ótima chamada de *temporal compressive resource allocation* (TCRA). Esta técnica é capaz de explorar a relação existente entre *microslots* (exploração no domínio do tempo) para reduzir o número de vezes por segundo que alocação de recursos é executada. Além disso, é proposto um novo parâmetro, denominado de banda de coerência da relação sinal ruído normalizada (*normalized signal to noise ratio* – nSNR) para informar precisamente a planicidade da nSNR. A eficácia deste parâmetro é comparada com a banda de coerência. Diante disto, sua modelagem estatística para ambientes *in-home*, *outdoor* de baixa tensão e PLC-*wireless* é apresentada considerando distribuições de componentes individuais e misturas de Gaussianas. Com base na definição da banda de coerência da nSNR, é descrita a técnica sub-ótima denominada *spectral compressive resource allocation* (SCRA). Ela explora a relação existente entre os sub-canais adjacentes (exploração no domínio da frequência) para reduzir a dimensão do vector de nSNR, que é a principal informação de entrada para as técnicas de alocação de recursos. Com base no fato de que a geometria de *tiles* associadas com a transformada de Fourier discreta limita os ganhos associados com o uso da técnica SCRA em conjunto com o esquema OFDM, é introduzido pela primeira vez o esquema chamado multiplexação por divisão ortogonal no tempo-frequência (*orthogonal time-frequency division multiplexing* – OTFDM). Este esquema se baseia na transformada ortogonal de Stockwell discreta para oferecer diferentes geometrias de *tiles* e funciona tanto para comunicação de dados em banda de base quanto em banda passante. Os resultados numéricos baseados em canais PLC medidos e no uso de protótipo de transceptores PLC mostram que as técnicas TCRA e SCRA podem trocar redução de complexidade computacional por perda de taxa de transmissão e que economia de complexidade computacional relevante pode ser realizada com baixas perdas na taxa de transmissão. Ademais, os resultados numéricos mostram que o esquema OTFDM pode ser superado pelo esquema de OFDM se a informação de estado de canal não está disponível no lado do transmissor. No entanto, a disponibilidade de tais informações no lado do transmissor permite a utilização do esquema OTFDM em conjunto com a técnica SCRA atingir uma melhoria notável em comparação com o esquema OFDM trabalhando com a técnica SCRA.

Palavras-chave: Comunicação via rede elétrica. Alocação de recursos. Multiplexação por divisão ortogonal na frequência.

## ABSTRACT

This dissertation focuses on the computational complexity reduction and on the need for network bandwidth associated with the use of resource allocation techniques in power line communication (PLC) system based on orthogonal frequency division multiplexing (OFDM) scheme. In this context, the so-called temporal compressive resource allocation (TCRA) technique, which is a sub-optimal technique, is introduced. The TCRA is capable of exploiting the existing relationship among microslots (time domain exploitation) to reduce the number of times per second the resource allocation technique is executed. Also, a novel parameter, called nSNR coherence bandwidth, that precisely informs the flatness of the normalized signal to noise ratio (nSNR) is proposed. The effectiveness of this parameter is compared to the coherence bandwidth. Also, its statistical modeling for in-home, outdoor and low-voltage, and hybrid PLC-wireless channels with single-component and Gaussian mixture distributions is presented. Based on the nSNR coherence bandwidth definition, the spectral compressive resource allocation (SCRA) technique, which is a sub-optimal technique, is outlined. The SCRA technique exploits the existing relationship among adjacent subchannels (frequency domain exploitation) to reduce the dimensionality of the nSNR vector, which is the main feeding information for the resource allocation technique. Based on the fact that the geometry of the tiles associated with the discrete Fourier transform limits the gains associated with the use of the SCRA together with the OFDM scheme, the so-called orthogonal time-frequency division multiplexing (OTFDM) scheme is, for the first time, introduced. The OTDFM scheme, which is based on the discrete orthogonal Stockwell transform, offers different tile geometries and works in both baseband and passband data communications. Numerical results based on measured PLC channels and the use of prototype of PLC transceivers show that TCRA and SCRA techniques can trade computational complexity reduction with data rate loss and relevant computational complexity savings may be accomplished with low data rate losses. Moreover, the numerical results show that the OTFDM scheme may be outperformed by the OFDM scheme if channel state information is not available at the transmitter side; however, the availability of such information at the transmitter side allow the use of the OTFDM scheme together with the SCRA achieve remarkable improvement in comparison with OFDM scheme working with the SCRA technique.

Key-words: Power line Communication. Resource allocation techniques. Orthogonal frequency division multiplexing.

## LIST OF FIGURES

Figure 1 – Measures of $\bar{\gamma}[m]$ during six cycles of the mains signal. . . . .	24
Figure 2 – Estimates of $R^o[m]$ during six cycles of the mains signal. . . . .	24
Figure 3 – The flowchart of the TCRA technique. . . . .	25
Figure 4 – Algorithm for the implementation of the TCRA technique . . . . .	28
Figure 5 – An example for optimal data rate and for the TCRA technique. (a) Optimal data rate, (b) the relationship among microslots inside on cycle of the mains signal is exploited, (c) the relationship among cycles of the mains signal is exploited, and (d) the relationship considering microslots and cycles of the mains signal are exploited. . . . .	30
Figure 6 – Estimates of $C_{\Upsilon[m]}[\tau]$ for $\Upsilon[m] = \bar{\gamma}[m]$ during 16 cycles of the mains signal. . . . .	32
Figure 7 – Estimates of $C_{\Upsilon[m]}[\tau]$ for $\Upsilon[m] = R^o[m]$ during 16 cycles of the mains signal. . . . .	32
Figure 8 – (a) CCDF of $\eta[m_{c,S_i\{j\}}]$ for <b>case #1</b> , where different values of $\alpha_1$ are used and $N_c = 1$ ; (b) CCDF of $\eta[m_{c,S_i\{j\}}]$ for <b>case #2</b> , where different values of $N_c$ are used and $\alpha_1 = 1$ ; (c) CCDF of $\eta[m_{c,S_i\{j\}}]$ for <b>case #3</b> , where different values of $N_c$ are used and $\alpha_1 = 0.7$ . . . . .	34
Figure 9 – CCDF of the data rate loss ratio observed before and after the time interval $\Delta T$ , when $\Upsilon[m] = \bar{\gamma}[m]$ and $\Upsilon[m] = R^o[m]$ . . . . .	35
Figure 10 – Performance comparison among the TCRA technique ( <b>case #3</b> ), the non-adaptive bit loading technique (first technique) [22], and the bit loading technique implemented in the IEEE 1901 Standard when $N_c = 20$ . . . . .	35
Figure 11 – (a) The nSNR and the CFR magnitude associated with a measured in-home PLC channel. (b) The PSD of a measured additive noise in a in-home electric circuit. . . . .	41
Figure 12 – Two hypothetic examples: (a) the flat nSNR (b) the flat CFR. . . . .	42
Figure 13 – Difference between the nSNR coherence bandwidth and the coherence bandwidth ( $B_{c,\bar{\gamma}} - B_{c,H}$ ) observed in the measured of in-home PLC channels: (a) $\alpha = 0.9$ and (b) $\alpha = 0.5$ . . . . .	44
Figure 14 – The In-home PLC channel: The best modeling (by single-component and Gaussian mixture distributions) of the nSNR coherence bandwidth ( $\alpha = 0.9$ ) for (a) $W_{30}$ ; (b) $W_{50}$ ; and (c) $W_{100}$ . . . . .	47
Figure 15 – The outdoor PLC channel: The best modeling (by single-component distribution) of the nSNR coherence bandwidth ( $\alpha = 0.9$ ) for (a) $W_{30}$ ; (b) $W_{50}$ ; and (c) $W_{100}$ . . . . .	50

Figure 16 – The hybrid PLC-wireless channel (PLC-to-wireless direction): The best modeling (by single-component and Gaussian mixture distributions) of the nSNR coherence bandwidth ( $\alpha = 0.9$ ) for (a) $W_{30}$ ; (b) $W_{50}$ ; and (c) $W_{100}$ . . . . .	53
Figure 17 – The hybrid PLC-wireless channel (wireless-to-PLC direction): The best modeling (by single-component and Gaussian mixture distributions) of the nSNR coherence bandwidth ( $\alpha = 0.9$ ) for (a) $W_{30}$ ; (b) $W_{50}$ ; and (c) $W_{100}$ . . . . .	56
Figure 18 – The algorithm for choosing the $L_c$ value when the SCRA technique is adaptive. . . . .	63
Figure 19 – The algorithm for the implementation of the SCRA technique. . . . .	66
Figure 20 – The CCDFs of the peak SER ( $\chi$ ) and the average SER ( $\bar{\chi}$ ) for different ways of choosing $p_{i,k}$ with $L_c = 8$ and $W_{50}$ . . . . .	67
Figure 21 – The CCDF of data rate loss ratio ( $\eta$ ) for different ways of choosing $p_{i,k}$ with $L_c = 8$ and $W_{50}$ . . . . .	68
Figure 22 – The CCDFs of the data rate loss ratio ( $\eta$ ) when the $L_c$ value is constant. (a) $W_{30}$ , (b) $W_{50}$ , and (c) $W_{100}$ . . . . .	69
Figure 23 – The CCDFs of the data rate loss ratio ( $\eta$ ) when the $L_c$ value is adaptive. (a) $W_{30}$ , (b) $W_{50}$ , and (c) $W_{100}$ . . . . .	71
Figure 24 – The CCDFs of the data rate loss ratio ( $\eta$ ) when the $L_c$ value is constant and adaptive. (a) $W_{30}$ , (b) $W_{50}$ , and (c) $W_{100}$ . . . . .	72
Figure 25 – The CCDFs of the data rate loss ratio ( $\eta$ ) when the $L_c$ value is chosen based on the nSNR coherence bandwidth and the coherence bandwidth. (a) $W_{30}$ , (b) $W_{50}$ , and (c) $W_{100}$ . . . . .	73
Figure 26 – Examples of tile geometry at the time-frequency domain for (a) OFDM scheme and (b) hypothetical time-frequency representation when $2N = 16$ . . . . .	80
Figure 27 – Examples of tile geometries of the time-frequency domain for $M = 16$ and hermitian symmetric. (a) Octave geometry and (b) $\mathcal{B}$ geometry with $\mathcal{B} = 2$ . . . . .	83
Figure 28 – A block diagram to implement the transmitter of the OTFDM scheme in the baseband. . . . .	84
Figure 29 – Block diagram of two options to implement the receiver of the OTFDM scheme in the baseband. (a) with high computational complexity and (b) with low computational complexity. . . . .	85
Figure 30 – Comparison between the OFDM and OTFDM (using $\mathcal{B}$ geometry with $\mathcal{B} = 128$ ) schemes. (a) the CFR of the PLC channel (b) the SNR per tile and (c) the SER per tile of the OTFDM scheme. . . . .	88
Figure 31 – The SER performances of the OFDM and the OTFDM schemes impaired by the background noise modeled as AWGN. . . . .	91

Figure 32 – The SER performances of the OFDM and the OTFDM schemes impaired by the background noise modeled as AWGN and the NBI component.	91
Figure 33 – SER performance of the OFDM and OTFDM schemes impaired by the background noise and impulsive noise components.	92
Figure 34 – The CCDFs of the data rate loss ratio ( $\eta$ ) when the optimal resource allocation technique is applied to the OFDM scheme and to the OTFDM scheme considering several tile geometries.	93
Figure 35 – The CCDFs of the data rate loss ratio ( $\eta$ ) when the SCRA technique is applied to the OTFDM scheme with $\mathcal{B} = 8$ and several $L_c$ values.	94
Figure 36 – The CCDFs of the data rate loss ratio ( $\eta$ ) when the SCRA technique is applied using $L_c = 8$ to the OFDM scheme and to the OTFDM scheme with $\mathcal{B} = 8$ .	95
Figure 37 – $C'_{\Upsilon[m]}[\tau]$ for $\Upsilon[m] = \bar{\gamma}[m]$ during 4 cycles of the mains signal ( $M = 25$ ).	105
Figure 38 – $C'_{\Upsilon[m]}[\tau]$ for $\Upsilon[m] = R^o[m]$ during 4 cycles of the mains signal ( $M = 25$ ).	106

## LIST OF TABLES

Table 1 – Three different cases that exploit the relationships. . . . .	25
Table 2 – Complexity reduction ratio and data rate loss ratio achieved by the TCRA technique when $\Upsilon[m] = \bar{\gamma}[m]$ and $P_{\eta>0.05} = 1 - P(\eta[m_{c,S_{i\{j\}}}] \leq 0.05)$ . . . . .	33
Table 3 – The evaluation criteria for the fits for $B_{c,\bar{\gamma}}$ in $W_{30}$ , $W_{50}$ and $W_{100}$ for in-home PLC channels. . . . .	46
Table 4 – The evaluation criteria for the fits for $B_{c,\bar{\gamma}}$ in $W_{30}$ , $W_{50}$ and $W_{100}$ for outdoor PLC channels. . . . .	49
Table 5 – The evaluation criteria for the fits for $B_{c,\bar{\gamma}}$ in $W_{30}$ , $W_{50}$ and $W_{100}$ for hybrid PLC-wireless channels in the PLC-to-wireless direction. . . . .	52
Table 6 – The evaluation criteria for the fits for $B_{c,\bar{\gamma}}$ in $W_{30}$ , $W_{50}$ and $W_{100}$ for hybrid PLC-wireless channels in the wireless-to-PLC direction. . . . .	55
Table 7 – Some information about $B_{c,\bar{\gamma}}$ of in-home PLC channels, outdoor PLC channels and hybrid PLC-wireless channels (both directions) for $W_{30}$ , $W_{50}$ and $W_{100}$ . . . . .	57
Table 8 – An example of the trade off between data rate loss ratio and computational complexity reduction ratio in Fig. 22a for $W_{30}$ . . . . .	68
Table 9 – Comparison between the SCRA technique feeds by $B_{c,\bar{\gamma}}$ and $B_{c,H}$ for $W_{100}$ . . . . .	74
Table 10 – The parameter estimates of the Gaussian mixture distributions. . . . .	108
Table 11 – The parameter estimates of the single-component distributions. . . . .	109

## ACRONYMS

<b>AIC</b>	Akaike information criterion
<b>AWGN</b>	additive white Gaussian noise
<b>BER</b>	bit error ratio
<b>BIC</b>	Bayesian information criterion
<b>CCDF</b>	complementary cumulative distribution function
<b>CFR</b>	channel frequency response
<b>CIR</b>	channel impulse response
<b>CSI</b>	channel state information
<b>DFT</b>	discrete Fourier transform
<b>DMT</b>	discrete multitone modulation
<b>DOST</b>	discrete orthogonal Stockwell transform
<b>EDC</b>	efficient determination criterion
<b>FDE</b>	frequency-domain equalization
<b>FFT</b>	fast Fourier transform
<b>FPGA</b>	field programmable gate array
<b>HS-OFDM</b>	hermitian symmetric OFDM
<b>HS-OTFDM</b>	hermitian symmetric OTFDM
<b>IDFT</b>	inverse discrete Fourier transform
<b>LPTV</b>	linear periodically time-varying
<b>LTI</b>	linear and time invariant
<b>LTV</b>	linear and time-varying
<b>MMSE</b>	minimum mean square error
<b>NBI</b>	narrow-band interference
<b>nm-SNR</b>	normalized multichannel SNR
<b>nSNR</b>	normalized signal to noise ratio

**OFDM** orthogonal frequency division multiplexing

**OTFDM** orthogonal time-frequency division multiplexing

**PDF** probability density function

**PLC** power line communication

**PSD** power spectral density

**QAM** quadrature amplitude modulation

**SCRA** spectral compressive resource allocation

**SER** symbol error rate

**SNR** signal to noise ratio

**TCRA** temporal compressive resource allocation

**ZF** zero-forcing

## CONTENTS

<b>1</b>	<b>INTRODUCTION . . . . .</b>	<b>16</b>
1.1	OBJECTIVES . . . . .	19
1.2	THESIS OUTLINE . . . . .	19
<b>2</b>	<b>A TEMPORAL COMPRESSIVE RESOURCE ALLOCATION TECHNIQUE FOR COMPLEXITY REDUCTION IN PLC TRANSCEIVERS . . . . .</b>	<b>21</b>
2.1	PROBLEM FORMULATION . . . . .	22
2.2	THE TEMPORAL COMPRESSIVE RESOURCE ALLOCATION TE- CHNIQUE . . . . .	25
2.3	PERFORMANCE ANALYSES . . . . .	31
2.4	SUMMARY . . . . .	36
<b>3</b>	<b>A NEW PARAMETER TO BE CONSIDERED IN RESOURCE ALLOCATION FOR PLC SYSTEMS . . . . .</b>	<b>38</b>
3.1	THE $n$ SNR COHERENCE BANDWIDTH . . . . .	39
3.2	THE COHERENCE BANDWIDTH VERSUS THE $n$ SNR COHERENCE BANDWIDTH . . . . .	41
3.3	STATISTICAL ANALYSES AND MODELING . . . . .	43
3.3.1	In-home PLC channels . . . . .	45
3.3.2	Outdoor and low-voltage PLC channels . . . . .	48
3.3.3	Hybrid PLC-wireless channels . . . . .	48
3.3.4	The $n$ SNR coherence bandwidth for the three PLC channels . . . . .	54
3.4	SUMMARY . . . . .	54
<b>4</b>	<b>A SPECTRAL COMPRESSIVE RESOURCE ALLOCATION TECHNIQUE FOR PLC SYSTEMS . . . . .</b>	<b>58</b>
4.1	PROBLEM FORMULATION . . . . .	59
4.2	SPECTRAL COMPRESSIVE RESOURCE ALLOCATION TECHNI- QUE . . . . .	62
4.3	PERFORMANCE ANALYSES . . . . .	65
4.3.1	Analysis of criteria for representing a chunk . . . . .	65
4.3.2	Analysis due to the $L_c$ value . . . . .	67
4.3.3	Comparison between the $n$ SNR coherence bandwidth and the coherence bandwidth . . . . .	70
4.4	SUMMARY . . . . .	74

<b>5</b>	<b>AN ORTHOGONAL TIME-FREQUENCY DIVISION MULTIPLEXING SCHEME . . . . .</b>	<b>75</b>
5.1	PROBLEM FORMULATION . . . . .	76
5.2	THE OTFDM SCHEME BASED ON THE DOST . . . . .	80
5.2.1	The discrete orthogonal Stockwell transform . . . . .	81
5.2.2	The OTFDM scheme . . . . .	83
5.2.3	The SNR in the OTFDM scheme . . . . .	85
5.2.4	The resource allocation in the OTFDM scheme . . . . .	87
5.3	PERFORMANCE ANALYSES . . . . .	90
5.3.1	The transmitter without CSI . . . . .	90
5.3.2	The transmitter with CSI . . . . .	92
5.4	SUMMARY . . . . .	94
<b>6</b>	<b>CONCLUSIONS . . . . .</b>	<b>96</b>
6.1	FUTURE WORKS . . . . .	98
	<b>REFERENCES . . . . .</b>	<b>99</b>
	<b>Appendix A – A Proof of the Cyclostationarity of <math>\Upsilon[m]</math> . . . . .</b>	<b>105</b>
	<b>Appendix B – The Estimated Parameters . . . . .</b>	<b>107</b>
	<b>Appendix C – Publications . . . . .</b>	<b>110</b>

## 1 INTRODUCTION

Power line communication (PLC) systems have been recognized and established as an important and alternative data communication solution to fulfill, under some constraints, the needs and the requirements associated with smart grid [1, 2], access network [2, 3], internet of things [4, 5] and local area network [6, 7]. The rationale behind it is the fact that electric power systems is ubiquitous, PLC technology uses the power cables for data communication, and the PLC channel capacity surpasses 1 Gbps. However, the electric power grids were primarily built for energy delivery, and, nowadays, they are recognized as the most complex system developed so far by the human being and thereby their use for data communication purpose is a challenging issue. The challenge is due to the dynamic of loads connected to the electric power systems, the electromagnetic compatibility and interference regulations, the physical characteristic and construction (unshielded) of the power cables, and the impedance mismatch (among the power cables and/or among the power cables and loads).

It is well-known the existence of multipath fading effects in the PLC channel [8–11] and, as a consequence, its channel frequency response (CFR) is selective in the frequency domain [12–16]. Moreover, the signal attenuation in the power cables increases with the distance, from the transmitter to the receiver, and/or with the frequency increase [12, 17–19]. Also, the dynamic of loads connected to the electric power grid results in PLC channels behaving as linear periodically time-varying (LPTV) or as linear and time-varying (LTV) [15, 20–24], mainly because the time-varying impedance mismatch among loads and/or the electric power grids at the point of connection and the AC/DC converters. With regards to the additive noise in PLC channel, the literature shows that it can be modeled as a cyclo-stationary random process, which is synchronous with the mains cycle [23–27]. Also, it is composed of several components, such as colored background noise, impulsive noise (synchronous and asynchronous with the mains cycle), and narrow-band interference (NBI) [10, 11, 27–29].

Due to the aforementioned characteristics of electric power grids for data communication purpose, current PLC technologies widely adopt multicarrier data communication schemes based on orthogonal frequency division multiplexing (OFDM) [30–34]. The most used multicarrier scheme in a PLC system is the hermitian symmetric OFDM (HS-OFDM) scheme [27, 28, 31, 35–38], better known as discrete multitone modulation (DMT) scheme [35, 36], since the data communication is in the baseband. The main advantage of OFDM-based schemes for PLC technologies is the fact that the information is transmitted through distinct subchannels in a very efficient way. In an OFDM scheme, each subcarrier can individually make use of a digital modulation for data communication and all of them transmit information during the same interval. As the conditions vary among the subchannels, then resource allocation techniques must be applied in order to maximize the

data rate or minimize the margin [39]. To do so, the channel state information (CSI) must be available at the transmitter side, since these techniques use the normalized signal to noise ratio (nSNR), which can be interpreted as the signal to noise ratio observed in all subchannels when the transmitter allocates unitary transmission power in all of them for data communication [39].

Resource allocation for OFDM-based PLC systems, assuming that the PLC channel is linear and time invariant (LTI), has been investigated in the literature. For instance, authors of [35] proposed a least mean square channel estimator for offering variable data rate in the DMT scheme for broadband PLC system. The problem of subchannel and power allocation for indoor PLC networks with multiple links under power spectral density constraint was investigated in [40], while [41] discussed the fairness of resource allocation in PLC networks with multiple links. Moreover, [42] and [43] paid attention to the influence of the length of cyclic prefix for bit-loading and the performance analysis of different bit-loading techniques, respectively. Multiuser resource allocation was discussed in [44] and the resource allocation problem, in the presence of interferences, was presented in [45]. Also, [46] presented a low complexity non-iterative discrete bit-loading algorithm to maximize the data rate subject to a given bit error ratio (BER) and uniform power allocation, whereas [47] proposes a fast bit loading algorithm based on the fractional knapsack algorithm. On the other hand, [48] introduced a modified incremental bit allocation algorithm and compared its performance with incremental bit loading algorithm [49]. Furthermore, [50] proposes an efficient bit loading algorithm with peak BER constraint for PLC systems.

The need for adaptive resource allocation in scenarios in which PLC channels are LPTV was initially discussed in [23, 25, 26]. Recently, [22] and [21] have addressed optimal resource allocation techniques using the idea of microslots. The microslot is a small time slot in which the assumption about the PLC channel being time invariant applies. These techniques maximize the transmission data rate by non-uniformly distributing the total energy or total transmission power, which is available for a set of microslots within a cycle of the mains signal, among the microslots. However, due to the time-varying behavior of PLC channels and the large number of subchannels in practical PLC systems based on OFDM schemes, the optimal resource allocation may result in unfeasible solution because it can lead to very high computational complexity (intensive hardware utilization) and network bandwidth consumption for data exchanges in PLC network because it may not agree with hardware and bandwidth constraints imposed by the design of the PLC transceiver and the PLC network.

The high computational complexity associated with [22] and [21] is related to the fact that the optimal resource allocation technique must be performed many times by second, at least, with a rate of  $1/T_c$ , in which  $T_c$  is the coherence time of a PLC channel, in

seconds. For instance, the coherence time of in-home PLC channel is equal to  $T_c = 600 \mu\text{s}$  [51], then the optimal resource allocation technique must be evaluated 1666.67 times per second. Additionally, every time the resource allocation technique is applied, part of the network bandwidth available for data communication must be allocated to exchange information related to the resource allocation technique. Therefore, if large number of users and/or subchannels are considered, then the network bandwidth for exchanging such information in a PLC network may considerably reduce the throughput of the whole PLC network. That means, a search for resource allocation techniques with low computational complexity and minimum data rate loss in comparison to the optimal or previous resource allocation available in the literature is an important issue to be pursued. Note that only [46–48, 50] presented suggestions to reduce the computational complexity of the resource allocation techniques.

Assuming the LPTV behavior of the PLC channels and the cyclo-stationarity of the PLC additive noise, then periodic features of these channels and additive noise can be combined to show that the nSNR is periodic in the time domain. If the nSNR is periodic, then it can be exploited in order to group microslots (contiguous or not) sharing similar nSNR and, as a consequence, it is possible to decrease the number of times the resource allocation is executed per second. Therefore, the allocation result can be sub-optimal, but savings in terms of computational complexity may be very interesting.

Another situation is to assume that the frequency domain representation of the nSNR in PLC channels share similar information. Such similarity or relationship may be exploited to group adjacent subchannels in a so-called chunk, such that all subchannels in this chunk receive the same portion of the total transmission power and transmit the same number of bits. This approach can reduce the dimensionality of the nSNR vector that feeds the resource allocation technique and, as a consequence, it can potentially decrease the computational complexity of the resource allocation technique. This case yields computational complexity reduction in the frequency domain and, similar to the time domain, the results are sub-optimal. Overall, it is evident that the exploitation of both time and frequency domains together or independently for resource allocation is an important research problem for investigation.

Although the approach which groups adjacent subchannels in a chunk may yield computational complexity savings, it also can present a data rate loss in comparison to the optimal resource allocation technique when OFDM-based schemes apply. It occurs because adjacent subchannels with similarities still present different nSNR values in a PLC system based on OFDM scheme, since the nSNR is selective in the frequency domain due to the nature of CFR and the power spectral density (PSD) of the additive noise. To overcome such problem several strategies can be applied. Among existing strategies, the introduction of a new multicarrier scheme that groups adjacent subchannels in an efficient

way can yield the same computational complexity reduction and small data rate loss in comparison with the OFDM-based schemes.

## 1.1 OBJECTIVES

Based on the aforementioned problems and motivations for introducing low-cost resource allocation technique for reducing the computational complexity of PLC transceivers, the main objectives of this thesis are as follows:

- To introduce and analyze the so-called temporal compressive resource allocation (TCRA) technique, which groups microslots sharing similar information (nSNR) in order to reduce the computational complexity of resource allocation techniques applied to OFDM-based PLC systems in the time domain when PLC channels are LPTV. This technique exploits the existing relationship among microslots.
- To discuss a novel parameter, which informs the flatness of the nSNR, in the frequency domain, in order to demonstrate that it is the most appropriate for grouping a set of subcarriers sharing similar information (nSNR). The novel parameter is called nSNR coherence bandwidth.
- To introduce and to analyze the spectral compressive resource allocation (SCRA) technique, which makes use of chunk of subcarriers specified by the nSNR coherence bandwidth to reduce the computational complexity of resource allocation in OFDM-based PLC systems. This technique exploits the existing relationship among the subchannels.
- To present and analyze a novel multicarrier scheme, which is capable of exploiting time-frequency representation of transmitted symbols to reduce the computational complexity of resource allocation technique for PLC systems with minimal data rate loss. This novel multicarrier scheme is called orthogonal time-frequency division multiplexing (OTFDM). It is a kind of technique that can be used to jointly exploit the time-frequency relationship.

## 1.2 THESIS OUTLINE

This thesis is organized as follows:

- Chapter 2 describes the TCRA technique for LPTV PLC channels and compares it with other existing techniques in the literature.
- Chapter 3 presents the nSNR coherence bandwidth to inform the flatness of the nSNR for resource allocation purposes and compares it with the coherence bandwidth, which informs the flatness of the communication channel.

- Chapter 4 focuses on the SCRA technique and compares it with the optimal resource allocation technique discussed in [22].
- Chapter 5 describes a new multicarrier scheme named OTFDM and its variation for baseband data communication. Moreover, this chapter proposes the use of the SCRA technique together with the OTFDM scheme to reduce the computational complexity of resource allocation techniques and shows its improvement in comparison with the OFDM scheme.
- Chapter 6 addresses the main conclusions of this thesis.

## 2 A TEMPORAL COMPRESSIVE RESOURCE ALLOCATION TECHNIQUE FOR COMPLEXITY REDUCTION IN PLC TRANSCEIVERS

The need for adaptive resource allocation in scenarios in which PLC channels are LPTV was initially discussed in [23, 25, 26]. Recently, [21] and [22] addressed optimal resource allocation techniques using the idea of microslots, which defines a time slot in which the channel state information is time invariant. These techniques maximize the data rate by non-uniformly distributing the total energy, which is available for a set of microslots, within a cycle of the mains signal, among the microslots. Yet, computational complexity reasons prevent this resource allocation technique from being used in real time implementation of OFDM-based PLC systems, because it demands a huge computational complexity. Therefore, the introduction of practical low-cost bit loading technique capable of exploiting the LPTV characteristic of PLC channel is of paramount importance and a challenging issue to be addressed when the concept of microslots is taken into account.

Note that the fact that PLC channels are LPTV [51, 52] and the PLC additive noise may be modeled by a cyclostationary random process with period equal to the period of the mains signal [23, 25, 51, 52] implies that the signal to noise ratio (SNR) shows a periodic behavior. Based on that information and aiming to reduce the computational complexity of resource allocation technique, the IEEE 1901 standard [53] included the possibility of using the bit loading calculated in one microslot of one cycle of the mains signal, in the consecutive ones – limited to 8 microslots per cycle. Although it reduces the computational complexity, limited improvement is observed because the number of grouped microslots is at most 8.

In this context, this chapter introduces the temporal compressive resource allocation (TCRA) technique for exploiting the relationship among microslots and, as consequence, offering a resource allocation technique with low computational complexity for OFDM-based PLC systems when the PLC channel is LPTV. The main idea behind this technique is the exploitation of existing relationship among the normalized SNR, over microslots, in LPTV PLC channels, which allows a trade off between computational complexity reduction and data rate loss. The TCRA technique, following [53] and different from [21, 22], allocates the same amount of energy among the microslots, which overcome some difficulties hindering the use [21, 22] in a real-time OFDM-based PLC system, namely (i) the need for much more hardware resource utilization and energy for bit loading allocation (cost must be as low as possible); (ii) the potential violation of the electric field radiation limits imposed by regulatory authorities (there is a limit on the PSD for power allocation); (iii) the limitations imposed by the coherence time of PLC channels and network bandwidth for data control exchanges because the CSI must be exchanged among the users each microslots. The main contributions of this chapter are as follows:

- The introduction of a novel bit loading technique that addresses existing relationships within one cycle of mains signal, over consecutive cycles of the mains signal, and both of them altogether to trade computational complexity reduction with data rate loss.
- Performance analyses on measured data set and comparison with IEEE 1901 standard and the techniques proposed in [22]. Note that [22] is the main reference technique in the literature for comparison.

## 2.1 PROBLEM FORMULATION

Assume an LPTV PLC channel that during a time interval  $T_c$  called *coherence time*, is modeled as LTI. A microslot is defined as a time window spanning a time interval  $T_{\bar{\gamma}}$ , such that  $T_{\bar{\gamma}} \ll T_c$ . The noise is modeled, during each microslot interval, as an additive, stationary and zero mean random process. In each cycle of the mains signal there are  $M$  microslots and, for each microslot, the PLC channel is modeled as a frequency-selective LTI channel. The vectorial discrete-time representation of the channel impulsive response, during the  $m^{\text{th}}$  microslot, is  $\mathbf{h}[m] = [h_0[m], h_1[m], \dots, h_{L_h-1}[m]]^T$ , where  $L_h$  is the channel length and  $(\cdot)^T$  denotes the transpose operator. Now, if an OFDM scheme with  $N$  subcarriers is taken into account, then  $\mathbf{H}[m] = [H_0[m], H_1[m], \dots, H_{2N-1}[m]]^T$  is the discrete frequency vector representation of an LTI PLC channel in the  $m^{\text{th}}$  microslot. Also,  $\mathbf{V}[m] = [V_0[m], V_1[m], \dots, V_{2N-1}[m]]^T$ , in which  $\mathbb{E}\{V_k[m]V_j[m]\} = \mathbb{E}\{V_k[m]\}\mathbb{E}\{V_j[m]\}$  for  $k \neq j$ ,  $\mathbb{E}\{V_k[m]\} = 0$ , and  $\mathbb{E}\{\cdot\}$  denotes the expectation operator, is the vector corresponding to the discrete frequency representation of the additive noise in the  $m^{\text{th}}$  microslot. Now, assume that

$$\mathbf{\Lambda}_{|\mathbf{H}[m]|^2} \triangleq \mathbf{diag}\{|H_0[m]|^2, |H_1[m]|^2, \dots, |H_{2N-1}[m]|^2\} \quad (2.1)$$

and

$$\mathbf{\Lambda}_{\sigma_{\mathbf{V}[m]}^2} \triangleq \mathbf{diag}\{\sigma_{V_0[m]}^2, \sigma_{V_1[m]}^2, \dots, \sigma_{V_{2N-1}[m]}^2\}, \quad (2.2)$$

where  $\sigma_{V_k[m]}^2$  is the noise variance in the  $k^{\text{th}}$  subchannel for the  $m^{\text{th}}$  microslot. Thereby, the nSNR, which represents the SNR in all subchannels when the transmitter allocates unitary energy [39] in all subcarriers, can be defined by

$$\begin{aligned} \mathbf{\Lambda}_{\bar{\gamma}[m]} &\triangleq \mathbf{diag}\{\bar{\gamma}_0[m], \bar{\gamma}_1[m], \dots, \bar{\gamma}_{N-1}[m]\} \\ &= \mathbf{\Lambda}_{|\mathbf{H}[m]|^2} \mathbf{\Lambda}_{\sigma_{\mathbf{V}[m]}^2}^{-1}. \end{aligned} \quad (2.3)$$

Note that  $\mathbf{\Lambda}_{\bar{\gamma}[m]}$  is a function of the channel. Based on the literature, a parameter that represents the nSNR in all subchannels in the  $m^{\text{th}}$  microslot is the normalized multichannel SNR (nm-SNR), which is expressed by [39]

$$\bar{\gamma}[m] = \det\left(\mathbf{I}_{2N} + \mathbf{\Lambda}_{\bar{\gamma}[m]}\right)^{\frac{1}{2N}} - 1, \quad (2.4)$$

where  $\mathbf{I}_{2N} \in \mathbb{R}^{2N \times 2N}$  is an  $2N \times 2N$  identity matrix, and  $\det(\cdot)$  is the determinant operator.

To proceed, consider the vectors  $\mathbf{b}[m] = [b_0[m], b_1[m], \dots, b_{N-1}[m]]^T$  and  $\mathbf{E}[m] = [E_0[m], E_1[m], \dots, E_{N-1}[m]]^T$  in which  $b_k[m]$  and  $E_k[m]$  are the number of bits and the energy allocated to the  $k^{\text{th}}$  subcarrier at the  $m^{\text{th}}$  microslot. Also, assume that matrix representations of these vectors are given by  $\Lambda_{\mathbf{b}[m]} = \mathbf{diag}\{b_0[m], b_1[m], \dots, b_{N-1}[m]\}$ ;  $\Lambda_{\mathbf{E}[m]} = \mathbf{diag}\{E_0[m], E_1[m], \dots, E_{N-1}[m]\}$ . By applying a bit loading technique (e.g., water filling [39, 54], greedy [55], LPTV-aware [22]) in each microslot, the optimal resource allocation, in the sense of data rate maximization subject to a maximum total transmit energy  $E_t$ , applied to the  $m^{\text{th}}$  microslot results in  $\Lambda_{\mathbf{b}^o[m]}$  and  $\Lambda_{\mathbf{E}^o[m]}$  after solving a resource allocation problem. In the literature, there are two criteria to solve a resource allocation problem namely rate-adaptive and margin-adaptive [39]. This thesis considers the first one in order to maximize the transmission data rate. The optimal results can be expressed by

$$[\Lambda_{\mathbf{b}^o[m]}, \Lambda_{\mathbf{E}^o[m]}] = f(\Lambda_{\bar{\gamma}[m]}, E_t, \Gamma), \quad (2.5)$$

where  $E_t$  is the total energy to be shared among the subcarriers at the  $m^{\text{th}}$  microslot and  $\Gamma$  denotes a gap factor from the Shannon capacity curve that accounts for the deployment of practical modulation and coding schemes [39, 42, 44]. The optimal data rate obtained for the  $m^{\text{th}}$  microslot is given by

$$R^o[m] = \frac{1}{T_{\text{OFDM}}} \text{Tr}(\Lambda_{\mathbf{b}^o[m]}), \quad (2.6)$$

where  $\text{Tr}(\cdot)$  is the trace operator,  $T_{\text{OFDM}} = T_{\text{sym}} + T_{\text{cp}}$  is the OFDM symbol duration and  $T_{\text{sym}}$  and  $T_{\text{cp}}$  denote the time durations of the OFDM symbol and the cyclic prefix, respectively.

The proposal discussed in [22], although optimal, may be impractical due to three main reasons: (i) the need for introducing low-cost and energy savings telecommunication equipment, which require lowering the hardware cost of the transceiver for dealing with the constraints associated with emerging applications (smart grid, smart cities, etc); (ii) the need for maximizing the network resource utilization by lowering the use of network bandwidth for exchanging control information among the transceivers, which can considerably reduce the throughput since the chosen bit loading technique needs to be run every microslot, CSI must be exchanged every microslot, and the coherence time of PLC channels is usually around  $600 \mu\text{s}$  [51]; and (iii) the need to respect the electric field radiation limits regulated by national telecommunication regulatory agencies because the optimal resource allocation in each microslot may violated these limits.

To think of solutions for these problems, it would be useful to examine the curves plotted in Figs. 1 and 2. These plots portrays samples of, respectively,  $\bar{\gamma}[m]$  and  $R^o[m]$  – these were measured during six consecutive cycles of the mains signal in the electric circuit of a laboratory at Federal University of Juiz de Fora, Minas Gerais state, Brazil.

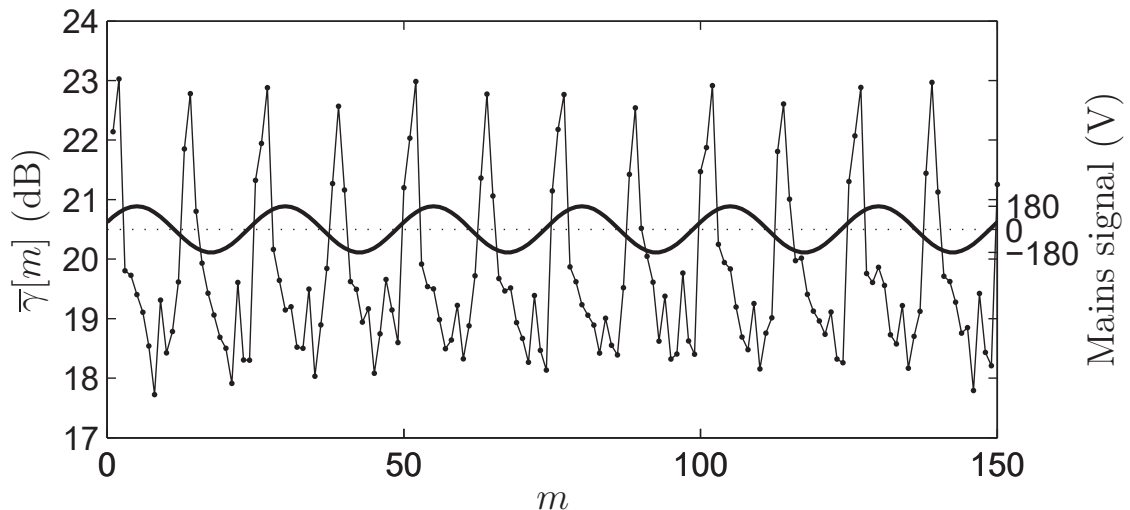


Figure 1: Measures of  $\bar{\gamma}[m]$  during six cycles of the mains signal.

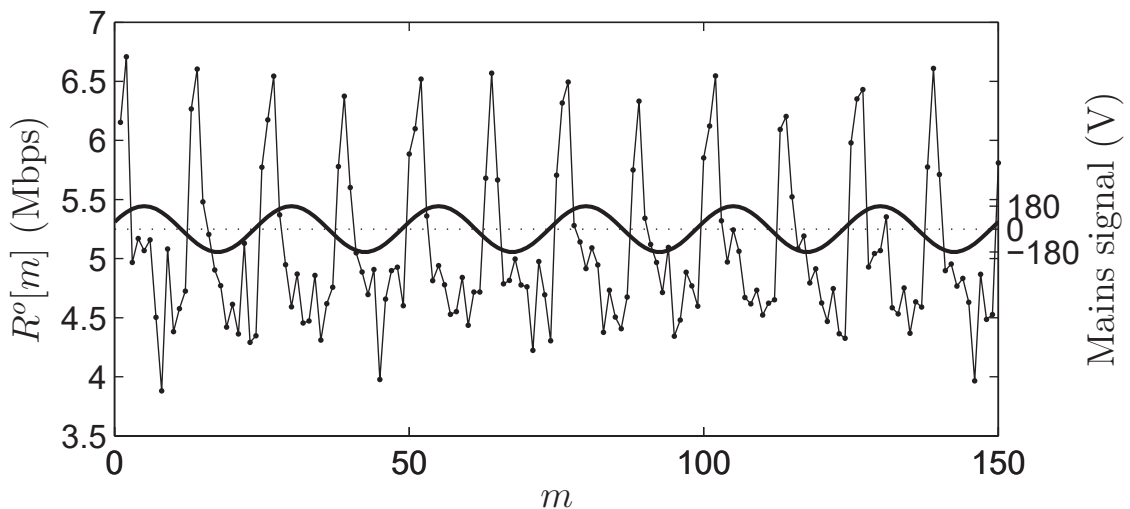


Figure 2: Estimates of  $R^o[m]$  during six cycles of the mains signal.

To obtain  $R^o[m]$ , the water filling based bit loading technique was applied. Fig. 1 and Fig. 2 illustrate that both  $\bar{\gamma}[m]$  and  $R^o[m]$  are approximately periodic in the time domain with period  $M$  (in these figures  $M = 25$ ), which corresponds to one cycle of the mains signal.

Now, assume that  $\bar{\gamma}[m]$  is a random variable and so the correlation coefficient of  $\bar{\gamma}[m]$  among microslots may be expressed by

$$C_{\bar{\gamma}[m]}[\tau] = \frac{\mathbb{E}\{(\bar{\gamma}[m] - \mu_{\bar{\gamma}})(\bar{\gamma}[m + \tau] - \mu_{\bar{\gamma}})\}}{\sigma_{\bar{\gamma}}^2}, \quad (2.7)$$

in which  $\tau \in \mathbb{Z}$ ,  $\mu_{\bar{\gamma}} = \mathbb{E}\{\bar{\gamma}[m]\}$ ,  $\sigma_{\bar{\gamma}}^2 = \mathbb{E}\{\bar{\gamma}[m]^2\} - \mu_{\bar{\gamma}}^2$ . As shown in Appendix A,  $\bar{\gamma}[m]$  can be modeled as a cyclostationary random process with period  $\tau = M$ . The correlation coefficient  $C_{R^o[m]}[\tau]$  of  $R^o[m]$  is similarly defined. By exploiting the fact that  $C_{\bar{\gamma}[m]}[\tau] \cong C_{\bar{\gamma}[m]}[\tau + M]$  and  $C_{R^o[m]}[\tau] \cong C_{R^o[m]}[\tau + M]$ , a bit loading technique with reduced computational complexity is devised in Section 2.2.

Table 1: Three different cases that exploit the relationships.

Exploited relationship	case #1	case #2	case #3
Among microslots inside one cycle	X		X
Among $N_c$ cycles		X	X

## 2.2 THE TEMPORAL COMPRESSIVE RESOURCE ALLOCATION TECHNIQUE

The TCRA technique exploits the relationship among microslots inside one cycle of mains signal, the relationship among  $N_c \in \mathbb{N}^*$  cycles of mains signal or both of them. Thereby, Table 1 addresses three different cases associated with the exploitation of these relationships.

The TCRA technique is divided into two parts. In the first part, the **Set Partitioning Procedure**, a partition of the set of microslots positions within a cycle of mains signal in subsets is done. The second part, the **Bit Loading Procedure**, as indicated in the flowchart of the TCRA technique shown in Fig. 3, is used to allocate bits to each member of the partition. In the flowchart of Fig. 3, the Greek letter  $\Upsilon$  is meant to be replaced by either  $\bar{\gamma}$  or  $R^o$  as the case may be. The two parts of the TCRA technique are described next.

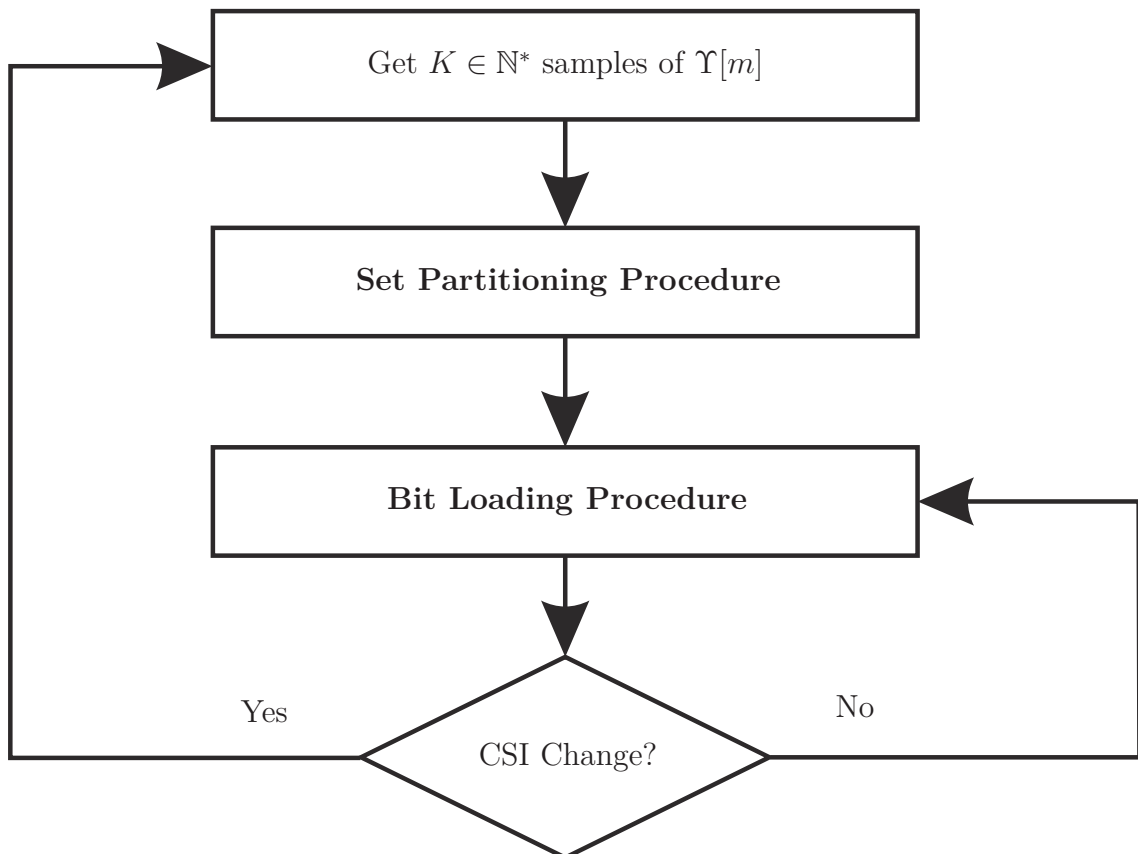


Figure 3: The flowchart of the TCRA technique.

**Microslot Set Partitioning Procedure:** in this part,  $\Upsilon[m] = R^o[m]$  or  $\Upsilon[m] = \bar{\tau}[m]$ . Thus, microslot positions, which indicates the position of a microslot within a cycle of the mains signal, are grouped into sets as follows:

**step #1** Evaluate (2.7) using  $K \in \mathbb{N}^* | K \gg M$  samples of  $\Upsilon[m]$ .

**step #2** Calculate the number of cycles of the mains signal that has high correlation using  $N_c = \max_{C_{\Upsilon[m]}[cM] \geq \alpha_2} \{c + 1\}$ , where  $c = 0, 1, 2, \dots$  is related to the  $c^{th}$  cycle of the mains signal and  $\alpha_2$  is the correlation threshold among  $N_c$  cycles of the mains signal.

**step #3** Define  $M$  sets (one set for each microslot position) composed of the microslot positions that have high correlation. Mathematically, define  $L_S^a = M$  sets, each one denoted by  $\mathcal{S}_l = \{l - 1 + \tau_1 + \tau_2 | C_{\Upsilon[m]}[\tau_1] \geq \alpha_1, 0 \leq \tau_1 \leq M - 1, \tau_2 = cM, \text{ and } 0 \leq c \leq N_c - 1\}$ , where  $l = 1, 2, \dots, L_S^a$  and  $\alpha_1$  is the correlation threshold inside one cycle of the mains signal. Note that one microslot can be in more than one set in this step.

**step #4** Eliminate the sets that have all elements belonging to other sets (e.g.,  $\mathcal{S}_l^b, L_S \leftarrow \min L_S^a$ , subject to  $\bigcup_{l=1}^{L_S} \mathcal{S}_l^b = \{0, 1, \dots, MN_c - 1\}$ ). Note that  $\mathcal{S}_l^b \cap \mathcal{S}_i^b \neq \{\emptyset\}$ , in which  $l \neq i, i \in \{1, 2, \dots, L_S\}$  can still occur.

**step #5** Define the data rate of a set as  $\varepsilon_{\mathcal{S}_l} = \min_j (\Upsilon[\mathcal{S}_l^b\{j\}])$ , where  $l = 1, 2, \dots, L_S$ ,  $j = 1, 2, \dots, L_{\mathcal{S}_l}$  and  $L_{\mathcal{S}_l} = \text{card}(\mathcal{S}_l)$ , in which  $\text{card}(\cdot)$  denotes the cardinality of a set.

**step #6** Identify those sets associated with the microslot position  $p$  within  $N_c$  cycles of the mains signal. Mathematically,  $l_p^* \triangleq \{l | \mathcal{S}_l^b \cap \{p\} \neq \{\emptyset\}\}$ , where  $0 \leq p \leq N_c M - 1$ .

**step #7** In order to eliminate the intersection, define  $L_S$  empty sets,  $\mathcal{S}_l = \{\emptyset\}$ ,  $1 \leq l \leq L_S$  and assume that the microslot position  $p$  is inserted only in the  $\mathcal{S}_{l_p^*}^b$  set, which has the maximum data rate,  $q = \arg \max_j (\varepsilon_{\mathcal{S}_{l_p^*}^b\{j\}})$ , where  $1 \leq j \leq \text{card}(l_p^*)$ . As a result,  $\mathcal{S}_l \cap \mathcal{S}_i = \{\emptyset\}$  and  $\text{card}(\bigcup_{l=1}^{L_S} \mathcal{S}_l) = MN_c$ .

It is important to note that if the thresholds  $\alpha_1 < 1$  and  $\alpha_2 = 1$ , then the proposed technique exploits the cyclostationarity of  $\Upsilon[m]$  only inside one cycle of the mains signal, i.e.  $0 \leq \tau \leq M - 1$  (case #1). On the other hand, by considering  $\alpha_1 = 1$  and  $\alpha_2 < 1$ , the cyclostationarity of  $\Upsilon[m]$  is exploited along  $N_c$  cycles of the mains signal (case #2) and if  $\alpha_1 < 1$  and  $\alpha_2 < 1$ , then cyclostationarity of  $\Upsilon[m]$  inside one cycle and among cycles of the mains signal are jointly exploited (case #3). Finally, if  $\alpha_1 = \alpha_2 = 1$ , then the proposed technique becomes the second technique described in [22], because it results in the optimal data rate in each microslot.

**Bit Loading Procedure:** After the Set Partitioning Procedure has yielded the partition members, the following steps must be performed:

**step #1** Evaluate (2.5) and (2.6) for the first microslot of each set (i.e.  $\mathcal{S}_l\{1\}$ ,  $l = 1, 2, \dots, L_S$ ).

**step #2** Use the resulting bit allocations in the other microslots by considering the sets provided by the Set Partitioning Procedure during  $N_c$  cycles of the mains signal.

Notice that the partition generated by the Set Partitioning Procedure, will remain unaltered during the operation of the transceiver unless the CSI changes. Therefore, the Set Partitioning Procedure is executed only at the beginning of the transceiver operation and whenever the CSI value changes. Fig. 4 shows the algorithm devised to implement the TCRA technique.

The differences emerging from the choice of  $\Upsilon[m]$  are summarized as follows:

- $\Upsilon[m] = R^o[m]$ : the data rate is *a priori* evaluated for all microslots by using the chosen bit loading technique that allocates bits in the subcarriers associated with microslots. Based on that bit loading information, the microslots partition is selected. It should be noted that the adoption of  $\Upsilon[m] = R^o[m]$ , raises considerably the computational complexity of the Set Partitioning Procedure since the bit loading technique is applied to all microslots, but the attained data rates are optimal for the chosen microslots partition.
- $\Upsilon[m] = \bar{\gamma}[m]$  implies that only nm-SNR estimates are considered for choosing the microslots partition in which the bit loading allocation will applied. As a result the computational complexity is considerably reduced since the bit loading technique is applied only to the chosen partition. This choice offers a suboptimal data rate because nm-SNR values do not correspond to the optimal data rate.

In order to evaluate the proposed technique, the data rate loss ratio per microslot and the computational complexity reduction ratio per cycle are computed. Let the microslots on the  $c^{th}$  cycle of the mains signal, which are associated with the  $j^{th}$  element of the  $l^{th}$  set, be defined as

$$m_{c,\mathcal{S}_l\{j\}} \triangleq \left\lfloor \frac{c}{N_c} \right\rfloor N_c M + \mathcal{S}_l\{j\}, \quad (2.8)$$

where  $c = 0, 1, 2, \dots, 0 \leq j \leq L_{\mathcal{S}_l}$ , and  $\lfloor a \rfloor = \max\{m \in \mathbb{Z} | m \leq a\}$ . Then, the minimum data rate of the  $l^{th}$  set on the  $c^{th}$  cycle of the mains signal is, based on (2.6), defined as

$$R_{c,\mathcal{S}_l}^{\min} \triangleq \min_{0 \leq j \leq L_{\mathcal{S}_l}} \left\{ R^o \left[ m_{c,\mathcal{S}_l\{j\}} \right] \right\}. \quad (2.9)$$

```

input :
   $K \in \mathbb{Z}$  is the number of samples to estimate  $\mu_Y$  and  $\sigma_Y^2$ ;
   $Y[m] \in \{\gamma[m] \text{ or } R^o[m]\}$ ;
   $\alpha_1 \in \mathbb{R}$  is a threshold;
   $\alpha_2 \in \mathbb{R}$  is a threshold;
   $M \in \mathbb{Z}$  is the number of microslots in a cycle of mains signal;
begin
  while PLC system is working do
    Set Partitioning Procedure
    • Step #1
     $\mu_Y = \frac{1}{K} \sum_{k=0}^{K-1} Y[k]$ ;
     $\sigma_Y^2 = \frac{1}{K} \sum_{k=0}^{K-1} (Y[k] - \mu_Y)^2$ ;
    for  $\tau = 0$  to  $K - 1$  do
      |  $C_{Y[m]}[\tau] = \frac{\mathbb{E}\{(Y[m] - \mu_Y)(Y[m+\tau] - \mu_Y)\}}{\sigma_Y^2}$ ;
    end
    • Step #2
     $N_c = 0$ ;
    for  $c = 0$  to  $K/M$  do
      | if  $C_{Y[m]}[cM] \geq \alpha_2$  then
      | |  $N_c = c + 1$ ;
      | end
    end
    • Step #3
     $L_S^a = M$ ;
    for  $l = 1$  to  $L_S^a$  do
      |  $S_l^a = \{l - 1 + \tau_1 + \tau_2 \mid C_{Y[m]}[\tau_1] \geq \alpha_1, 1 \leq l + \tau_1 \leq M, \tau_2 = cM, \text{ and } 0 \leq c \leq N_c - 1\}$ ;
    end
    • Step #4
     $S_l^b, L_S^b \leftarrow \min L_S^a$ , subject to
       $\bigcup_{l=1}^{L_S^b} S_l^b = \{0, 1, \dots, M - 1\}$ ;
    • Step #5
    for  $l = 1$  to  $L_S^b$  do
      |  $\varepsilon_{S_l} = \min_j (\Upsilon[S_l^b\{j\}])$ ;
      |  $S_l = \{\emptyset\}$ ;
    end
    • Steps #6 and #7
    for  $p = 0$  to  $N_c M - 1$  do
      |  $l_p^* = \{l \mid S_l^b \cap \{p\} \neq \{\emptyset\}\}$ ;
      |  $q = \arg \max_j (\varepsilon_{S_{l_p^*\{j\}}})$ ;
      |  $S_{l_p^*\{q\}} = S_{l_p^*\{q\}} + \{p\}$ ;
    end
    Bit Loading Procedure
    while CSI do not change do
      • Step #1
      for cycles of mains signal multiples of  $N_c$  do
        for the  $l^{\text{th}}$  set do
          |  $m_l = cM + S_l\{1\}$ ;
          | Evaluate (2.5) and (2.6) for microslot  $m_l$ ;
          |  $R_{S_l} = R^o[m_l]$ ;
        end
      end
      • Step #2
      Use  $R_{S_l}$  in the others elements of  $S_l$ ;
    end
  end

```

Figure 4: Algorithm for the implementation of the TCRA technique

The minimum data rate value represents the worst case scenario for the  $l^{th}$  set on the  $c^{th}$  cycle of the mains signal. Hence, the data rate loss ratio is defined as

$$\eta[m_{c,\mathcal{S}_l\{j\}}] \triangleq \frac{R^o[m_{c,\mathcal{S}_l\{j\}}] - R_{c,\mathcal{S}_l}^{\min}}{R^o[m_{c,\mathcal{S}_l\{j\}}]}, \quad (2.10)$$

where  $R^o[m_{c,\mathcal{S}_l\{j\}}]$  is the optimal data rate for the  $j^{th}$  element of the  $l^{th}$  set on the  $c^{th}$  cycle of the mains signal and, because of that it can be used to evaluate the data rate loss incurred by the proposed technique.

Now, let  $L_S$  be the number of times that a bit loading technique is applied during  $N_c$  cycles of the mains cycle in the Bit Loading Procedure. Then, the computational complexity reduction ratio per cycle is defined as

$$\rho \triangleq 1 - \frac{L_S}{MN_c}. \quad (2.11)$$

Fig. 5 illustrates the differences in terms of computational complexity reduction (number of times the bit loading technique has to be evaluated per cycle) among the optimal data rate (bit loading is performed each new microslot) and the cases addressed in Table 1 when  $M = 9$ . The black curve refers to the voltage waveform of the mains signal with frequency equal to 60 Hz. Microslots with the same color are given the same resource allocation and vertical lines indicate the instant that the nSNR is estimated and the resource allocation is performed. The microslots positions are sequentially labeled modulo 9 (with an integer number between 0 and 8).

Note that Fig. 5(a) shows the optimal data rate allocation, which is obtained when the bit loading technique is applied in each microslot ( $\alpha_1 = \alpha_2 = 1$ ). Also, the three cases addressed by the TCRA technique which are depicted in Fig. 5 (b)-(d), are summarized as follows:

- Fig. 5(b) applies for  $\alpha_1 < 1$  and  $\alpha_2 = 1$  (exploitation of relationship among microslots within one cycle of the mains signal - **case #1**). For this plot, the  $c^{th}$  cycle of the mains signal was divided in three sets ( $\mathcal{S}_1 = \{(c, 0), (c, 3), (c, 4), (c, 8)\}$ ,  $\mathcal{S}_2 = \{(c, 1), (c, 5)\}$ , and  $\mathcal{S}_3 = \{(c, 2), (c, 6), (c, 7)\}$ , where  $(c, p)$  denote the  $p^{th}$  microslot position on the  $c^{th}$  cycle of the mains signal). The nSNR is estimated and, in the sequel, the bit loading technique is applied in the microslot that corresponds to the first element of each set. In other words, in the microslot whose microslot positions are  $(c, 0)$ ,  $(c, 1)$ , and  $(c, 2)$ , respectively. The microslot positions represented by  $(c, 3)$ ,  $(c, 4)$ , and  $(c, 8)$  make use of the bit allocation provided by the bit loading technique applied in the  $(c, 0)$  microslot position. In the same way, the bit allocation performed for  $(c, 1)$  is reproduced in  $(c, 5)$ . Finally, in the  $(c, 6)$  and  $(c, 7)$  microslot positions are applied the bit allocation obtained for the  $(c, 2)$  microslot position. Note that the bit loading technique is executed three times per cycle of the mains signal.

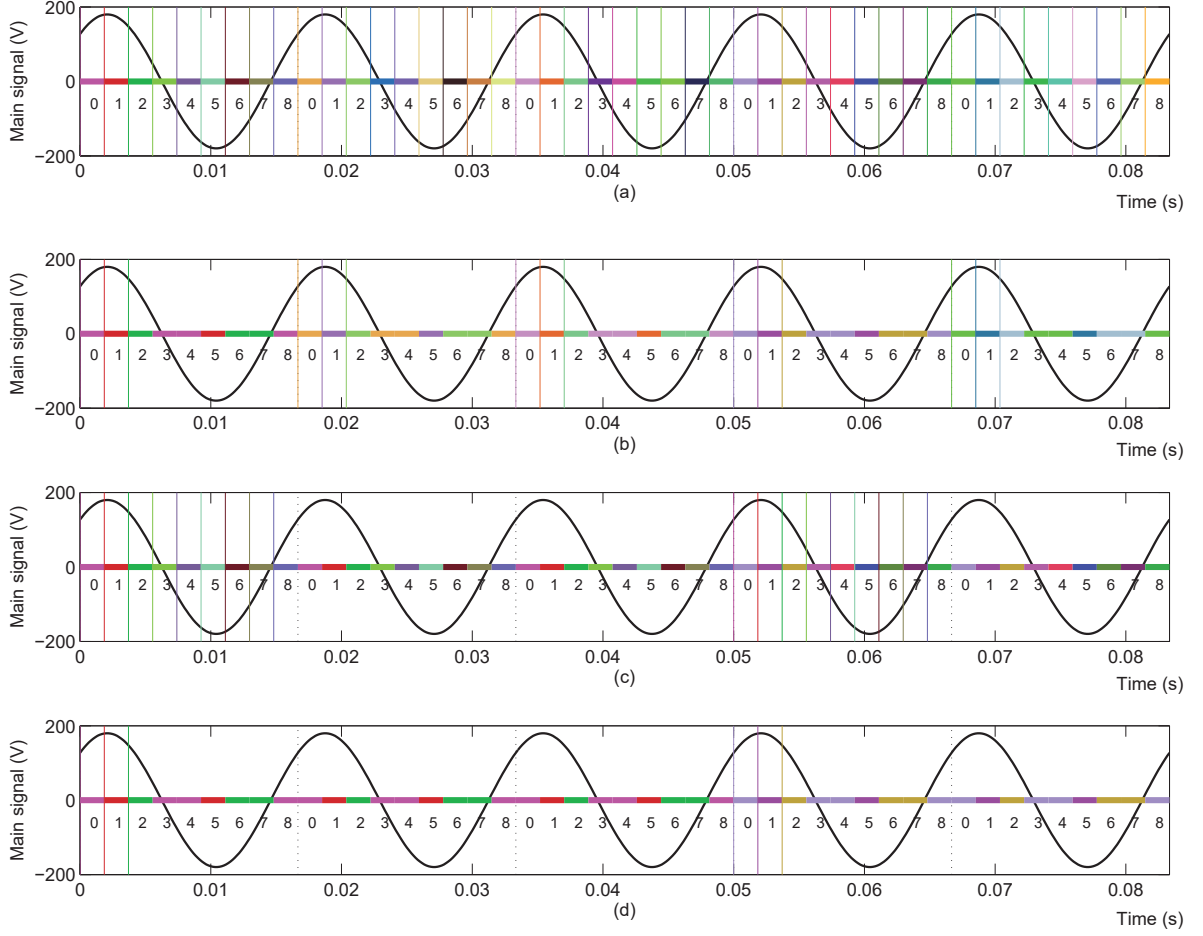


Figure 5: An example for optimal data rate and for the TCRA technique. (a) Optimal data rate, (b) the relationship among microslots inside on cycle of the mains signal is exploited, (c) the relationship among cycles of the mains signal is exploited, and (d) the relationship considering microslots and cycles of the mains signal are exploited.

- Fig. 5(c) exemplifies  $\alpha_1 = 1$  and  $\alpha_2 < 1$  (exploitation of relationship among cycles of the mains signal - **case #2**). For this example, nine sets are defined and it is assumed that  $\alpha_1 = 1$  and  $N_c = 3$ . In other words,  $\mathcal{S}_l = \{(c, p), (c + 1, p), (c + 2, p)\}$ , where  $1 \leq l \leq 9$  and  $p = l - 1$ . It means that the nSNR is estimated and the bit loading technique is applied only in the microslot position associated with the first element of each set (i.e., the microslot position  $(c, p)$ ). The microslot positions  $(c + 1, p)$  and  $(c + 2, p)$  make use of the same bit allocation obtained with microslot position  $(c, p)$ . The bit loading technique is executed nine times every three cycles of the mains signal.
- Finally, Fig. 5(d) illustrates  $\alpha_1 < 1$  and  $\alpha_2 < 1$  (exploitation of relationship considering both microslots within one cycle and  $N_c$  cycles of the mains signal - **case #3**) when  $N_c = 3$ . In addition, a cycle of the mains signal is divided into three sets

( $\mathcal{S}_1 = \{(c, 0), (c, 3), (c, 4), (c, 8), (c + 1, 0), (c + 1, 3), (c + 1, 4), (c + 1, 8), (c + 2, 0), (c + 2, 3), (c + 2, 4), (c + 2, 8)\}$ ,  $\mathcal{S}_2 = \{(c, 1), (c, 5), (c + 1, 1), (c + 1, 5), (c + 2, 1), (c + 2, 5)\}$ , and  $\mathcal{S}_3 = \{(c, 2), (c, 6), (c, 7), (c + 1, 2), (c + 1, 6), (c + 1, 7), (c + 2, 2), (c + 2, 6), (c + 2, 7)\}$ ). The nSNR is estimated and the bit loading technique is applied in the microslot position related to the first element in each set, which are  $(c, 0)$ ,  $(c, 1)$  e  $(c, 2)$ . For the microslot positions belonging to set  $\mathcal{S}_1$ , the used bit allocation is that one obtained for the  $(c, 0)$  microslot position. Similarly, for the microslot positions in the  $\mathcal{S}_2$  and  $\mathcal{S}_3$ , the bit loading allocations are those ones obtained in the  $(c, 1)$  and  $(c, 2)$  microslot positions, respectively. Note that the bit loading technique is executed three times every three cycles of the mains signal. Overall, note that  $\alpha_1 < 1$  and  $\alpha_2 < 1$  offer the minimum computational complexity because the bit allocation is performed, in average, one time per cycle of the mains signal.

### 2.3 PERFORMANCE ANALYSES

This section presents comprehensive performance analyses of the proposed technique in terms of data rate loss ratio and computational complexity reduction ratio. Also, a performance comparison with bit loading techniques described in [22] and the one devised for IEEE 1901 standard [53] are shown.

The performance analyses are based on a data set obtained in a measurement campaign carried out in low-voltage and indoor electric power grids in a laboratory at Federal University of Juiz de Fora, Minas Gerais state, Brazil. For the measurement campaign, a field programmable gate array (FPGA)-based prototype of a PLC transceiver that makes use of an HS-OFDM scheme [28] and operates in the frequency band delimited by 10 MHz and 20 MHz, was used. For the OFDM symbol, the number of subcarriers is  $N = 512$ ; the length of cyclic prefix is  $L_{cp} = 128$ ; the time period of an OFDM symbol is  $T_{OFDM} = (2N + L_{cp})/2B \cong 57.6\mu\text{s}$ ; 460 subcarriers are used for measuring the PLC channel frequency response because a guard frequency in both sides prevents out of band interferences. The minimum time interval for estimating the channel frequency responses and/or measuring the additive noise with the FPGA-based transceiver prototype is  $T_{\bar{\gamma}} = (1/f_0)/M = 666.66 \mu\text{s}$  because the main frequency is  $f_0 = 60 \text{ Hz}$  and, as a consequence,  $M = 25$ . Samples of estimates of  $\bar{\gamma}[m]$  and  $R^o[m]$ , which were obtained in the measurement campaign are shown in Figs. 1 and 2, respectively. Note that  $\bar{\gamma}[m]$  is according to (2.4) and  $R^o[m]$  is the optimal data rate yielded by the water filling-based bit loading technique.

Fig. 6 shows estimates of  $C_{\bar{\gamma}[m]}[\tau]$ ,  $0 \leq \tau < 400$  (sixteen cycles of the mains signal) which were obtained with the measured data shown in Fig. 1. On the other hand, Fig. 7 plots  $C_{R^o[m]}[\tau]$  for the same range of  $\tau$ . These graphs show that there is a strong relationship among microslots within one cycle of the mains signal (i.e.,  $0 \leq \tau \leq M - 1$ ),

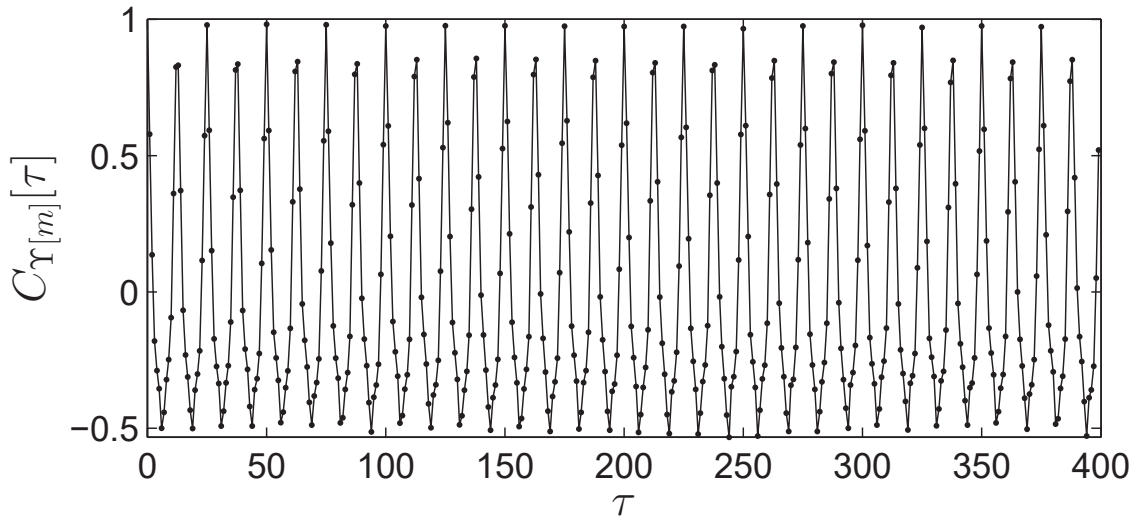


Figure 6: Estimates of  $C_{\Upsilon[m]}[\tau]$  for  $\Upsilon[m] = \bar{\gamma}[m]$  during 16 cycles of the mains signal.

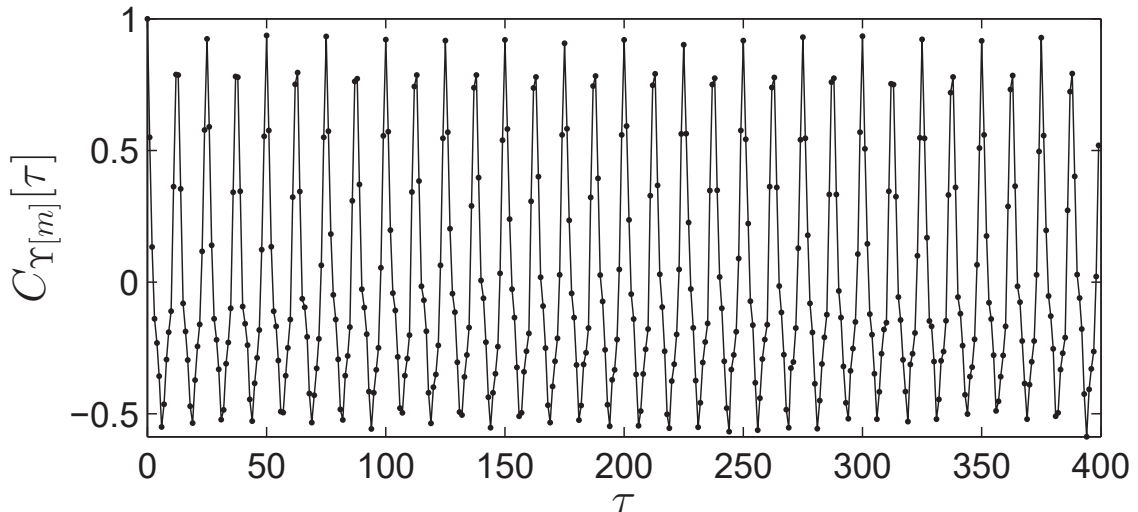


Figure 7: Estimates of  $C_{\Upsilon[m]}[\tau]$  for  $\Upsilon[m] = R^o[m]$  during 16 cycles of the mains signal.

for both parameters. Also, note that  $C_{\bar{\gamma}[m]}[\tau]_{\tau=375} = 0.97$  and  $C_{R^o[m]}[\tau]_{\tau=375} = 0.93$ . This means that after 15 cycles of the mains signal, the correlation coefficient is still high for the same microslot position within the cycle of the mains signal.

Fig. 8a, 8b, and 8c show the complementary cumulative distribution function (CCDF) of data rate loss ratio when  $\Upsilon[m] = \bar{\gamma}[m]$  and illustrate the differences among the outputs associated with **case #1**, **case #2**, and **case #3**, respectively. Also, Fig. 8a shows that the proposed technique is very sensitive to changes of  $\alpha_1$ . As  $\alpha_1$  increases, the probability that  $\eta[m_{c,S_i\{j\}}]$  is higher than a pre-specified value is reduced; however,  $\rho$  decreases because  $L_S$  increases. Note that when  $\alpha_1 = 1.0$ , no computational complexity savings is obtained because  $P(\eta[m_{c,S_i\{j\}}] > 0.1) = 0.0$  and, as a consequence,  $\rho = 0$ . On the other hand, if, for instance,  $\alpha_1 = 0.1$ , then  $P(\eta[m_{c,S_i\{j\}}] > 0.1) = 0.41$  and  $\rho = 0.84$ . It means that on average only 16% of the microslots in a cycle of the mains signal need

Table 2: Complexity reduction ratio and data rate loss ratio achieved by the TCRA technique when  $\Upsilon[m] = \bar{\gamma}[m]$  and  $P_{\eta>0.05} = 1 - P(\eta[m_{c,S_i\{j\}}] \leq 0.05)$ .

Case #1	$\alpha_1 = 1.0$	$\alpha_1 = 0.7$	$\alpha_1 = 0.3$	$\alpha_1 = 0.1$	$\alpha_1 = -0.7$
$P_{\eta>0.05}$	0	0.318	0.548	0.606	0.876
$\rho$	0	0.52	0.76	0.84	0.96
Case #2	$N_c = 1.0$	$N_c = 2$	$N_c = 4$	$N_c = 8$	$N_c = 16$
$P_{\eta>0.05}$	0	0.162	0.314	0.434	0.524
$\rho$	0	0.5	0.75	0.875	0.9375
Case #3	$N_c = 1.0$	$N_c = 2$	$N_c = 4$	$N_c = 8$	$N_c = 16$
$P_{\eta>0.05}$	0.318	0.454	0.582	0.682	0.756
$\rho$	0.52	0.76	0.88	0.94	0.97

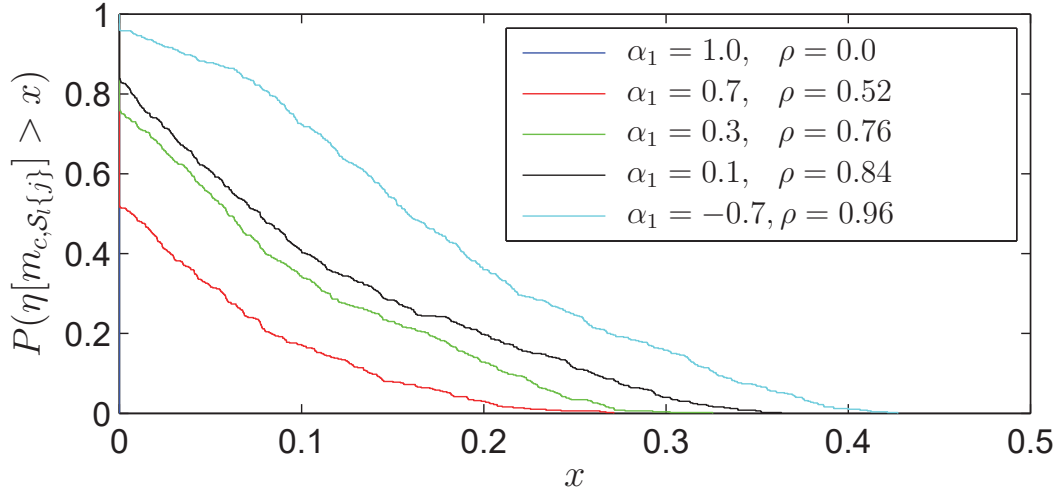
to be submitted to the chosen bit loading technique.

Fig. 8b shows that for the **case #2**, the probability  $P(\eta[m_{c,S_i\{j\}}] > x)$  vary significantly in comparison with the probabilities presented in Fig. 8a if, for instance,  $N_c \in \{1, 2, 4, 8, 16\}$ . The rationale behind this is the fact that the evaluated correlation considering  $N_c \leq 16$  is high (see Fig. 7). On the other hand, the higher  $N_c$  is, the higher  $\eta[m_{c,S_i\{j\}}]$  becomes and, as a consequence,  $\rho$  increases. Note that  $\rho = 0$  and  $\rho = 0.94$  for  $N_c = 1$  and  $N_c = 16$ , respectively. It means that on average only 6% of microslots within one cycle of the mains signal are submitted a chosen bit loading technique when  $N_c = 16$ .

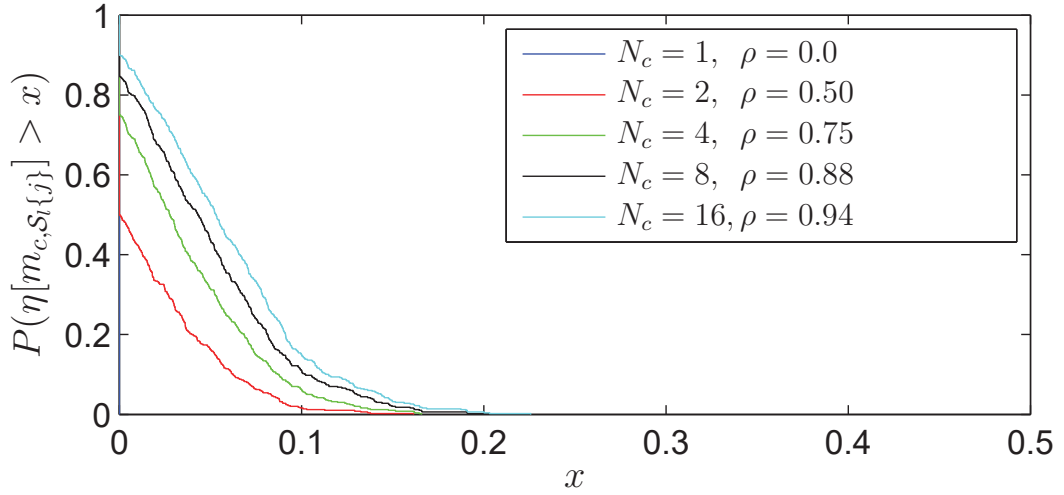
Finally, Fig. 8c highlights improvements offered by **case #3** (this case refers to the combination between **case #1** and **case #2**). For this plot,  $\alpha_1 = 0.7$  and  $N_c \in \{1, 2, 4, 8, 16\}$ . Note that computational complexity savings is achieved, since  $\rho = 0.52$  and  $\rho = 0.97$  for  $N_c = 1$  and  $N_c = 16$ , respectively. In other words, if  $N_c = 1$  and  $N_c = 16$ , then the bit loading technique have to be evaluated, on average, in 48% and 3% of microslots, respectively.

Table 2 lists the computational complexity reduction ratio when the probability of losing more than 5% of data rate for each case is considered ( $P_{\eta>0.05} = P(\eta[m_{c,S_i\{j\}}] > 0.05)$ ). Note that  $P_{\eta>0.05} = 0.548$  and  $\rho = 0.76$  for **case #1**,  $P_{\eta>0.05} = 0.314$  and  $\rho = 0.75$  for **case #2**, and  $P_{\eta>0.05} = 0.454$  and  $\rho = 0.76$  for **case #3**, if  $\alpha_1 = 0.3$ ,  $N_c = 4$  and  $N_c = 2$ , respectively. These results confirm that the proposed technique can effectively trade computational complexity reduction with data rate loss. Also, depending on the acceptable data rate loss ratio, the best performance results can be attained by considering **case #2** or **case #3**. Overall, **case #1** offers the lowest performance results in terms of computational complexity reduction ratio.

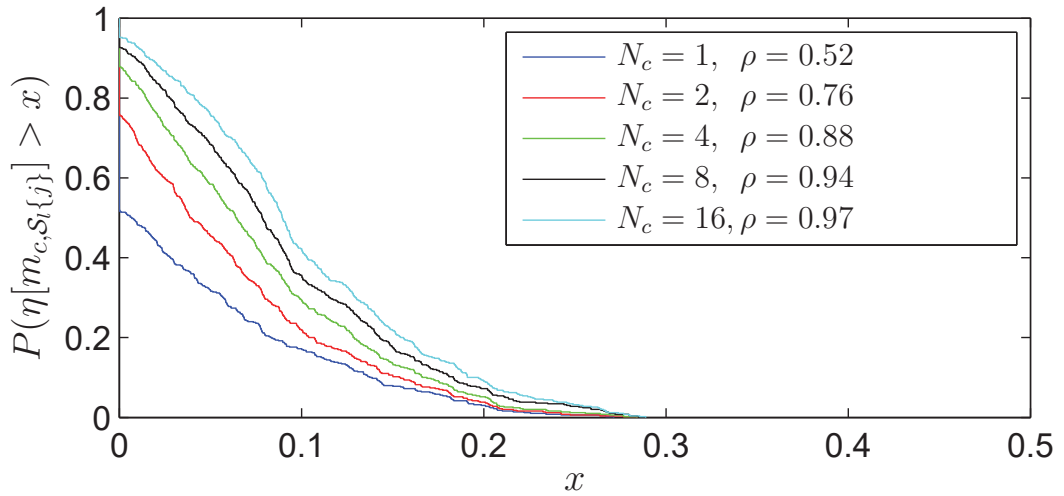
The plots in Fig. 9 show the results obtained when the Set Partitioning Procedure is executed on measured data set, which was collected in a given interval (DB#1) and in an interval separated by 60 seconds from the first one (DB#2) in the laboratory at UFJF. For both measured data set, the TCRA technique was applied using  $\alpha_1 = 0.7$  and



(a)



(b)



(c)

Figure 8: (a) CCDF of  $\eta[m_c, S_i\{j\}]$  for **case #1**, where different values of  $\alpha_1$  are used and  $N_c = 1$ ; (b) CCDF of  $\eta[m_c, S_i\{j\}]$  for **case #2**, where different values of  $N_c$  are used and  $\alpha_1 = 1$ ; (c) CCDF of  $\eta[m_c, S_i\{j\}]$  for **case #3**, where different values of  $N_c$  are used and  $\alpha_1 = 0.7$ .

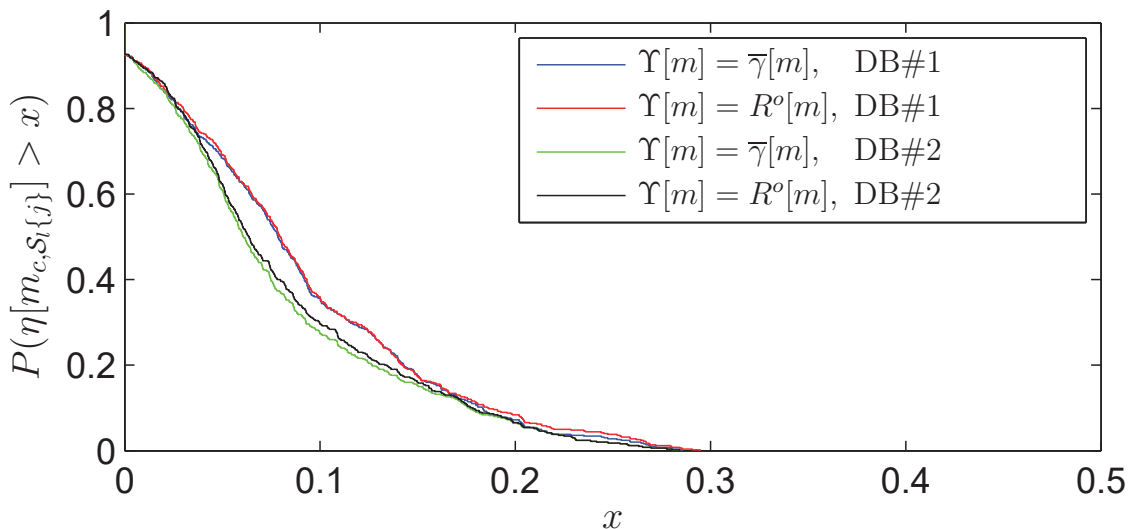


Figure 9: CCDF of the data rate loss ratio observed before and after the time interval  $\Delta T$ , when  $\Upsilon[m] = \bar{\gamma}[m]$  and  $\Upsilon[m] = R^o[m]$ .

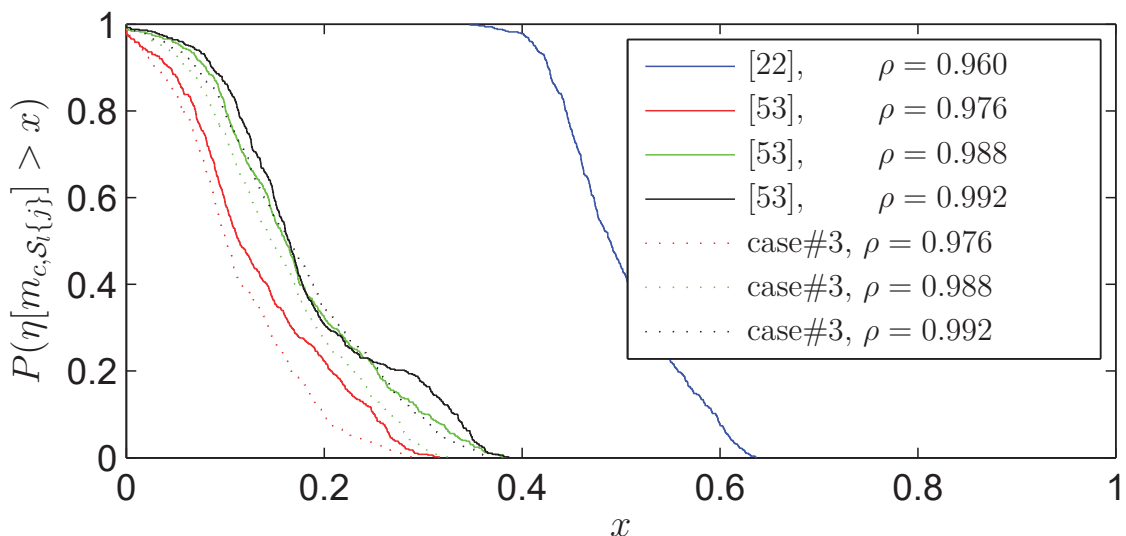


Figure 10: Performance comparison among the TCRA technique (**case #3**), the non-adaptive bit loading technique (first technique) [22], and the bit loading technique implemented in the IEEE 1901 Standard when  $N_c = 20$ .

$N_c = 8$ . Note that  $P(\eta[m_c, S_{l\{j\}}] > x)$  slightly differs when DB#1 and DB#2 feed the Bit Loading Procedure. It indicates that the periodic behavior of low-voltage and indoor PLC channels can still be observed after a long time period. Also, this plot highlights the fact that a small change in data rate loss ratio is observed when  $\Upsilon[m] = \bar{\gamma}[m]$  in comparison with  $\Upsilon[m] = R^o[m]$ . Therefore, the adoption of  $\Upsilon[m] = \bar{\gamma}[m]$  is strongly recommended for minimizing computational complexity.

Fig. 10 shows the performance comparison among the TCRA technique (**case #3** – the best option for the TCRA), the non-adaptation bit loading technique for LPTV channels (first technique discussed in [22]), and the bit loading technique implemented in

the IEEE 1901 standard [53]. Note that the improvements (in terms of data-rate loss ratio) offered by the TCRA technique can be significant in comparison with the non-adaptive bit loading technique. Important to highlight that the proposed technique with  $\alpha_1 = \alpha_2 = 1$  achieves data rates that are equal to those obtained with the simplistic adaptation technique, which is described in [22]; however, this kind of performance demands huge computational complexity because the bit loading technique is applied in each microslot. Regarding, the third and the fourth techniques described in [22], they offer optimal data rate because energy is non-uniformly allocated among the microslots. However, both techniques are not taken into account in our performance comparison because they can potentially violate the electric field radiation limits, demand amplifiers with a wide linear excursion, and require significant network bandwidth for data control exchange.

Further analysis on Fig. 10 shows that the improvements (in terms of data-rate loss ratio) offered by the TCRA technique can be as high as 15% for a pre-specified value of rate-loss ratio if the comparison is with the IEEE 1901 standard. According to the IEEE 1901 standard, each cycle of the mains signal can be divided in up to eight sets of microslots. In this context, a comparison between the TCRA (**case #3**) technique (dashed lines) and the one presented in IEEE 1901 standard (solid lines) — see Fig. 10, considers the usage of three sets of microslots. These sets are constituted by 4, 8, and 12 microslots, corresponding to  $\rho = 0.976$ ,  $\rho = 0.988$  and  $\rho = 0.992$ , respectively. It is important to note that the computational complexity reduction ratio  $\rho = 0.992$  extrapolates the limits of the IEEE 1901 standard because the cycle of the mains signal is divided into twelve sets of microslots while the IEEE 1901 standard limits the number of sets of microslots in 8. Note that, for  $\rho = 0.988$ , at 10% of the measured data the data rate loss ratio is higher than 0.26, if the proposed technique is applied. On the other hand, if IEEE 1901 standard technique is used, for 10% of the measured data the data rate loss ratio is higher than 0.30. This result illustrates that the improvement in comparison with the IEEE 1901 standard, is, in this case, around 15%.

## 2.4 SUMMARY

The main conclusions of this chapter are summarized as follows:

- The proposed technique facilitates the trade off computational complexity reduction for data rate loss and the use of it with the nm-SNR parameter as input is strongly recommended due to its low computational complexity and low performance degradation.
- The exploitation of the nm-SNR relationship within the main cycle and over the cycles of the mains signal individually or together results in the best trade off between computational complexity reduction and data rate loss.

- The proposed technique yields improvements in comparison with the bit loading technique recommended by the IEEE 1901 standard. Also, it achieves, under some constraints, the same results as the simplistic adaptation technique, which is discussed in [22]. Furthermore, it outperforms the non-adaptive technique described in [22]. Due to its flexibility to trade bit-rate with computational complexity, the proposed technique is more appropriate for hardware implementation.

### 3 A NEW PARAMETER TO BE CONSIDERED IN RESOURCE ALLOCATION FOR PLC SYSTEMS

The optimal resource allocation for each microslot as discussed in [22] may be impracticable because it demands a very high computational complexity and signaling overhead (network bandwidth). Moreover, the majority of practical resource allocation techniques for OFDM-based PLC systems [35, 39–41, 44, 47] makes use of the nSNR. Numerical analyses of adjacent subchannels indicate that their nSNR present relevant relationship and, as a consequence, can be used to propose a sub-optimal resource allocation technique with an important advantage: low computational complexity. However, a problem to exploit such relationship is the fact that a parameter that correctly informs the flatness of the nSNR, as the coherence bandwidth does for the CFR, does not exist in the literature. To extend the usefulness of the coherence bandwidth for computational complexity reduction of resource allocation techniques, [56] and [57] introduced the use of it to determine the size of group of adjacent subchannels sharing almost the same nSNR in wireless communication systems based on OFDM scheme. Despite the interesting results, the straightforward application of this idea to the PLC channel may not be appropriate because PLC channels present increasing attenuation profile when the frequency increases and the additive noise is a colored random process. The combination of the PLC channel and noise results in an nSNR that is totally different from the CFR. Therefore, it is of utmost importance to come up with a parameter that effectively characterizes the flatness of the nSNR.

In this context, this chapter aims to introduce a new parameter that informs the flatness of the nSNR for resource allocation in OFDM-based PLC systems. This parameter is named nSNR coherence bandwidth. Due to its characteristic, this parameter is capable of capturing the flatness of the nSNR. Moreover, considering a data set constituted by measures of PLC channels and additive noises of in-home, outdoor and low voltage, and hybrid PLC-wireless [58, 59] environments, this chapter discusses comprehensive statistical analyses of the nSNR coherence bandwidth for three different frequency bands: 1.7-30 MHz, 1.7-50 MHz and 1.7-100 MHz. The first and the second frequency bands comply with European and Brazilian regulations for PLC system operation [60, 61], respectively, while the latter is being investigated for improving PLC system performance [13]. The main contributions of this chapter are summarized as follows:

- The proposal of the nSNR coherence bandwidth, which can be used to come up with low computational complexity and sub-optimal resource allocation technique for OFDM-based PLC systems.
- The comparison between the nSNR coherence bandwidth and the coherence bandwidth to show, under which circumstances, the former parameter is more relevant

than the latter for OFDM-based PLC systems.

- The statistical analyses of the nSNR coherence bandwidth for in-home PLC channels, low voltage and outdoor PLC channels and hybrid PLC-wireless channels measured in Brazil in the three aforementioned frequency bands.

### 3.1 THE nSNR COHERENCE BANDWIDTH

Assume that the PLC channel is LTI within an OFDM symbol interval, since the coherence time of PLC channels is much longer than the OFDM symbol interval. Moreover, let  $h(t)$  and  $H(f)$  be the channel impulse response (CIR) and the CFR of an LTI PLC channel. According to the literature, the coherence bandwidth is expressed by [13, 16]

$$B_{c,H} = \max_{|R_H(\Delta f)| \geq \alpha} \{\Delta f\}, \quad (3.1)$$

where  $0 \leq \alpha \leq 1$  is a threshold and  $R_H(\Delta f)$  is the frequency correlation function, which can be expressed by

$$R_H(\Delta f) = \int_{-\infty}^{\infty} H(f)H^*(f + \Delta f)df, \quad (3.2)$$

where  $(\cdot)^*$  represents the complex conjugate operator. According to [13, 16], the coherence bandwidth informs the flatness of the CFR. This is a very important information for situations in which the CFR drives the performance, such as frequency domain equalization. To apply this information for resource allocation purposes, [56, 57] proposed the adoption of the coherence bandwidth for grouping adjacent subcarriers in order to reduce the number of subchannels information to feed the resource allocation technique in wireless communication systems. Although the attained results are interesting for reducing the computational complexity, a detailed look at the resource allocation technique shows that, different from the frequency domain equalization, the nSNR is the information that drives the performance of resource allocation.

In this context, let the transmission signal and the PLC additive noise be stationary random processes, then the SNR in the frequency domain can be expressed by

$$\gamma(f) = \frac{S_x(f) |H(f)|^2}{S_v(f)}, \quad (3.3)$$

where  $S_x(f)$  is the PSD of the transmission signal and  $S_v(f)$  is the PSD of the additive noise. Therefore, the nSNR can be expressed by

$$\bar{\gamma}(f) = \frac{|H(f)|^2}{S_v(f)}. \quad (3.4)$$

Note that the nSNR varies with the square magnitude of the CFR, thus a small variation of magnitude in the CFR may result in a large variation of the nSNR, which is not captured

by the coherence bandwidth. Moreover, the nSNR depends on the additive noise PSD that is not flat in electric power grids.

The coherence bandwidth can offer good results for reducing the computational complexity of resource allocation techniques, as observed in wireless communication systems [56, 57], benefited by the fact that the additive noise in wireless channels is white random process. On the other hand, the adoption of the coherence bandwidth for resource allocation in PLC system demands more attention because it does not inform the flatness of the nSNR. Thus, a new parameter capable to informing the flatness of the nSNR and its statistical analysis for PLC systems can assist the introduction of a new sub-optimal resource allocation technique with low computational complexity.

In this regard, this chapter advocates that the so-called nSNR coherence bandwidth is the most appropriate parameter to be used for exploiting the existent relationship among adjacent subchannels to come up with low cost resource allocation techniques for PLC systems, since it precisely reflects the flatness of the nSNR. Grounded on the definition of the coherence bandwidth [13, 16], the nSNR coherence bandwidth is defined as follows:

*Definition 1 (The nSNR Coherence Bandwidth):* Let  $\bar{\gamma}(f) \in \mathbb{R}$  be the nSNR as a function of  $f \in \mathbb{R}$ ,  $-\infty \leq f \leq \infty$ , then the nSNR self-correlation function is given by

$$R_{\bar{\gamma}}(\Delta f) = \int_{-\infty}^{\infty} \bar{\gamma}(f)\bar{\gamma}(f + \Delta f)df. \quad (3.5)$$

Therefore, the nSNR coherence bandwidth is defined by

$$B_{c,\bar{\gamma}} \triangleq \max_{|R_{\bar{\gamma}}(\Delta f)| \geq \alpha} \{\Delta f\}, \quad (3.6)$$

where  $\alpha \in \mathbb{R} | 0 \leq \alpha \leq 1$  is a threshold.

The usefulness of  $B_{c,\bar{\gamma}}$  is illustrated in Fig. 11. Fig. 11a shows the nSNR and the magnitude of a CFR associated with a measured in-home electric power grid, while Fig. 11b illustrates the PSD of the measured noise in the same circuit. The evaluation of the self-correlation of the CFR and of the nSNR shows that both of them are different. For instance, they yield, for a correlation level of 0.9, frequency shift of 5.1 MHz and 2 MHz, respectively. In this specific situation, the use of  $B_{c,H} = 5.1$  MHz in resource allocation technique may introduce remarkable data rate loss, because subcarriers with very distinct nSNR are grouped in a same set. As the nSNR is the main information to feed a resource allocation technique, then the use of the technique suggested in [56, 57] can introduce remarkable data rate loss. For instance, if the bandwidth of a subchannel in a PLC channel is  $\Delta B = 50$  kHz, then  $B_{c,\bar{\gamma}}$  will group 40 subsequent subcarriers, while  $B_{c,H}$  will group 102 subsequent subcarriers. Note that the problem with  $B_{c,H}$  is that it does not properly take into account the influence of the additive noise, which is normally not white, and the squared magnitude of the CFR.

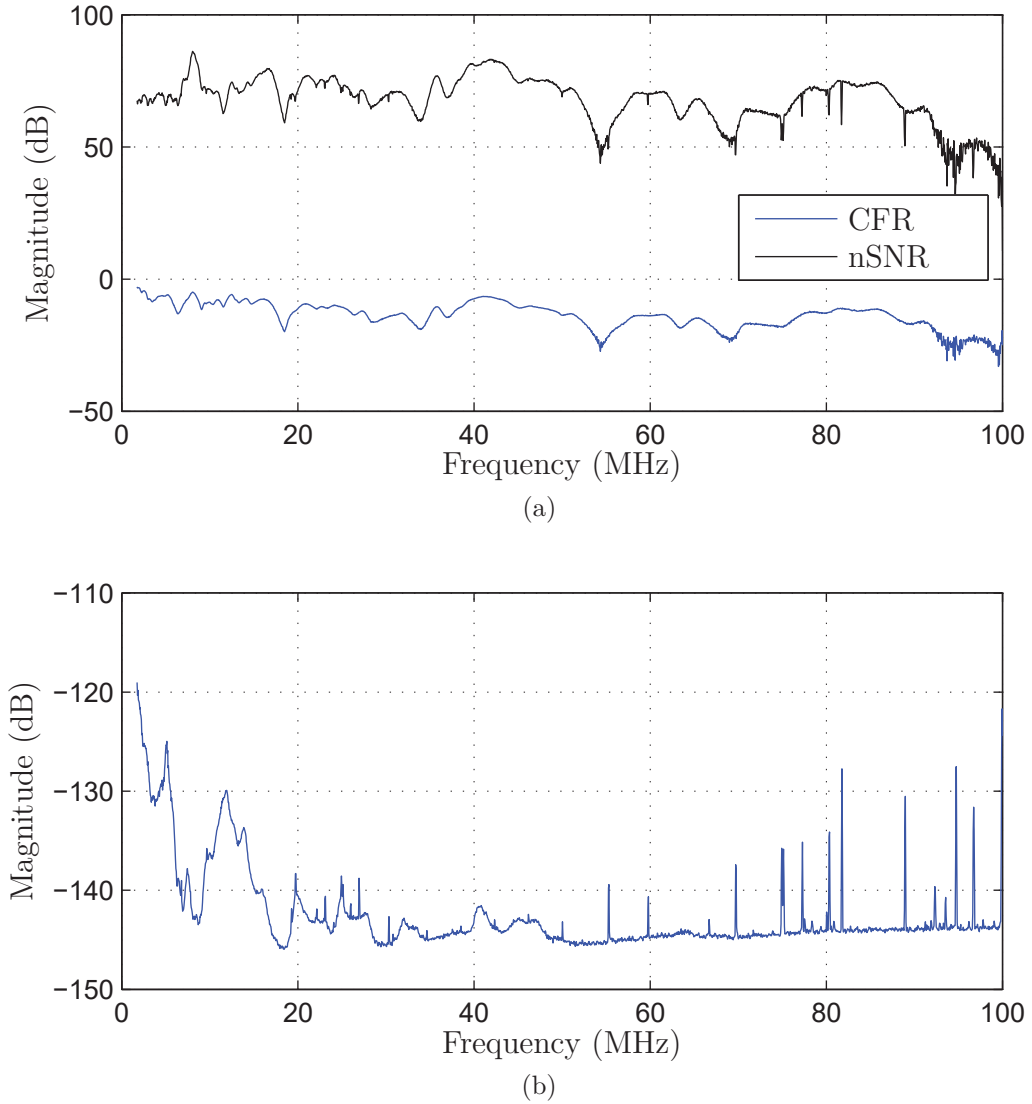


Figure 11: (a) The nSNR and the CFR magnitude associated with a measured in-home PLC channel. (b) The PSD of a measured additive noise in a in-home electric circuit.

### 3.2 THE COHERENCE BANDWIDTH VERSUS THE nSNR COHERENCE BANDWIDTH

In order to clarify the differences between the nSNR coherence bandwidth and the coherence bandwidth, assume that the CFR and the PSD of the additive noise of a hypothetic channel are given, respectively, by

$$H(f) = 0.5|f|^{-0.45}e^{2\pi fj}, \quad (3.7)$$

and

$$S_v(f) = 0.00025|f|^{-0.9}. \quad (3.8)$$

The plots in Fig. 12a show the magnitude curves of the CFR, the additive noise PSD and the nSNR associated with this hypothetic channel for  $B = 50$  MHz, for the same value of  $\alpha$ . For this channel, the coherence bandwidth  $B_{c,H}$  is equal to 195 kHz when the correlation

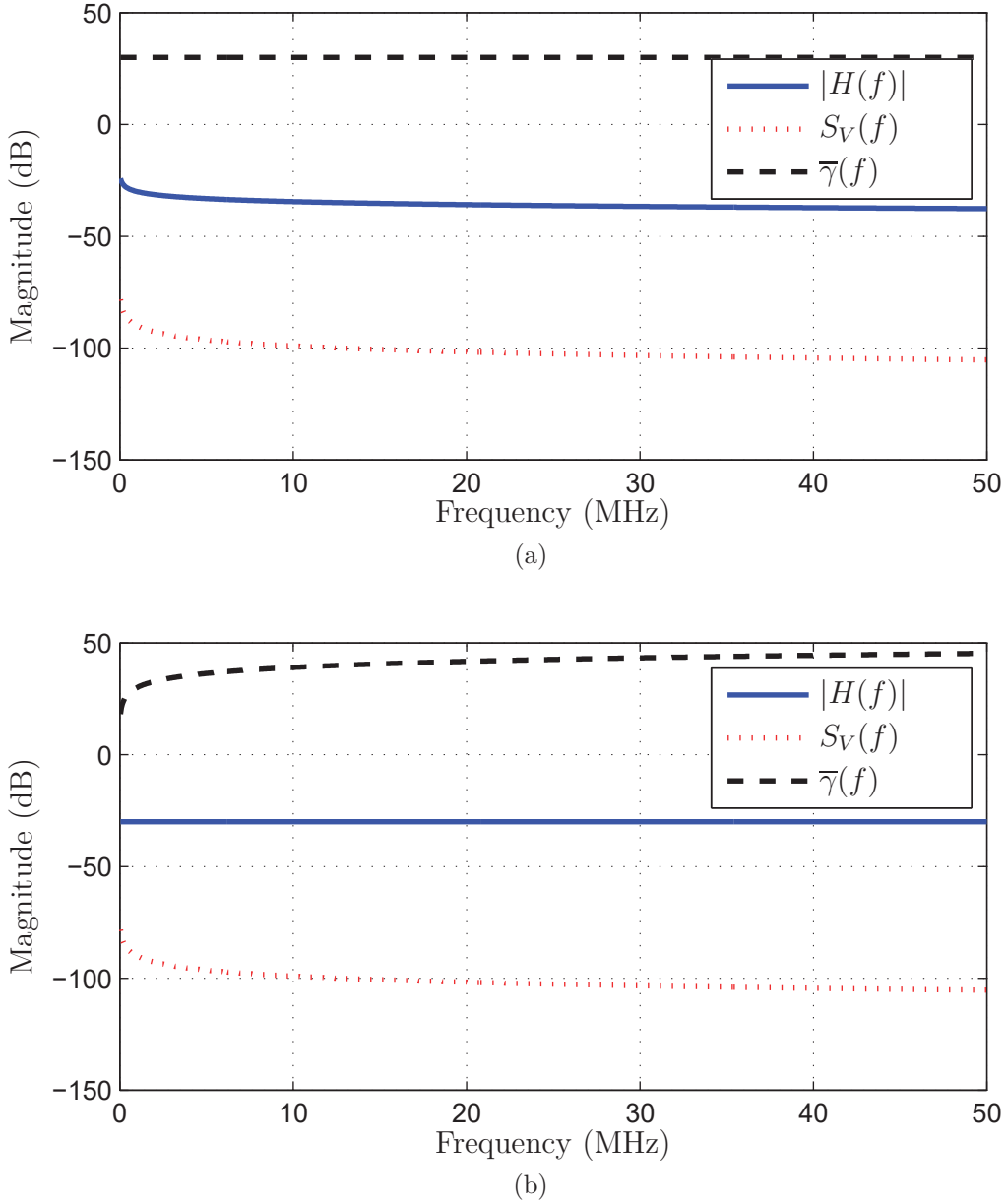


Figure 12: Two hypothetical examples: (a) the flat nSNR (b) the flat CFR.

coefficient  $\alpha$  is chosen to be 0.9, while the nSNR coherence bandwidth is  $B_{c,\bar{\gamma}} = 50$  MHz. For instance, if an OFDM scheme applies, then the coherence bandwidth will inform that at least  $\lceil B/B_{c,H} \rceil = 257$  (where  $\lceil a \rceil = \min\{n \in \mathbb{Z} | n \geq a\}$ ) information of subchannels must feed the bit loading technique, while the nSNR coherence bandwidth informs that only one subchannel information is enough to perform the bit loading technique. In other words, the nSNR coherence bandwidth can result in considerable savings in terms of computational complexity of resource allocation techniques because it precisely captures the flatness of the nSNR.

Now, assume that the CFR of a hypothetical channel is expressed by

$$H(f) = 0.001e^{2\pi f j}, \quad (3.9)$$

and the noise PSD be expressed by (3.8). Fig. 12b shows the magnitude of the CFR, the PSD of the additive noise and the nSNR curve for  $B = 50$  MHz. For a correlation level of  $\alpha = 0.9$ , the values of the coherence bandwidth and the nSNR coherence bandwidth are 50 MHz and 4 MHz, respectively. In other words, the use of coherence bandwidth for reducing the computational complexity of resource allocation technique indicates that the information of only one subchannel must feed the bit loading technique, while the nSNR coherence bandwidth correctly suggests at least  $\lceil B/B_{c,\bar{\gamma}} \rceil = 13$  information of subchannels must be feed the bit loading technique. One can note that, the coherence bandwidth mistakenly shows that all subbands can transmit the same number of bits, which does not make sense because the nSNR is not flat at all.

Finally, consider estimates of CFR of PLC channel and PSD of the additive noise obtained during a measurement campaign carried out in seven residences, covering houses and apartments in the city of Juiz de Fora, Minas Gerais state, Brazil, by using the measurement setup and the methodology discussed in [62] and [63], respectively. The total number of measured CFRs and noise PSDs is 7,117. These estimates were obtained by following [63]: sampling frequency equal to 200 MHz; frequency band from 1.7 MHz up to 100 MHz; an HS-OFDM scheme [28] with lengths of OFDM symbol and cyclic prefix equal to  $2N = 4096$  and  $L_{CP} = 512$ , respectively; and frequency resolution of each subchannel equal to 48.8 kHz. Fig. 13 shows the difference between the nSNR coherence bandwidth and the coherence bandwidth for each measured channel. Note that the nSNR coherence bandwidth is different from the coherence bandwidth, as it was emphasized through the two previous hypothetical examples. For  $\alpha = 0.9$  ( $\alpha \rightarrow 1$ ), there is a slight difference between the two coherence bandwidths, whereas for  $\alpha = 0.5$  ( $\alpha \rightarrow 0$ ) this difference significantly increases. Furthermore, the nSNR coherence bandwidth is smaller than the coherence bandwidth ( $B_{c,\bar{\gamma}} < B_{c,H}$ ) in 60.3% of the cases for  $\alpha = 0.9$  and 60.7% for  $\alpha = 0.5$ . This shows that the nSNR coherence bandwidth is in general more conservative than the coherence bandwidth, which means that a smaller number of adjacent subchannels share similar information and will be grouped to feed the bit loading technique if the nSNR coherence bandwidth applies.

### 3.3 STATISTICAL ANALYSES AND MODELING

The objective of this section is to perform statistical analyses of the nSNR coherence bandwidth in order to model its probability density function (PDF), by addressing different frequency bands and types of channels. These analyses aims to obtain the best model for the histogram of the nSNR coherence bandwidth for in-home, outdoor and low-voltage and hybrid PLC-wireless channels by analyzing single-component and Gaussian mixture distributions. This is an important analysis because it can assist the design of novel resource allocation techniques with reduced computational complexity. The chosen

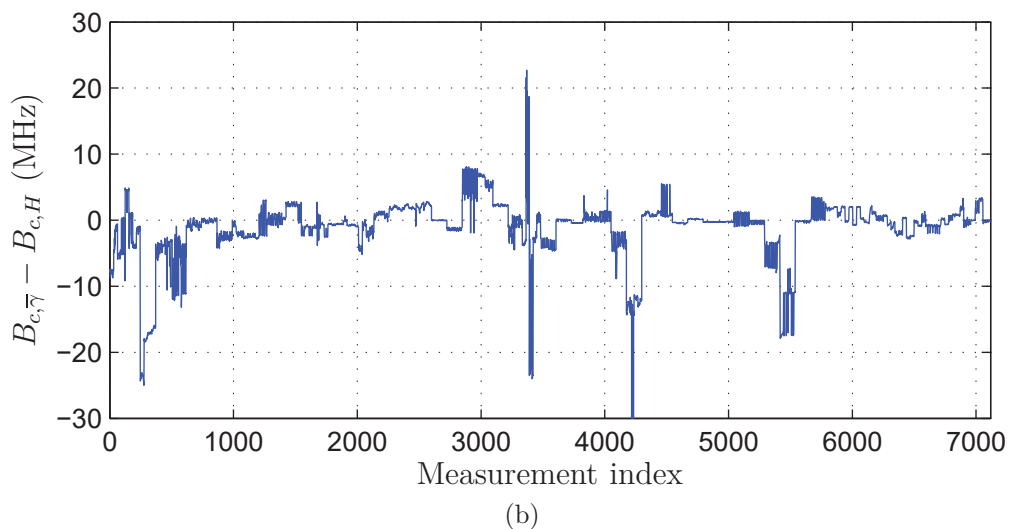
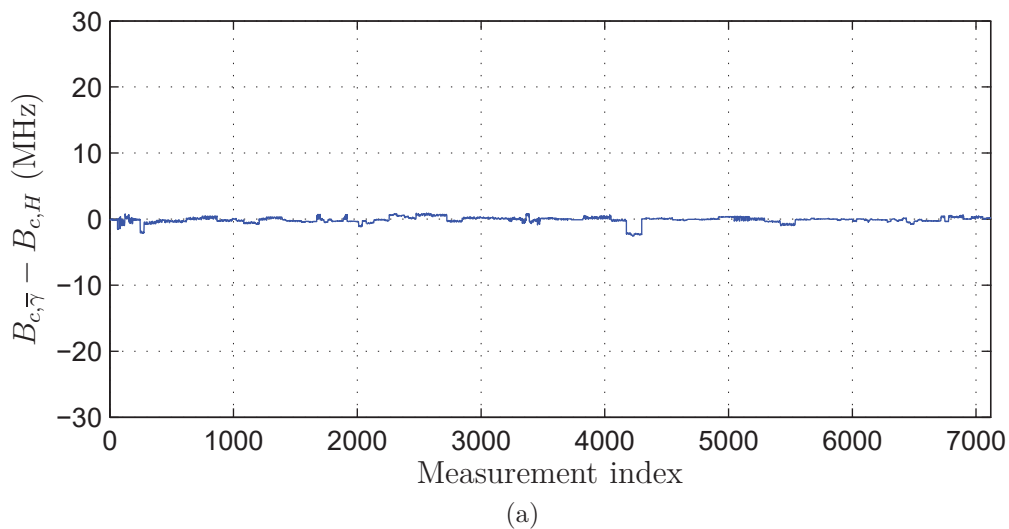


Figure 13: Difference between the nSNR coherence bandwidth and the coherence bandwidth ( $B_{c,\bar{\gamma}} - B_{c,H}$ ) observed in the measured of in-home PLC channels: (a)  $\alpha = 0.9$  and (b)  $\alpha = 0.5$ .

frequency bands are 1.7-30 MHz, 1.7-50 MHz, and 1.7-100 MHz, which are named  $W_{30}$ ,  $W_{50}$  and  $W_{100}$ , respectively. Moreover, this chapter adopts  $\alpha = 0.9$ , since it is the highest  $\alpha$  value among those generally accepted in the literature for determining the coherence bandwidth, which are 0.5, 0.7, and 0.9.

Note that the nSNR coherence bandwidth presents discrete values because the channel estimation procedure works in the discrete-time domain; however, due to the nature of the nSNR coherence bandwidth, it is a continuous random variable. Because of that, the statistical analysis of  $B_{c,\bar{\gamma}}$  takes into account several symmetric and asymmetric continuous distributions. The investigated single-component distributions are Log-Normal, Exponential, Gamma, Inverse Gaussian, Logistic, Log-Logistic, Nakagami, Normal and Weibull, and the Gaussian mixture distributions are with two to four components.

These choices refer to the fact that these distributions are widely used in the literature.

Based on [64], Akaike information criterion (AIC), Bayesian information criterion (BIC), efficient determination criterion (EDC), and Log-Likelihood function are used as evaluation criteria to choose the best model for the histogram. For the Log-Likelihood function, the distribution that offers the best modeling is the one with the maximum Log-Likelihood value. Meanwhile, for the AIC, BIC and EDC criteria, the best modeling is offered by the distribution showing the minimum AIC, BIC and EDC value, respectively. For the latter three, there is a compensation for handling the number of parameters of distribution, in order to provide a fair evaluation. This chapter assumes that a modeling is the best one if it obtains the best value for the majority of evaluation criteria. Moreover, the estimated parameters of the distributions that provide the best modeling of the nSNR coherence bandwidth for all aforementioned frequency bands are listed in the Appendix B.

### 3.3.1 In-home PLC channels

This analysis is based on measured in-home PLC channels and additive noise gathered from seven residences, covering houses and apartments [58]. The data set used is the same one briefly described in Section 3.2. The total number of measured in-home PLC channels and PLC additive noise is 7,117, thereby there are 7,117 nSNRs.

Table 3 lists the evaluation criteria results for both single-component and Gaussian mixture distributions. In this table, GMD indicates Gaussian mixture distribution and the suffix refers to the number of Gaussian components. Note that for  $W_{30}$ ,  $W_{50}$  and  $W_{100}$ , the Gaussian mixture distributions achieve the best values of Log-Likelihood, AIC, BIC and EDC than the single-component distributions. It is worth mentioning that the three last evaluation criteria consider the number of parameters into their formulation to inform the best distribution, and, even so, the Gaussian mixture distributions achieve the best results. Overall, the Inverse Gaussian distribution attained the best modeling among the single-component distributions for  $W_{30}$  and  $W_{50}$ , while Log-Logistic distribution did the same for  $W_{100}$ . Meanwhile, the Gaussian mixture distribution with four components yielded the best modeling for  $W_{30}$ ,  $W_{50}$  and  $W_{100}$ .

Fig. 14a shows that the Gaussian mixture distribution with four components models the histogram of the nSNR coherence bandwidth more efficiently than the Inverse Gaussian, which is the best single-component distribution for  $W_{30}$ . The two first peaks of the histogram are properly modeled by the Gaussian mixture distribution with four components, while the Inverse Gaussian distribution presents a result not as good in terms of in shape and amplitude. Performing similar analysis, figures 14b and 14c show that the Gaussian mixture distribution with four components offers a better modeling than the Inverse Gaussian distribution for  $W_{50}$  and the Log-Logistic distribution for  $W_{100}$ .

Table 3: The evaluation criteria for the fits for  $B_{c,\bar{\gamma}}$  in  $W_{30}$ ,  $W_{50}$  and  $W_{100}$  for in-home PLC channels.

$W_{30}$				
Distribution	Log-Likelihood	AIC	BIC	EDC
Log-Normal	-98534.90	197073.80	197077.51	197103.55
Exponential	-100934.90	201871.81	201873.66	201886.68
Gamma	-99082.37	198168.75	198172.45	198198.49
<b>Inverse Gaussian</b>	<b>-98497.74</b>	<b>196999.48</b>	<b>197003.18</b>	<b>197029.22</b>
Logistic	-100342.44	200688.87	200692.58	200718.62
Log-Logistic	-98607.59	197219.18	197222.88	197248.92
Nakagami	-99913.76	199831.53	199835.23	199861.27
Normal	-101341.53	202687.07	202690.77	202716.81
Weibull	-99646.43	199296.86	199300.57	199326.61
GMD 2	-99165.43	198340.85	198375.20	198415.22
GMD 3	-98514.54	197045.08	197100.04	197164.06
<b>GMD 4</b>	<b>-98087.46</b>	<b>196196.92</b>	<b>196272.49</b>	<b>196360.52</b>
$W_{50}$				
Distribution	Log-Likelihood	AIC	BIC	EDC
Log-Normal	-99734.18	199472.36	199476.07	199502.11
Exponential	-101997.96	203997.92	203999.77	204012.79
Gamma	-100071.08	200146.16	200149.86	200175.90
<b>Inverse Gaussian</b>	<b>-99673.41</b>	<b>199350.82</b>	<b>199354.52</b>	<b>199380.56</b>
Logistic	-101205.73	202415.47	202419.17	202445.21
Log-Logistic	-99906.66	199817.33	199821.03	199847.07
Nakagami	-100627.09	201258.18	201261.88	201287.92
Normal	-101770.72	203545.43	203549.14	203575.18
Weibull	-100496.74	200997.48	201001.18	201027.22
GMD 2	-100296.14	200602.28	200636.63	200676.64
GMD 3	-99592.25	199200.50	199255.47	199319.48
<b>GMD 4</b>	<b>-99141.55</b>	<b>198305.09</b>	<b>198380.67</b>	<b>198468.69</b>
$W_{100}$				
Distribution	Log-Likelihood	AIC	BIC	EDC
Log-Normal	-100506.47	201016.93	201020.64	201046.68
Exponential	-102307.68	204617.36	204619.22	204632.24
Gamma	-100687.31	201378.63	201382.33	201408.37
Inverse Gaussian	-100679.97	201363.94	201367.65	201393.69
Logistic	-101772.61	203549.23	203552.93	203578.97
<b>Log-Logistic</b>	<b>-100499.32</b>	<b>201002.64</b>	<b>201006.35</b>	<b>201032.39</b>
Nakagami	-101279.54	202563.07	202566.78	202592.82
Normal	-102562.94	205129.89	205133.59	205159.63
Weibull	-101063.41	202130.83	202134.53	202160.57
GMD 2	-100940.68	201891.36	201925.71	201965.72
GMD 3	-100338.84	200693.68	200748.65	200812.66
<b>GMD 4</b>	<b>-100063.96</b>	<b>200149.92</b>	<b>200225.49</b>	<b>200313.51</b>

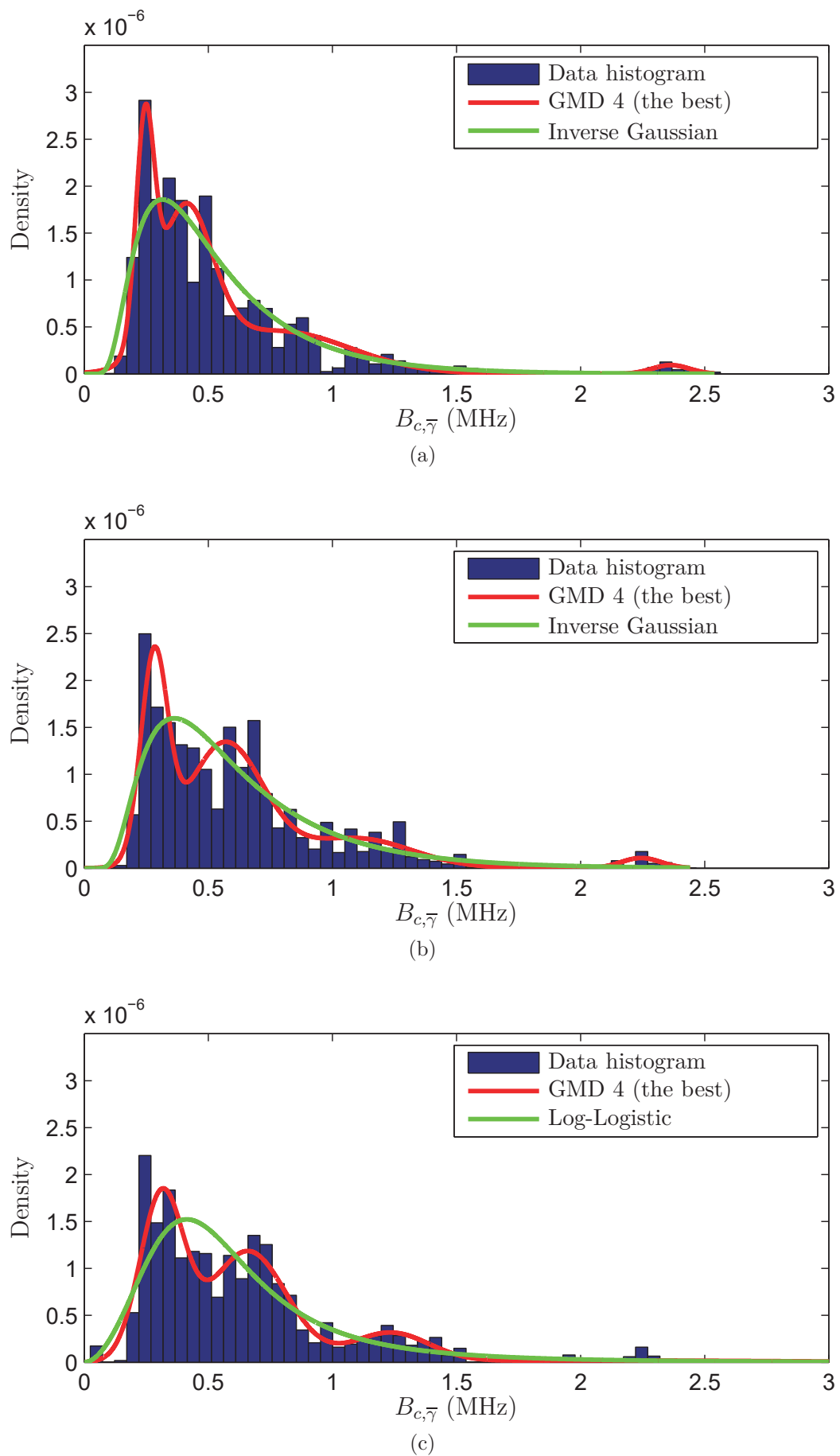


Figure 14: The In-home PLC channel: The best modeling (by single-component and Gaussian mixture distributions) of the nSNR coherence bandwidth ( $\alpha = 0.9$ ) for (a)  $W_{30}$ ; (b)  $W_{50}$ ; and (c)  $W_{100}$ .

### 3.3.2 Outdoor and low-voltage PLC channels

For outdoor and low-voltage PLC channels, this subsection makes use of a data set obtained from a measurement campaign carried out in a residential district of the Juiz de Fora city, Minas Gerais state, Brazil [65]. In this measurement campaign 146 CFRs and 175 additive noises were obtained. The total number of evaluated nSNRs were 25,550 for each frequency band ( $W_{30}$ ,  $W_{50}$  and  $W_{100}$ ).

Table 4 lists the results of the evaluation criteria for modeling the histogram of nSNR coherence bandwidth with single-component and Gaussian mixture distributions. For  $W_{30}$  and  $W_{100}$ , the modeling with Nakagami distribution offers the best result for the majority of criteria. The Nakagami distribution is closely followed by the modeling with Gamma distribution. Although some Gaussian mixture distributions output high Log-Likelihood value, the AIC, BIC and EDC criteria show that due to the number of parameter of the Gaussian mixture distribution, it is not the best choice. In regards to  $W_{50}$ , the Gamma distribution shows the best results for the majority of evaluation criteria, followed by the Nakagami distribution.

Figs. 15a-15c show the two best single-component modelings of the histogram of the nSNR coherence bandwidth for  $W_{30}$ ,  $W_{50}$  and  $W_{100}$ , respectively. Focusing on the frequency bands  $W_{30}$  and  $W_{100}$ , the Gamma distribution achieves a modeling slightly shifted to the left and with the biggest amplitude, while the Nakagami distribution yields a more proper modeling. For  $W_{50}$ , there is a different situation because the characteristics of the Gamma distribution makes it better than the Nakagami distribution for modeling the histogram of the nSNR coherence bandwidth.

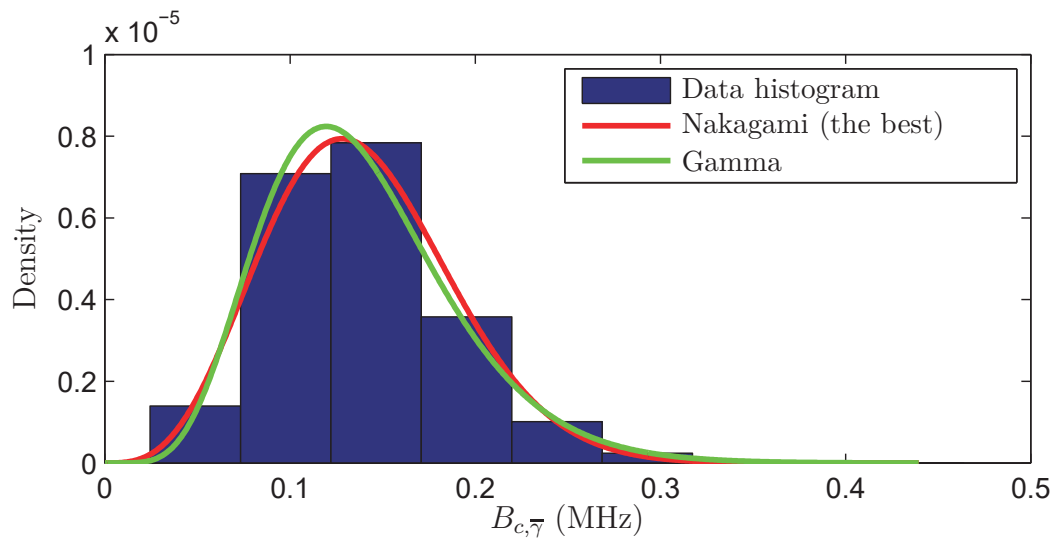
### 3.3.3 Hybrid PLC-wireless channels

The measurement campaign of hybrid PLC-wireless channels were carried out together with the measurement campaign of in-home PLC channels, shortly described in Subsection 3.3.1. Due to its uniqueness, two different data transmission directions must be defined when working with PLC-wireless channels [58, 59]: the first one is the PLC-to-wireless direction, in which the transmission signal is injected in the electric power grid and part of the energy of this signal is irradiated and captured by an antenna; the second one is the wireless-to-PLC direction, in which the transmission signal is injected in the air using an antenna and part of this signal is induced in the electric power grids and captured by a PLC modem.

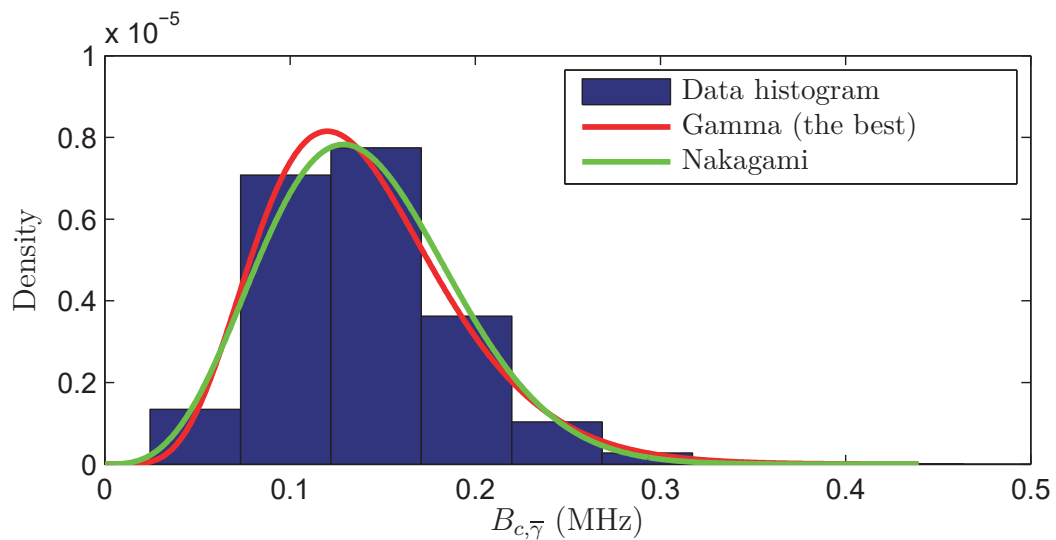
For statistical analyses, the total number of nSNRs used is 23,556. It is important to emphasize that the estimated CIR of such channels is the same, regardless of the data transmission direction. However, the additive noise is different for each data transmission direction and, therefore, the nSNR is very different for the two directions.

Table 4: The evaluation criteria for the fits for  $B_{c,\bar{\gamma}}$  in  $W_{30}$ ,  $W_{50}$  and  $W_{100}$  for outdoor PLC channels.

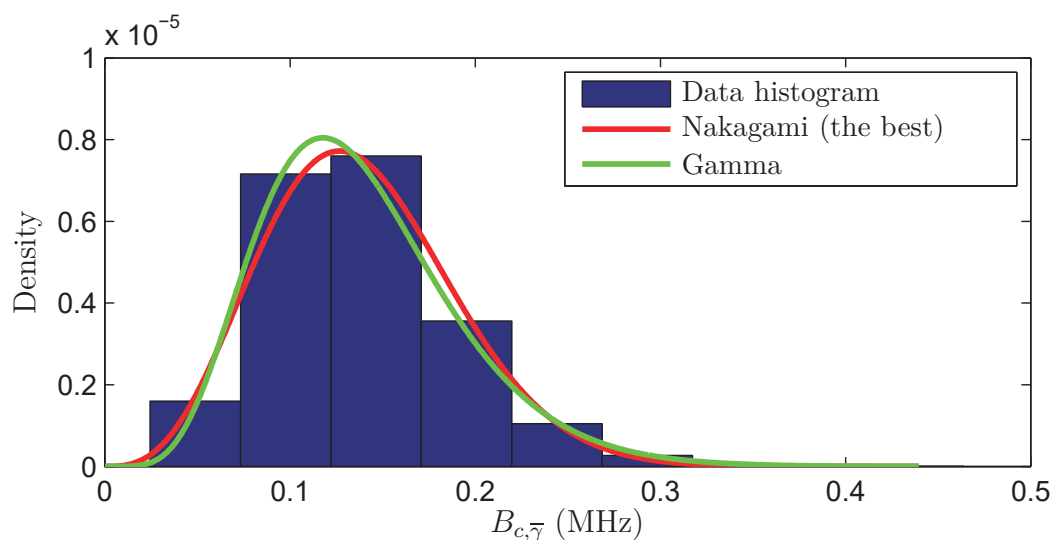
$W_{30}$				
Distribution	Log-Likelihood	AIC	BIC	EDC
Log-Normal	-312858.11	625720.22	625725.03	625780.15
Exponential	-328049.06	656100.13	656102.53	656130.09
<b>Gamma</b>	<b>-312219.76</b>	<b>624443.52</b>	<b>624448.33</b>	<b>624503.45</b>
Inverse Gaussian	-313018.69	626041.37	626046.19	626101.31
Logistic	-312840.05	625684.09	625688.91	625744.03
Log-Logistic	-312686.29	625376.59	625381.40	625436.53
<b>Nakagami</b>	<b>-312185.08</b>	<b>624374.16</b>	<b>624378.98</b>	<b>624434.10</b>
Normal	-312842.01	625688.01	625692.83	625747.95
Weibull	-312563.81	625131.61	625136.43	625191.55
GMD 2	-312222.74	624455.47	624496.21	624605.31
GMD 3	-312176.48	624368.97	624434.15	624608.72
GMD 4	-312181.57	624385.13	624474.77	624714.79
$W_{50}$				
Distribution	Log-Likelihood	AIC	BIC	EDC
Log-Normal	-313073.39	626150.79	626155.60	626210.73
Exponential	-328220.03	656442.06	656444.47	656472.03
<b>Gamma</b>	<b>-312497.17</b>	<b>624998.33</b>	<b>625003.15</b>	<b>625058.27</b>
Inverse Gaussian	-313230.13	626464.27	626469.08	626524.20
Logistic	-313203.60	626411.21	626416.02	626471.15
Log-Logistic	-312916.95	625837.90	625842.72	625897.84
<b>Nakagami</b>	<b>-312533.09</b>	<b>625070.18</b>	<b>625074.99</b>	<b>625130.12</b>
Normal	-313275.27	626554.53	626559.35	626614.47
Weibull	-312965.24	625934.48	625939.29	625994.42
GMD 2	-312542.99	625095.98	625136.72	625245.82
GMD 3	-312470.47	624956.94	625022.13	625196.69
GMD 4	-312541.92	625105.85	625195.48	625435.50
$W_{100}$				
Distribution	Log-Likelihood	AIC	BIC	EDC
Log-Normal	-313487.02	626978.04	626982.86	627037.98
Exponential	-327935.39	655872.78	655875.18	655902.74
<b>Gamma</b>	<b>-312854.81</b>	<b>625713.62</b>	<b>625718.44</b>	<b>625773.56</b>
Inverse Gaussian	-313637.80	627279.61	627284.42	627339.54
Logistic	-313559.78	627123.55	627128.37	627183.49
Log-Logistic	-313354.47	626712.94	626717.75	626772.88
<b>Nakagami</b>	<b>-312843.40</b>	<b>625690.79</b>	<b>625695.61</b>	<b>625750.73</b>
Normal	-313580.47	627164.93	627169.75	627224.87
Weibull	-313198.60	626401.21	626406.02	626461.15
GMD 2	-312907.13	625824.26	625865.01	625974.11
GMD 3	-312848.88	625713.77	625778.95	625953.52
GMD 4	-312845.10	625712.20	625801.84	626041.86



(a)



(b)



(c)

Figure 15: The outdoor PLC channel: The best modeling (by single-component distribution) of the nSNR coherence bandwidth ( $\alpha = 0.9$ ) for (a)  $W_{30}$ ; (b)  $W_{50}$ ; and (c)  $W_{100}$ .

For the data transmission in the PLC-to-wireless direction, Table 5 shows the results of the evaluation criteria for the best modeling by single-component and Gaussian mixture distributions for  $W_{30}$ ,  $W_{50}$  and  $W_{100}$ . Note that, as in the outdoor PLC channels, the single-component distributions yield the best results and the Gaussian mixture distributions do not converge properly for the frequency band  $W_{30}$ . The lack of convergence is due to the fact that low frequency signals require longer antennas. As the antenna used in the measurement setup has short length, the acquired noise is distorted in low frequencies. Therefore, if the frequency band is low and the antenna length is not appropriate, then there is a larger distortion on the noise measurement, which interferes with the nSNR coherence bandwidth. This effect is practically non-existent for the frequency bands  $W_{50}$  and  $W_{100}$ . As the nSNR shows different behavior in these frequency bands, the modeling of the histogram of the nSNR coherence bandwidth with the Gaussian mixture distributions as well as with the single-component distributions offered good results.

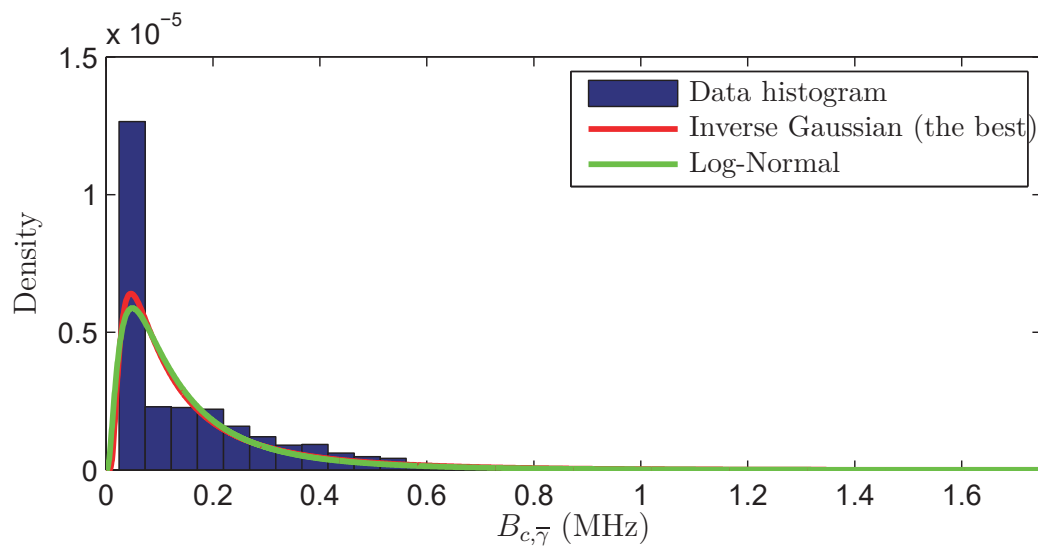
The single-component distributions with the best results for all evaluation criteria in all frequency bands ( $W_{30}$ ,  $W_{50}$  and  $W_{100}$ ) is the Inverse Gaussian distribution. For the frequency band  $W_{30}$ , the Log-Normal distribution offers the second best results. When analyzing the multimodal distributions, the Gaussian mixture distribution with four components achieves the best results for all evaluation criteria for the frequency bands  $W_{50}$  and  $W_{100}$ . To illustrate it, Fig. 16 shows the histogram of the nSNR coherence bandwidth and the best modelings for  $W_{30}$ ,  $W_{50}$  and  $W_{100}$ . Fig. 16a shows a small but visible difference between the two best modelings, Figs. 16b and 16c reveal that the Gaussian mixture distribution with four components offers a modeling slightly better in shape and amplitude than the Inverse Gaussian distribution for  $W_{50}$  and  $W_{100}$ .

When the data transmission is in the wireless-to-PLC direction, there are different results, because the additive noise in the PLC channel and wireless channel is different [58]. The evaluation criteria for modeling the nSNR coherence bandwidth with single-component distributions and Gaussian mixture distributions are listed in Table 6, while Fig. 17 shows the best modeling of single-component and Gaussian mixture distributions. For  $W_{30}$  the single-component distribution with the best results for all evaluation criteria is the Gamma distribution, while for  $W_{50}$  and  $W_{100}$  the Nakagami distribution attains the best results. Among all the Gaussian mixture distributions, the one with four components provides the best results for the majority of evaluation criteria in the chosen frequency bands  $W_{30}$ ,  $W_{50}$  and  $W_{100}$ .

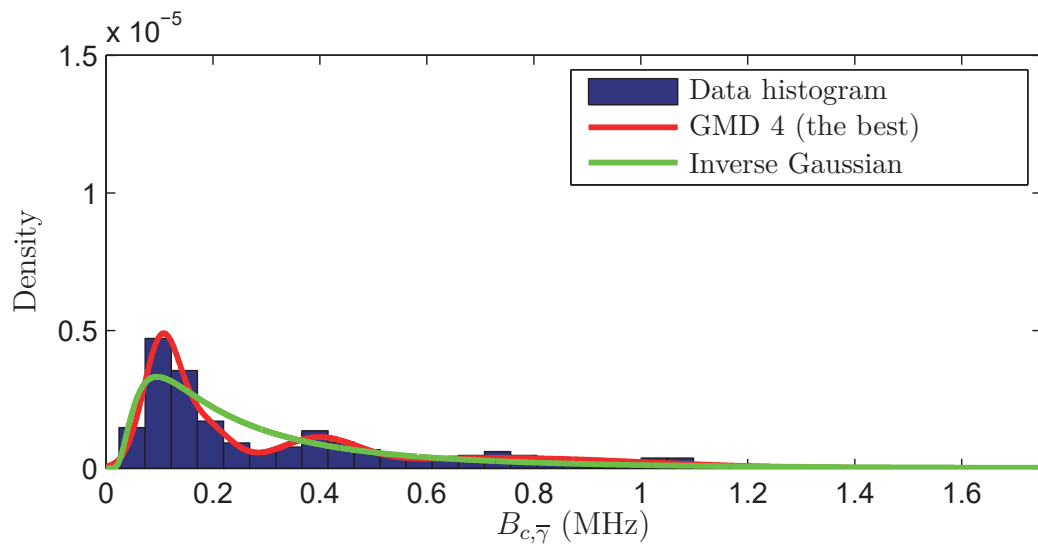
Fig. 17a shows that the Gamma distribution is not capable of properly modeling the two first peaks of the histogram of the nSNR coherence bandwidth for  $W_{30}$ , while the Gaussian mixture distribution with four components achieves the best result. A similar conclusion appears for  $W_{50}$  and  $W_{100}$  when the results obtained with the Nakagami distribution are compared with the results yield by Gaussian mixture distribution with

Table 5: The evaluation criteria for the fits for  $B_{c,\bar{\gamma}}$  in  $W_{30}$ ,  $W_{50}$  and  $W_{100}$  for hybrid PLC-wireless channels in the PLC-to-wireless direction.

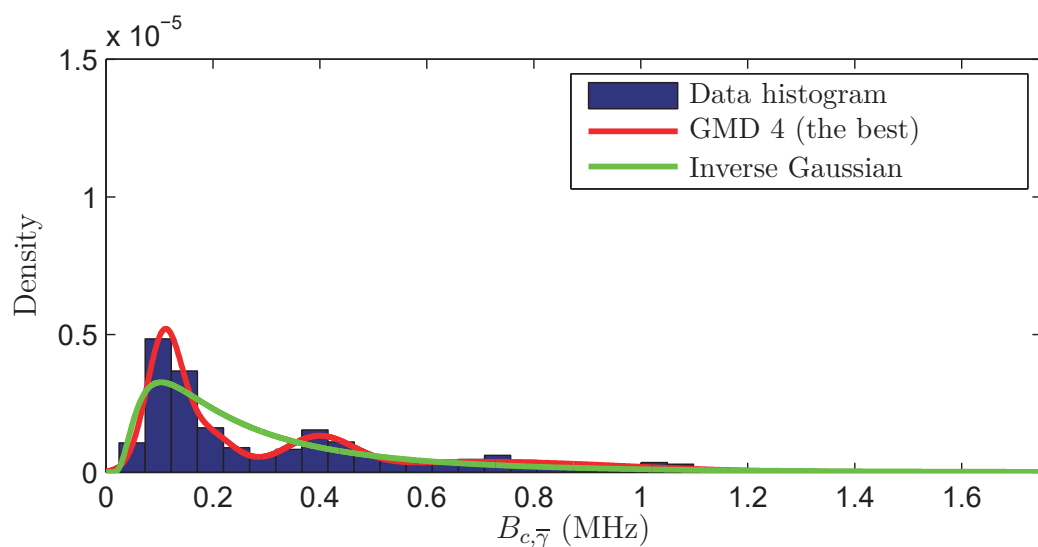
$W_{30}$				
Distribution	Log-Likelihood	AIC	BIC	EDC
<b>Log-Normal</b>	<b>-306270.67</b>	<b>612545.33</b>	<b>612550.08</b>	<b>612602.82</b>
Exponential	-309242.30	618486.60	618488.97	618515.35
Gamma	-308901.13	617806.26	617811.01	617863.76
<b>Inverse Gaussian</b>	<b>-305104.51</b>	<b>610213.02</b>	<b>610217.77</b>	<b>610270.51</b>
Logistic	-318495.33	636994.65	636999.40	637052.14
Log-Logistic	-307229.16	614462.32	614467.06	614519.81
Nakagami	-311497.09	622998.17	623002.92	623055.67
Normal	-321320.18	642644.36	642649.11	642701.85
Weibull	-309173.85	618351.70	618356.45	618409.19
GMD 2	-321320.18	642650.36	642690.71	642794.09
GMD 3	-321320.18	642656.36	642720.92	642886.33
GMD 4	-321320.18	642662.36	642751.13	642978.57
$W_{50}$				
Distribution	Log-Likelihood	AIC	BIC	EDC
Log-Normal	-321643.44	643290.89	643295.64	643348.38
Exponential	-323792.21	647586.42	647588.80	647615.17
Gamma	-322771.73	645547.46	645552.21	645604.96
<b>Inverse Gaussian</b>	<b>-321067.91</b>	<b>642139.81</b>	<b>642144.56</b>	<b>642197.30</b>
Logistic	-330154.51	660313.02	660317.76	660370.51
Log-Logistic	-322548.29	645100.59	645105.33	645158.08
Nakagami	-324164.73	648333.45	648338.20	648390.94
Normal	-330872.66	661749.31	661754.06	661806.81
Weibull	-323122.76	646249.52	646254.27	646307.02
GMD 2	-320931.56	641873.13	641913.48	642016.86
GMD 3	-319734.78	639485.56	639550.12	639715.53
<b>GMD 4</b>	<b>-319411.31</b>	<b>638844.63</b>	<b>638933.40</b>	<b>639160.84</b>
$W_{100}$				
Distribution	Log-Likelihood	AIC	BIC	EDC
Log-Normal	-320919.29	641842.57	641847.32	641900.06
Exponential	-323404.18	646810.36	646812.74	646839.11
Gamma	-322028.12	644060.23	644064.98	644117.72
<b>Inverse Gaussian</b>	<b>-320361.20</b>	<b>640726.40</b>	<b>640731.14</b>	<b>640783.89</b>
Logistic	-328946.57	657897.14	657901.89	657954.63
Log-Logistic	-321841.77	643687.54	643692.28	643745.03
Nakagami	-323433.82	646871.65	646876.39	646929.14
Normal	-329674.21	659352.42	659357.16	659409.91
Weibull	-322447.99	644899.99	644904.74	644957.48
GMD 2	-319948.11	639906.21	639946.57	640049.95
GMD 3	-318662.09	637340.17	637404.74	637570.15
<b>GMD 4</b>	<b>-318291.70</b>	<b>636605.40</b>	<b>636694.17</b>	<b>636921.61</b>



(a)



(b)



(c)

Figure 16: The hybrid PLC-wireless channel (PLC-to-wireless direction): The best modeling (by single-component and Gaussian mixture distributions) of the nSNR coherence bandwidth ( $\alpha = 0.9$ ) for (a)  $W_{30}$ ; (b)  $W_{50}$ ; and (c)  $W_{100}$ .

four components, as illustrated in Figs. 17b and 17c, respectively.

### 3.3.4 The nSNR coherence bandwidth for the three PLC channels

This subsection addresses an analysis of the nSNR coherence bandwidth for in-home PLC channel, outdoor PLC channel and hybrid PLC-wireless channel. In this context, Table 7 lists the minimal, mean and maximum values of the  $B_{c,\bar{\gamma}}$  for  $W_{30}$ ,  $W_{50}$  and  $W_{100}$  when the data set described in Subsections 3.3.1-3.3.3 are considered. Moreover, this table lists, in the column “90 percent”, the value of  $x$  such that  $P(B_{c,\bar{\gamma}} < x) = 0.9$ , in which  $P(\cdot)$  denotes the probability evaluated from the best modeling for each type of channel and frequency band. Note that the minimal value of  $B_{c,\bar{\gamma}}$  is 48.83 kHz in the majority of cases. This value is the frequency resolution of the channel estimation procedure. However, in-home PLC channel for  $W_{30}$  and  $W_{50}$  and hybrid PLC-wireless channel in the wireless-to-PLC direction for  $W_{30}$  offer higher minimal  $B_{c,\bar{\gamma}}$ . Moreover, all frequency bands ( $W_{30}$ ,  $W_{50}$  and  $W_{100}$ ) show similar nSNR coherence bandwidth behavior with respect to the types of channels. An exception of this rule is  $W_{30}$  for hybrid PLC-wireless channel in the PLC-to-wireless direction, which shows minimal and “90 percent” values approximately half of the values achieved by the frequency bands  $W_{50}$  and  $W_{100}$ . Another important observation is that the smallest nSNR coherence bandwidth is observed in outdoor PLC channels, whereas the highest one is noted in hybrid PLC-wireless channels when the wireless-to-PLC direction is considered.

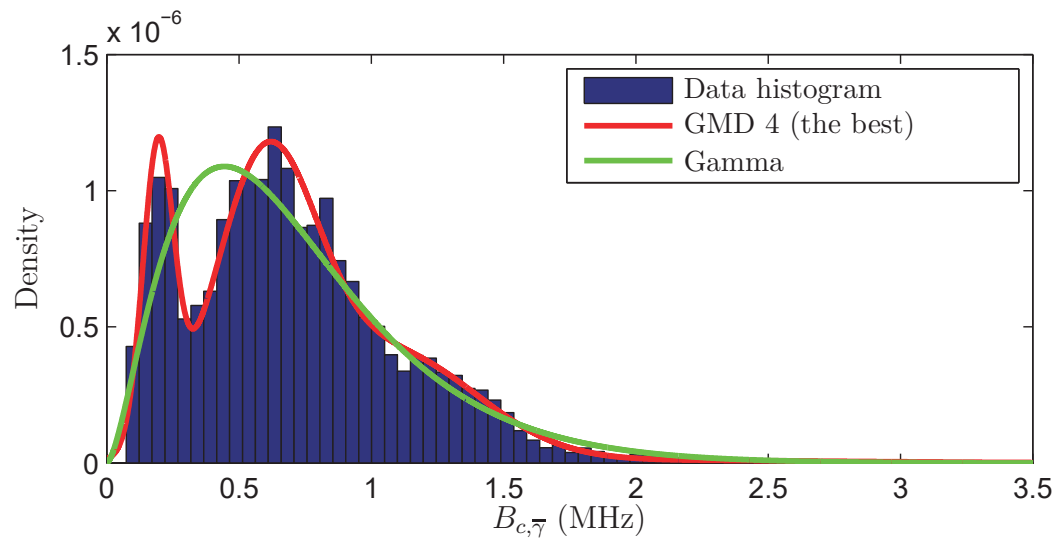
## 3.4 SUMMARY

The main conclusions of this chapter are summarized as follows:

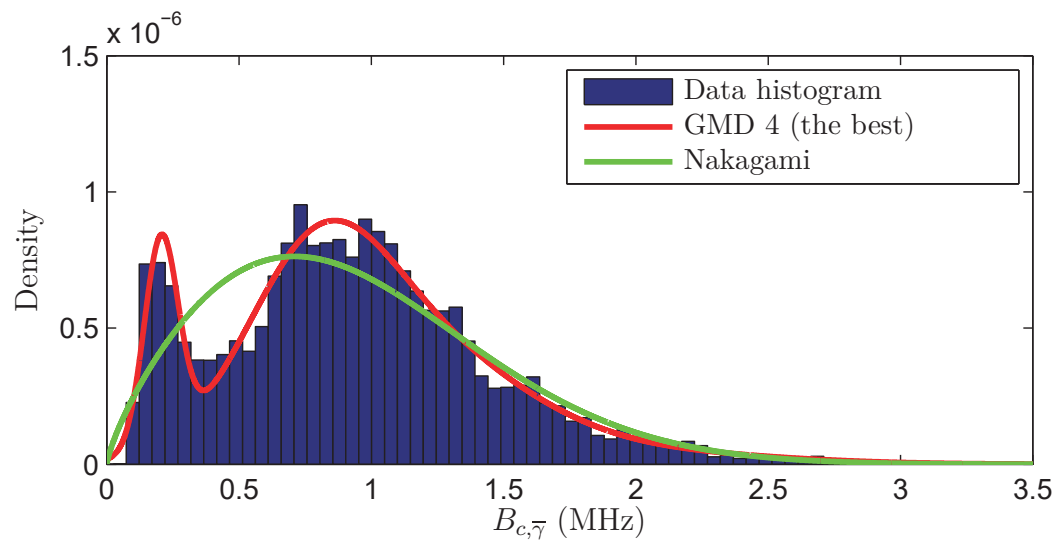
- This chapter introduced the nSNR coherence bandwidth and showed that it is a parameter more appropriate than the coherence bandwidth to inform the flatness of the nSNR for resource allocation purposes. Also, it highlighted that the nSNR coherence bandwidth presents different behavior in comparison with the coherence bandwidth.
- For in-home PLC channels, this chapter showed that the Gaussian mixture distribution with four components is the best model, among the considered distributions, for the PDF of the nSNR coherence bandwidth. On the other hand, for outdoor PLC channels, Nakagami or Gamma distributions are the best models for the PDF of the nSNR coherence bandwidth.
- For hybrid PLC-wireless channels, the nSNR coherence bandwidth PDF modeling is more complex. The Inverse Gaussian distribution offers the best model for the frequency band of 1.7-30 MHz, while the Gaussian mixture distribution with four

Table 6: The evaluation criteria for the fits for  $B_{c,\bar{\gamma}}$  in  $W_{30}$ ,  $W_{50}$  and  $W_{100}$  for hybrid PLC-wireless channels in the wireless-to-PLC direction.

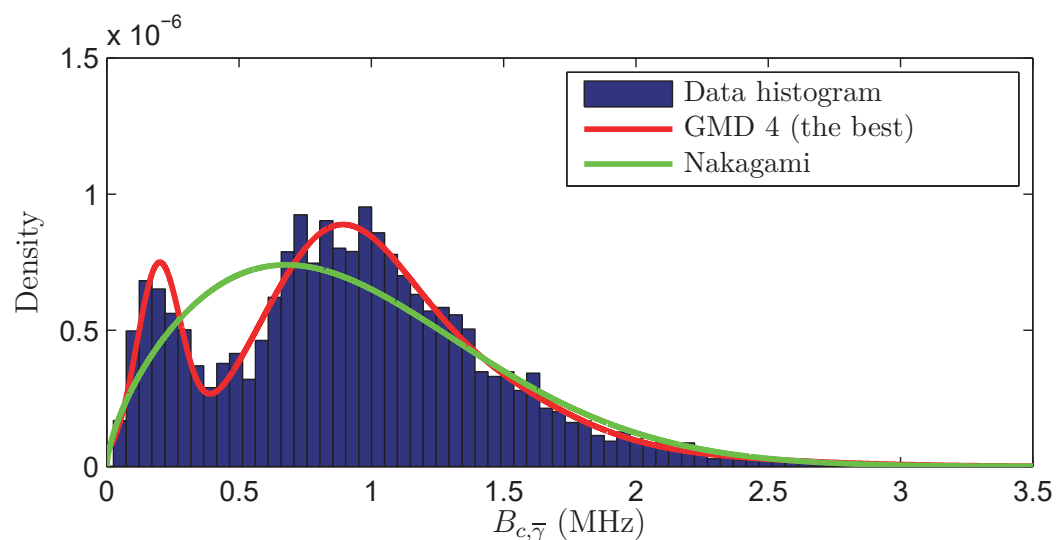
$W_{30}$				
Distribution	Log-Likelihood	AIC	BIC	EDC
Log-Normal	-338382.36	676768.71	676773.46	676826.21
Exponential	-342299.18	684600.37	684602.74	684629.11
<b>Gamma</b>	<b>-337489.26</b>	<b>674982.52</b>	<b>674987.27</b>	<b>675040.01</b>
Inverse Gaussian	-338794.61	677593.23	677597.97	677650.72
Logistic	-339603.05	679210.10	679214.85	679267.60
Log-Logistic	-338482.81	676969.61	676974.36	677027.10
Nakagami	-337835.98	675675.96	675680.70	675733.45
Normal	-340496.04	680996.09	681000.84	681053.58
Weibull	-337658.32	675320.64	675325.39	675378.13
GMD 2	-338751.22	677512.44	677552.79	677656.17
GMD 3	-337411.74	674839.49	674904.05	675069.46
<b>GMD 4</b>	<b>-336700.52</b>	<b>673423.04</b>	<b>673511.82</b>	<b>673739.26</b>
$W_{50}$				
Distribution	Log-Likelihood	AIC	BIC	EDC
Log-Normal	-345404.82	690813.63	690818.38	690871.13
Exponential	-348681.19	697364.37	697366.75	697393.12
Gamma	-343643.98	687291.95	687296.70	687349.44
Inverse Gaussian	-346232.74	692469.48	692474.23	692526.98
Logistic	-344521.98	689047.96	689052.71	689105.46
Log-Logistic	-345077.02	690158.03	690162.78	690215.53
<b>Nakagami</b>	<b>-343173.78</b>	<b>686351.56</b>	<b>686356.31</b>	<b>686409.06</b>
Normal	-344680.58	689365.16	689369.90	689422.65
Weibull	-343186.45	686376.89	686381.64	686434.39
GMD 2	-343872.73	687755.46	687795.82	687899.20
GMD 3	-342361.33	684738.66	684803.22	684968.63
<b>GMD 4</b>	<b>-342278.36</b>	<b>684578.72</b>	<b>684667.50</b>	<b>684894.93</b>
$W_{100}$				
Distribution	Log-Likelihood	AIC	BIC	EDC
Log-Normal	-347043.67	694091.34	694096.08	694148.83
Exponential	-348733.30	697468.59	697470.96	697497.34
Gamma	-344588.40	689180.80	689185.55	689238.30
Inverse Gaussian	-348744.35	697492.69	697497.44	697550.19
Logistic	-344987.88	689979.76	689984.51	690037.26
Log-Logistic	-346281.91	692567.81	692572.56	692625.30
<b>Nakagami</b>	<b>-343790.17</b>	<b>687584.34</b>	<b>687589.08</b>	<b>687641.83</b>
Normal	-345121.24	690246.49	690251.23	690303.98
Weibull	-343872.72	687749.45	687754.19	687806.94
GMD 2	-344465.13	688940.26	688980.61	689083.99
GMD 3	-342946.51	685909.03	685973.59	686139.00
<b>GMD 4</b>	<b>-342861.10</b>	<b>685744.20</b>	<b>685832.98</b>	<b>686060.42</b>



(a)



(b)



(c)

Figure 17: The hybrid PLC-wireless channel (wireless-to-PLC direction): The best modeling (by single-component and Gaussian mixture distributions) of the nSNR coherence bandwidth ( $\alpha = 0.9$ ) for (a)  $W_{30}$ ; (b)  $W_{50}$ ; and (c)  $W_{100}$ .

Table 7: Some information about  $B_{c,\bar{\gamma}}$  of in-home PLC channels, outdoor PLC channels and hybrid PLC-wireless channels (both directions) for  $W_{30}$ ,  $W_{50}$  and  $W_{100}$ .

In-home PLC channel				
Frequency band	Minimal (kHz)	Mean (kHz)	Maximal (kHz)	90 percent (kHz)
$W_{30}$	97.65	530.84	2539.06	977.05
$W_{50}$	146.48	616.36	2441.40	1130.37
$W_{100}$	48.83	643.78	3759.76	1203.12
Outdoor PLC channel				
Frequency band	Minimal (kHz)	Mean (kHz)	Maximal (kHz)	90 percent (kHz)
$W_{30}$	48.83	138.62	439.45	205.56
$W_{50}$	48.83	139.55	439.45	209.47
$W_{100}$	48.83	138.00	439.45	206.54
Hybrid PLC-wireless channel (PLC-to-wireless direction)				
Frequency band	Minimal (kHz)	Mean (kHz)	Maximal (kHz)	90 percent (kHz)
$W_{30}$	48.83	177.12	2246.09	390.13
$W_{50}$	48.83	327.83	2636.72	801.27
$W_{100}$	48.83	322.50	3076.17	767.09
Hybrid PLC-wireless channel (wireless-to-PLC direction)				
Frequency band	Minimal (kHz)	Mean (kHz)	Maximal (kHz)	90 percent (kHz)
$W_{30}$	97.65	717.36	4248.05	1288.08
$W_{50}$	48.83	939.75	3613.28	1610.35
$W_{100}$	48.83	941.82	3662.11	1620.12

components is more suitable for the frequency band of 1.7-50 MHz and 1.7-100 MHz, if the data transmission occurs in the PLC-to-wireless direction. On the other hand, if the data transmission occurs in the wireless-to-PLC direction, then the Gaussian mixture distribution with four components offers the best modeling for the frequency bands  $W_{30}$ ,  $W_{50}$  and  $W_{100}$ .

## 4 A SPECTRAL COMPRESSIVE RESOURCE ALLOCATION TECHNIQUE FOR PLC SYSTEMS

Aiming reducing the computational complexity of resource allocation techniques in OFDM-based PLC system, Chapter 2 exploited the relationship among microslots within one cycle and among consecutive cycles of mains signal and, in consequence, it proposed the TCRA technique to take advantage of such relationship. This is a sub-optimal resource allocation technique that can offer significant computational complexity savings by trading data rate loss with computational complexity reduction. On the other hand, [56] and [57] have analyzed a chunk-based resource allocation for wireless communication systems based on OFDM scheme, which exploits the existing relationship between adjacent subchannels (CSI exploitation) at the frequency domain in order to decrease the computational complexity and the signaling overhead (i.e. network bandwidth for exchanging control information to share the CSI and modulation parameters for all users sharing the same PLC network). These two works suggested the specification of chunk bandwidth based on the coherence bandwidth, benefited by the fact that the noise in wireless channels is modeled as an additive white Gaussian random process. Essentially, they proposed a technique that is capable of grouping a set of subcarriers, based on the coherence bandwidth and, as a result, it succeed in reducing the computational complexity of resource allocation technique when the existent relationship among the subchannels is exploited in the frequency domain. However, Chapter 3 showed that the nSNR coherence bandwidth is an appropriate parameter to be used for resource allocation problems in PLC systems, because it precisely informs the flatness of the nSNR. Also, the flatness of the nSNR is the parameter appropriated to group adjacent subcarriers in a set, which can be represented by one of the subcarriers belonging to the set.

This chapter proposes a novel chunk-based resource allocation technique, called spectral compressive resource allocation (SCRA), which is suitable for OFDM-based PLC systems. The SCRA technique exploits the existing relationship among adjacent subchannels for decreasing the computational complexity and for reducing the need for network bandwidth for exchanging signaling overhead. Furthermore, on the basis of a measurement data set composed of estimates of CFR and additive noise of in-home PLC channels, this chapter analyzes the SCRA technique performance in terms of the data rate loss, the computational complexity reduction and the symbol error rate (SER) for three different frequency bands: 1.7-30 MHz, 1.7-50 MHz and 1.7-100 MHz. For the same reasons exposed in Chapter 3, the first and the second frequency bands comply with European and Brazilian regulations for PLC systems [60,61], respectively, while the latter is a possibility for future regulation for PLC systems [13]. The main contributions of this chapter are summarized as follows:

- The introduction of the chunk-based SCRA technique for PLC systems based on

OFDM scheme.

- The analyses of the SER and data rate loss performances of the SCRA technique when the nSNR that represents each chunk is the minimal, mean, median or maximum nSNR value associated with the subcarriers belonging to the chunk.
- The analysis of the SCRA technique performance when the chunk bandwidth is constant or adaptive (it varies according to the nSNR coherence bandwidth) for three different frequency bands: 1.7-30 MHz, 1.7-50 MHz and 1.7-100 MHz.

The SCRA technique, introduced in this chapter is fundamentally different from the TCRA technique discussed in Chapter 2. While the SCRA technique addresses the frequency domain, the TCRA technique focuses on the time domain. In other words, the use of the SCRA technique together with TCRA can yield additional computational complexity savings in comparison with the independent use of only one of them.

#### 4.1 PROBLEM FORMULATION

The discussion will be centered on a data communication system over an LTV PLC channel using an OFDM scheme. In this sense, let an OFDM-based PLC system be working in a frequency band from 0 to  $B$  Hertz with  $N$  subcarriers and symbol length equal to  $2N$ , since the data transmission is in the baseband [27,28,35]. In this system, the subchannel bandwidth is  $B_s = 2B/2N = B/N$ , in which  $N \geq \lceil B/B_{c,H} \rceil$  (where  $B_{c,H}$  is the coherence bandwidth, as discussed in the Chapter 3 and  $\lceil a \rceil = \min\{n \in \mathbb{Z} | n \geq a\}$ ), and the CFR of the LTI PLC channel is approximately flat within a bandwidth equal to  $B_s \leq B_{c,H}$ . Also, the LTV PLC channel behaves as an LTI channel during a period of time shorter than the coherence time ( $T_c$ ) and the vectorial representation of the CIR of such LTI PLC channel is  $\mathbf{h} = [h_0 \ h_1 \ \cdots \ h_{L_h-1}]^T$ , where  $L_h$  is the length of the CIR and  $(\cdot)^T$  denotes the transposition operator. The CFR can be expressed by  $\mathbf{H} = [H_0 \ H_1 \ \cdots \ H_{2N-1}]^T = \mathbf{W} [\mathbf{h}^T \mathbf{0}_{2N-L_h}^T]^T$ , where  $\mathbf{0}_{2N-L_h}$  is the  $(2N - L_h)$ -length column vector composed of zeros and  $\mathbf{W}$  denotes the  $2N$ -size discrete Fourier transform (DFT) matrix. Thus, the gain profile of such LTI PLC channel for all subchannels can be expressed as a diagonal matrix  $\mathbf{\Lambda}_{|H|^2} = \mathbf{diag}\{|H_0|^2, |H_1|^2, \dots, |H_{2N-1}|^2\}$  in which  $\mathbf{diag}\{\cdot\}$  denotes a diagonal matrix.

This chapter models the additive noise as a colored Gaussian random process represented in the frequency domain by  $\mathbf{V} = [V_0 \ V_1 \ \cdots \ V_{2N-1}]^T$ . In addition, with  $\mathbb{E}\{\cdot\}$  representing the expectation operator, assume that the noise components are uncorrelated, i.e.,  $\mathbb{E}\{V_k V_j\} = \mathbb{E}\{V_k\}\mathbb{E}\{V_j\}$  for  $k \neq j$ ;  $k, j = 0, 1, \dots, 2N - 1$ , and each component  $V_k$  ( $k^{th}$  element of  $\mathbf{V}$ ) is a random variable having mean  $\mathbb{E}\{V_k\} = 0$  and variance  $\sigma_k^2 = \mathbb{E}\{|V_k|^2\}$  (the majority of papers on resource allocation in PLC systems and PLC channel characterization assume that the noise is either additive white Gaussian

noise (AWGN) or additive colored Gaussian noise [13, 16, 22, 66]). Furthermore, the noise PSD can be represented as the vector  $\mathbf{S}_v = [S_{v,0} \ S_{v,1} \ \cdots \ S_{v,2N-1}]^T$ , where  $S_{v,k}$  is the PSD at the  $k^{\text{th}}$  subchannel. For convenience, this vector will be rearranged as a diagonal matrix  $\mathbf{\Lambda}_{S_v} = \mathbf{diag}\{S_{v,0}, S_{v,1}, \dots, S_{v,2N-1}\}$ .

Differently of Chapter 2, which formulates the resource allocation problem sharing the total energy among subcarriers, this chapter considers power allocation. In this sense, the nSNR must be evaluated by

$$\bar{\gamma}_k = \frac{|H_k|^2}{S_{v,k} B_s} \quad (4.1)$$

and can be arranged as the nSNR diagonal matrix

$$\begin{aligned} \mathbf{\Lambda}_{\bar{\gamma}, 2N} &= \mathbf{diag}\{\bar{\gamma}_0, \bar{\gamma}_1, \dots, \bar{\gamma}_{2N-1}\} \\ &= \frac{\mathbf{\Lambda}_{|H|^2} \mathbf{\Lambda}_{S_v}^{-1}}{B_s}. \end{aligned} \quad (4.2)$$

However, the data transmission is performed in the baseband and therefore the transmission power and the bits are allocated only to the  $N$  subcarriers and not to the  $2N$  ones. Thereby, the nSNR vector can be expressed by  $\bar{\boldsymbol{\gamma}} = [\bar{\gamma}_0 \ \bar{\gamma}_1 \ \cdots \ \bar{\gamma}_{N-1}]^T$  and the nSNR diagonal matrix can be expressed by  $\mathbf{\Lambda}_{\bar{\boldsymbol{\gamma}}} = \mathbf{diag}\{\bar{\gamma}_0, \bar{\gamma}_1, \dots, \bar{\gamma}_{N-1}\}$ , which are used in the resource allocation problem.

In this context, the data rate maximization is obtained by solving a resource allocation problem, which allocates portion of the total transmission power and bits to each subcarrier. For the sake of simplicity, the operator that returns these allocations, based on the rate-adaptive criterion, can be expressed by

$$[\mathbf{\Lambda}_{b^o}, \mathbf{\Lambda}_{P^o}] = f(\mathbf{\Lambda}_{\bar{\boldsymbol{\gamma}}}, P_t, \Gamma), \quad (4.3)$$

where  $\text{Tr}(\mathbf{\Lambda}_{P^o}) \leq P_t$ ,  $\text{Tr}(\cdot)$  is the trace operator,  $P_t$  is the total transmission power to be shared among the subcarriers;  $\Gamma$  represents a gap factor from the Shannon capacity curve that accounts for the deployment of practical modulation and coding schemes [39, 42, 44];  $\mathbf{\Lambda}_{b^o} = \mathbf{diag}\{b_0^o, b_1^o, \dots, b_{N-1}^o\}$  and  $\mathbf{\Lambda}_{P^o} = \mathbf{diag}\{P_0^o, P_1^o, \dots, P_{N-1}^o\}$ , with  $b_k^o$  and  $P_k^o$  being the optimal number of bits and the portion of the total transmission power allocated to the  $k^{\text{th}}$  subcarrier, respectively. The resource allocation described in (4.3) can be solved by the water-filling technique [39, 54], which yields an optimal data rate for the transmission of  $\mathbf{\Lambda}_{b^o} \in \mathbb{R}_+^{N \times N}$  bits per symbol through all subchannels or by a greedy technique [39, 55] that offers a maximum data rate in the sense of the allocation of integer numbers of bits in the subcarriers ( $\mathbf{\Lambda}_{b^o} \in \mathbb{Z}_+^{N \times N}$ ). It is important to note that there are several contributions to achieve both  $\mathbf{\Lambda}_{b^o}$  and  $\mathbf{\Lambda}_{P^o}$  based on distinct constraints [22, 35, 39, 55].

The optimal data rate valid during  $T_c$  seconds, obtained after solving the resource allocation problem, is expressed by

$$R^o = \frac{1}{T_{\text{OFDM}}} \text{Tr}(\mathbf{\Lambda}_{b^o}), \quad (4.4)$$

$T_{\text{OFDM}} = T_{\text{sym}} + T_{\text{cp}}$  is the OFDM symbol interval, with  $T_{\text{sym}}$  and  $T_{\text{cp}}$  denoting the time intervals for the OFDM symbol and the cyclic prefix, respectively.

Usually, resource allocation techniques allocate a portion of the total transmission power and bits to each subcarriers to satisfy a BER or SER constraint; however, this chapter only adopts the SER constraint, because it simplifies all deductions and the results can be easily extended when the BER constraint applies. Thereby, let  $\chi_k \in \mathbb{R}_+$  be the exact SER for  $k^{\text{th}}$  subchannel calculated from  $b_k^o$  and  $P_k^o$ , then the peak SER and the average SER can be evaluated, respectively, by

$$\dot{\chi} = \max_k(\chi_k), \quad (4.5)$$

and

$$\bar{\chi} = \frac{1}{N} \text{Tr}(\mathbf{\Lambda}_\chi), \quad (4.6)$$

where  $\mathbf{\Lambda}_\chi = \mathbf{diag}\{\chi_0, \chi_1, \dots, \chi_{N-1}\}$  and  $\max(\cdot)$  returns the element with the maximum value of a diagonal matrix.

A method for inserting the SER constraint into the resource allocation problem is to specify a value for  $\Gamma$ , see (4.3). Considering uncoded square quadrature amplitude modulation (QAM), an upper bound of the SER for the  $k^{\text{th}}$  subchannel is expressed by [44, 45, 67]

$$\chi_k < 4Q(\sqrt{3\Gamma}), \quad (4.7)$$

where

$$Q(x) = \frac{1}{\sqrt{2\pi}} \int_x^\infty e^{-y^2/2} dy. \quad (4.8)$$

A peak SER constraint of  $10^{-6}$  can be upper bounded by taking  $\Gamma = 9.3$  dB. In this case, the peak SER upper bound is  $0.87 \times 10^{-6}$ .

There might be problems with the optimal resource allocation, since it considers that the PLC channel is LTI. In fact, the time-varying nature of the PLC channel might require a too frequent update of the allocated bits and the portion of the total transmission power among all subcarriers (once at every  $T_c$  seconds, ideally), which increases the signaling overhead. Consequently, the computational complexity can raise to unsurmountable levels (mainly when the value of  $T_c$  is small). For instance, if  $T_c = 600 \mu\text{s}$  (reasonable assumption for in-home PLC channel), then the number of updates in one second is 1667, which demands considerable network bandwidth for data exchange, mainly in the case in which a large number of user share the same PLC network, as discussed in Chapter2. In this scenario, one approach for reducing the computational complexity is to decrease the order of the resource allocation problem by introducing the concept of chunk, as initially proposed in [56] and [57] for wireless communication systems. The idea is to arrange sets of adjacent subcarriers into subsets called chunks, lumping together adjacent subcarriers sharing similarities in terms of their corresponding subchannels into the same chunk. With this idea in mind, Section 4.2 introduces the SCRA technique.

## 4.2 SPECTRAL COMPRESSIVE RESOURCE ALLOCATION TECHNIQUE

The SCRA technique is a chunk-oriented power and bit allocation technique for reducing the computational complexity by exploiting the existing relationship in the nSNR. It can perform drastic dimensionality reduction of the nSNR vector before running the bit loading algorithm. Unlike other techniques presented in the literature, the SCRA technique does not propose a new algorithm for solving the resource allocation problem. Basically, it introduces a procedure to group adjacent subcarriers into a same chunk in order to reduce the dimensionality of the resource allocation problem and, thereby, it must be combined with any existing bit loading algorithm for solving the resource allocation problem. The dimensionality reduction (for this reason compressive) relies on the segmentation of  $\bar{\gamma}$  into  $N_c = \lceil N/L_c \rceil$  chunks, where  $L_c$  is the chunk length (number of grouped subcarriers) corresponding to a bandwidth of  $L_c B_s$  Hertz. Therefore, each chunk is constituted by a set of adjacent nSNRs.

The choice of  $L_c$  has significant impact on the performance of the proposed technique. There are two modes to use it.

- In the first one, the  $L_c$  value is constant for all LTI PLC channels and it does not depend on the nSNR of a given LTI PLC channel. In this case, a preliminary analysis of adopted model or measured LTI PLC channel specifies the  $L_c$  value according to nSNR ( $\Lambda_{\bar{\gamma}}$ ). This is the simplest way to use the SCRA technique.
- The second mode chooses the  $L_c$  value by assigning a different  $L_c$  value for each estimate of nSNR ( $\Lambda_{\bar{\gamma}}$ ) associated with LTI PLC channel. It consists of choosing a different  $L_c$  value after estimating the nSNR and before running the bit loading algorithm. Thus, the second mode is adaptive and depends on the nSNR. The calculation of  $L_c$  is based on the nSNR coherence bandwidth and is evaluated by

$$L_c = \frac{B_{c,\bar{\gamma}}}{B_s}, \quad (4.9)$$

where  $B_{c,\bar{\gamma}}$  denotes the nSNR coherence bandwidth, as introduced in Chapter 3. Therefore, the more flat the nSNR is, the larger  $L_c$  and the higher the computational complexity reduction are. In the adaptive mode, the threshold  $\alpha$  in (3.6) is used to trade the computational complexity reduction with the data rate loss.

Fig. 18 shows the algorithm devised for choosing the  $L_c$  value using the second mode. This algorithm evaluates the nSNR coherence bandwidth in the discrete time domain and therefore considers circular shift operator to evaluate (3.5), since the DFT is the sampled version of the Fourier transform of a finite-length sequence. In this sense, this algorithm assumes that  $\Lambda_{\bar{\gamma},2N} = \mathbf{diag} \{ \bar{\gamma}_\delta, \bar{\gamma}_{\delta+1}, \dots, \bar{\gamma}_{2N-1}, \bar{\gamma}_0, \dots, \bar{\gamma}_{\delta-1} \}$ .

```

input :
   $\mathbf{\Lambda}_{\bar{\gamma},2N} \in \mathbb{R}_+^{2N \times 2N}$  is the nSNR matrix
   $N \in \mathbb{Z}_+$  is the number of subcarriers
   $\alpha \in \mathbb{R}_+$  is a threshold
begin
   $\delta = 0;$ 
   $C_{\bar{\gamma}}[0] = 1;$ 
  while  $C_{\bar{\gamma}}[\delta] \geq \alpha$  do
     $\delta = \delta + 1;$ 
     $C_{\bar{\gamma}}[\delta] = \frac{\text{Tr}(\mathbf{\Lambda}_{\bar{\gamma},2N} \mathbf{\Lambda}_{\bar{\gamma},2N}^2)}{\text{Tr}(\mathbf{\Lambda}_{\bar{\gamma},2N}^2)};$ 
  end
   $L_c = \delta + 1;$ 
end

```

Figure 18: The algorithm for choosing the  $L_c$  value when the SCRA technique is adaptive.

After defining the  $L_c$  value (constant or adaptive), the chunks can be matricially represented by

$$\begin{aligned} \mathbf{\Lambda}_{\bar{\gamma}_c} &\triangleq \mathbf{diag} \{ \bar{\gamma}_{c,0}, \bar{\gamma}_{c,1}, \dots, \bar{\gamma}_{c,N_c-1} \} \\ &= \mathbf{C}^T \mathbf{\Lambda}_{\bar{\gamma}} \mathbf{C}, \end{aligned} \quad (4.10)$$

where  $\bar{\gamma}_{c,i}$  is the nSNR representing the  $i^{\text{th}}$  chunk and  $\mathbf{C} \in \mathbb{R}^{N \times N_c}$  is a sparse dimensionality reduction matrix. If the chunk is constituted by adjacent nSNRs, then the element of  $\mathbf{C}$  at the  $k^{\text{th}}$  row and  $i^{\text{th}}$  column is defined by

$$C_{k,i} \triangleq \begin{cases} p_{k,i}, & iL_c \leq k < \min\{(i+1)L_c, N\} \\ 0, & \text{otherwise} \end{cases}, \quad (4.11)$$

in which  $p_{k,i}$  is a weight value given to the  $k^{\text{th}}$  subcarrier at the  $i^{\text{th}}$  chunk and  $\min\{a, b\}$  returns the minimum value between  $a$  and  $b$ .

An important parameter in the SCRA technique is  $p_{k,i}$ , because it defines the combination of the subcarriers belonging to the chunk in order to obtain the representative nSNR for each chunk. The choice of  $p_{k,i}$  can result in different performances of the SCRA technique. For instance,  $\bar{\gamma}_{c,i}$  can be rewritten as

$$\bar{\gamma}_{c,i} = \sum_{k=iL_c}^{\min\{(i+1)L_c, N\}-1} p_{k,i}^2 \bar{\gamma}_k. \quad (4.12)$$

Thus, if  $p_{k,i} = 1/\sqrt{L_c}$ , then  $\bar{\gamma}_{c,i}$  becomes the mean of the nSNRs belonging to  $i^{\text{th}}$  chunk. Other possible value of  $p_{k,i}$  is

$$p_{k,i} = \begin{cases} 1, & \bar{\gamma}_k = \Psi \{ \bar{\gamma}_{iL_c}, \dots, \bar{\gamma}_{\min\{(i+1)L_c, N\}-1} \} \\ 0, & \text{otherwise} \end{cases}, \quad (4.13)$$

where  $\Psi\{\cdot\}$  is a function that returns the minimum, median or maximum value. If  $p_{k,i}$  is given by (4.13) with  $\Psi\{\cdot\}$  being the function that selects the minimum value, then the SCRA technique is conservative. This means that the data rate is the lowest that can be obtained, but it satisfies the peak SER constraint. On the other hand, if the function  $\Psi\{\cdot\}$  selects the maximum value, then the SCRA technique yields the highest data rate; however, the peak SER constraint may not be satisfied.

In the SCRA technique, the numbers of bits allocated to all chunks according to their representative nSNRs, as well as the correspondent powers can be expressed by

$$[\mathbf{\Lambda}_{b_c}, \mathbf{\Lambda}_{P_c}] = f(\mathbf{\Lambda}_{\bar{\gamma}_c}, P_{t,c}, \Gamma), \quad (4.14)$$

where  $\mathbf{\Lambda}_{b_c} = \mathbf{diag}\{b_{c,0}, b_{c,1}, \dots, b_{c,N-1}\}$  and  $\mathbf{\Lambda}_{P_c} = \mathbf{diag}\{P_{c,0}, P_{c,1}, \dots, P_{c,N-1}\}$  are the resource allocation obtained with any resource allocation technique based on the rate-adaptive criterion;  $b_{c,i}$  and  $P_{c,i}$  are the number of bits and the portion of the total transmission power allocated to the  $i^{\text{th}}$  chunk, respectively;  $\text{Tr}(\mathbf{\Lambda}_{P_c}) \leq P_{t,c}$ ; and  $P_{t,c} = P_t N_c / N$  is the total transmission power shared among the chunks. Therefore, the order of the problem is  $N_c$  (usually  $N_c \ll N$ ), which is smaller than the order of the resource allocation expressed by (4.3). The majority of the computational complexity of the SCRA technique is in the bit loading algorithm, since the rest of the technique basically reorganizes the data without performing mathematical operations. The gain in terms of computational complexity reduction ratio that can be attained with the chunk-based resource allocation is defined as

$$\rho \triangleq 1 - \frac{1}{L_c}. \quad (4.15)$$

For the adaptive mode,  $L_c$  value is not constant, then  $\rho$  is evaluated considering the average chunk length for each value of  $\alpha$ . Since high  $L_c$  value indicates that more subcarriers are grouped together in a chunk, then the resource allocation technique can demand less computational complexity. Moreover, if  $L_c = 1$ , then the resource allocation technique must be executed for all subcarriers and, as a consequence, there is not a gain in terms of computational complexity reduction ratio ( $\rho = 0$ ).

The number of bits transmitted through each subchannel and its corresponding allocation of transmission power are given, respectively, by the following diagonal matrices:

$$\mathbf{\Lambda}_b \triangleq \mathcal{Z}(\bar{\mathbf{C}} \mathbf{\Lambda}_{b_c} \bar{\mathbf{C}}^T) \quad (4.16)$$

and

$$\mathbf{\Lambda}_P \triangleq \mathcal{Z}(\bar{\mathbf{C}} \mathbf{\Lambda}_{P_c} \bar{\mathbf{C}}^T), \quad (4.17)$$

in which  $\mathcal{Z}(\cdot)$  is a function that sets off-diagonal elements to zero and  $\bar{\mathbf{C}} \in \mathbb{B}^{N \times N_c}$ ,  $\mathbb{B} = \{0, 1\}$ , has its elements expressed by

$$\bar{\mathbf{C}}_{k,i} = \begin{cases} 1, & iL_c \leq k < \min\{(i+1)L_c, N\} \\ 0, & \text{otherwise} \end{cases}. \quad (4.18)$$

In other words, (4.16) and (4.17) mean that the result of the bit loading algorithm obtained for the  $i^{th}$  chunk is applied to all subcarriers belonging to the set. Finally, the data rate of the OFDM-based PLC system is expressed by

$$R_c = \frac{1}{T_{OFDM}} \text{Tr}(\mathbf{\Lambda}_b) \quad (4.19)$$

and the data rate loss ratio is defined as

$$\eta \triangleq 1 - \frac{R_c}{R^o}, \quad (4.20)$$

where  $R^o$  is the optimal data rate because  $N_c = N$  (see (4.4)). Note that (4.20) uses  $R^o$  to quantify the data rate loss due to the use of the chunk-based resource allocation technique. Depending on  $p_{k,i}$ , it is possible to obtain  $R_c > R^o$  and, as a consequence,  $\eta < 0$ , but the SER is compromised, as is shown in Section 4.3. Note that  $\eta$  compares the SCRA technique with the optimal technique, which is proposed in [22].

Fig. 19 shows the algorithm devised for implementing the SCRA technique. If the SCRA technique is adaptive, then first execute the algorithm in Fig. 18, in order to specify the  $L_c$  value and, next, feed the algorithm of the SCRA technique with this information.

### 4.3 PERFORMANCE ANALYSES

The purpose of this section is to discuss performance analyses of the SCRA technique in different scenarios. All analyses are based on measured in-home PLC channels and additive noises. This data set is the same used in Section 3.3.1. The numerical analyses address the frequency bands of 1.7-30 MHz, 1.7-50 MHz, and 1.7-100 MHz, which are represented by  $W_{30}$ ,  $W_{50}$  and  $W_{100}$ , respectively. Furthermore, all analyses in this chapter use a greedy technique based on [68], as described in [39], with  $\Gamma(\text{dB}) = 9.3$  dB (i.e., the peak SER constraint is  $10^{-6}$ ).

This section is organized into three subsections. Subsection 4.3.1 analyzes the performance of the SCRA technique for different ways of choosing the representative nSNR for a chunk (i.e., different approach to chose  $p_{k,i}$  values). Subsection 4.3.2 addresses a comparison result of SCRA technique when adaptive and constant  $L_c$  is adopted. Finally, Subsection 4.3.3 focuses on a comparison between the SCRA technique fed by the nSNR coherence bandwidth and by the coherence bandwidth which is important result for validating the usefulness of  $B_{c,\bar{\gamma}}$ . Finally, Subsection 4.3.3 focuses on a comparison between the SCRA technique and the technique proposed in [56,57].

#### 4.3.1 Analysis of criteria for representing a chunk

The choice of the representative nSNR for a chunk, which depends on  $p_{k,i}$ , changes the SCRA technique performance. In this context, Fig. 20 shows the CCDF of peak and

```

input :
 $\mathbf{\Lambda}_{\bar{\gamma}} \in \mathbb{R}_+^{N \times N}$  is the nSNR matrix
 $N \in \mathbb{Z}_+$  is the number of subcarriers
 $L_c \in \mathbb{Z}_+$  is the length of the first  $N_c - 1$  chunks
 $P_t \in \mathbb{R}_+$  is the total transmission power
 $\Gamma \in \mathbb{R}_+$  is the gap
begin
  - Obtain  $\mathbf{\Lambda}_{\bar{\gamma}_c}$ 
   $N_c = \lceil N/L_c \rceil$ ;
  for  $i = 0$  to  $N_c - 1$  do
    if  $i = N_c - 1$  then
       $\mathbf{\Lambda}_{\bar{\gamma}_c}[i, i] = \Psi\{\bar{\gamma}_{iL_c}, \dots, \bar{\gamma}_{N-1}\}$ ;
    else
       $\mathbf{\Lambda}_{\bar{\gamma}_c}[i, i] = \Psi\{\bar{\gamma}_{iL_c}, \dots, \bar{\gamma}_{(i+1)L_c-1}\}$ ;
    end
  end
  - Run the resource allocation algorithm
   $P_{t,c} = P_t N_c / N$ ;
  Evaluate (4.14);
  - Extend the results to all subcarriers
   $i = 0$ ;
  for  $k = 0$  to  $N - 1$  do
    if  $k \geq (i + 1)L_c$  then
       $i = i + 1$ ;
    end
     $\mathbf{\Lambda}_b[k, k] = \mathbf{\Lambda}_{b_c}[i, i]$ ;
     $\mathbf{\Lambda}_P[k, k] = \mathbf{\Lambda}_{P_c}[i, i]$ ;
  end
end

```

Figure 19: The algorithm for the implementation of the SCRA technique.

average SER, calculated by (4.5) and (4.6), respectively, for the aforementioned ways of choosing the representative nSNR for a chunk, see previous section. This plot covers  $W_{100}$  and  $L_c = 8$  (except for the optimal case, in which  $L_c = 1$ ) to show the SER behavior when the SCRA technique applies. Remember that the optimal case does not mean the smallest SER, in this case all subcarriers are considered in the resource allocation and, thereby, it is optimal in the sense of data rate. Note that the peak SER constraint of  $10^{-6}$  is only guaranteed for 100% of the data set for the optimal case, as it is expected if the representative nSNR is the minimum value in the chunk. Moreover, the peak SER yielded by the proposed technique, when the minimum value applies, is slightly better than the optimal resource allocation, showing that the SCRA technique has a conservative behavior. For all other choices (mean, median and maximum values), the SCRA technique violates the peak SER constraint. The results are similar for average SER, but in this case the conservative behavior of the SCRA technique is more evident if the minimum value applies. This occurs because the average SER performance of the SCRA technique is higher than

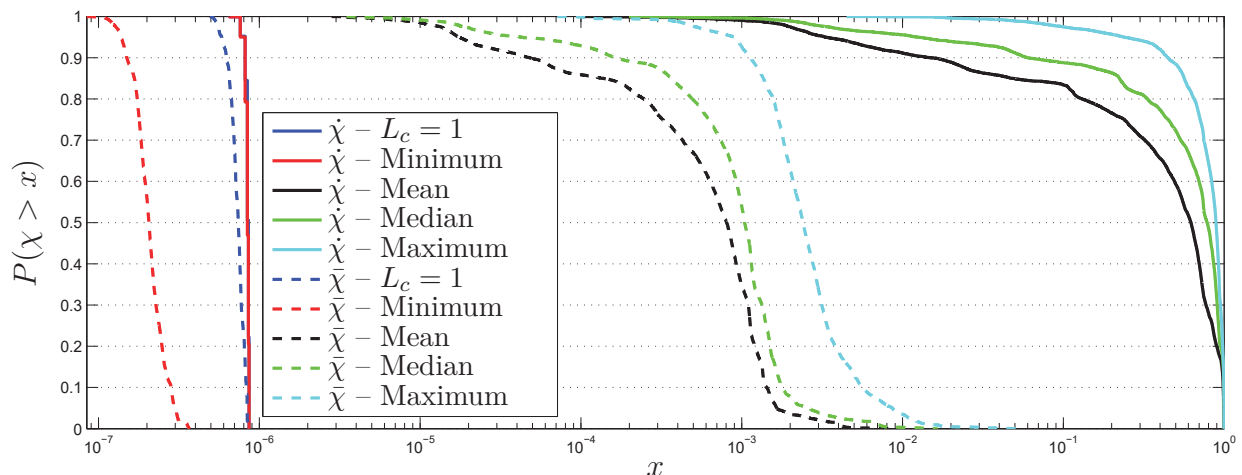


Figure 20: The CCDFs of the peak SER ( $\dot{\chi}$ ) and the average SER ( $\bar{\chi}$ ) for different ways of choosing  $p_{i,k}$  with  $L_c = 8$  and  $W_{50}$ .

the average SER performance of the optimal resource allocation (in the sense of data rate).

Fig. 21 shows the performance of the SCRA technique in terms of data rate loss ratio for the aforementioned ways of choosing the representative nSNR associated with a chunk. In this figure,  $P(\eta > x)$  indicates the probability of the data rate loss ratio being higher than  $x$ . The case  $L_c = 1$  is the reference, because it outputs the optimal data rate due to the use of the resource allocation technique described in [22]. Note that the choice of minimum value yields the highest data rate loss, but guarantees the SER constraint (see Fig. 20).

When the representative nSNR associated with a chunk is the maximum value, a data rate gain occurs in 100% of the data set, but the SER constraint is strongly violated in all data set. Moreover, if the median value is adopted, then a data rate loss occurs in 19.7% of the data set. On the other hand, if the mean value is used, then 100% of data set show a small data rate loss. In spite of the small variation of data rate, it is important to emphasize that median and mean values do not guarantee the peak SER constraint. In other words, the minimum value is the best choice among the chosen ones, disregarding the fact that it is conservative and introduces the highest data rate losses.

#### 4.3.2 Analysis due to the $L_c$ value

The SCRA technique shows difference performance for each value of  $L_c$ . In this regard, this subsection presents a comparison in terms of the data rate loss ratio and the computational complexity reduction ratio. All analyses consider the minimal value for the representative nSNR for a chunk, since it guarantees the peak SER constraint.

Fig. 22 shows two different information for  $W_{30}$ ,  $W_{50}$ , and  $W_{100}$ : (i) the CCDF of data rate loss ratio ( $\eta$ ) for the SCRA technique considering  $L_c \in \{1, 2, 4, 8, 16\}$ ; and (ii)

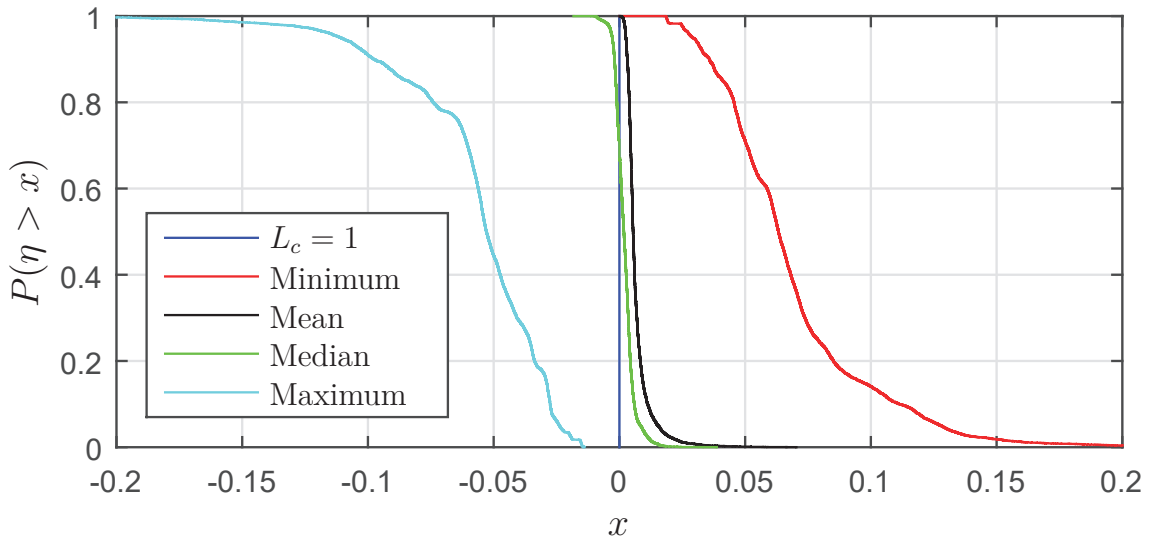


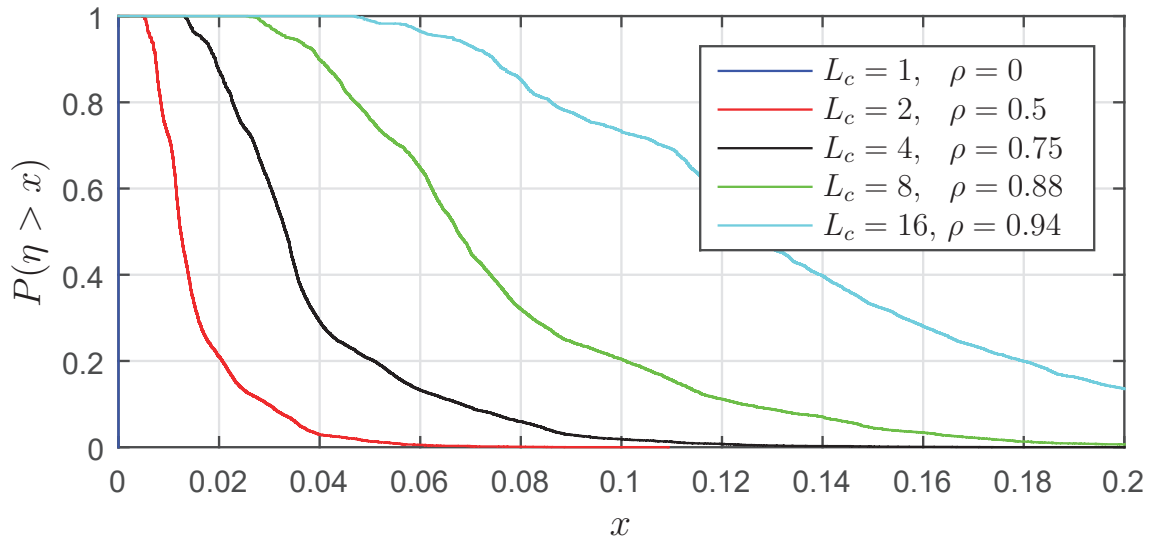
Figure 21: The CCDF of data rate loss ratio ( $\eta$ ) for different ways of choosing  $p_{i,k}$  with  $L_c = 8$  and  $W_{50}$ .

Table 8: An example of the trade off between data rate loss ratio and computational complexity reduction ratio in Fig. 22a for  $W_{30}$ .

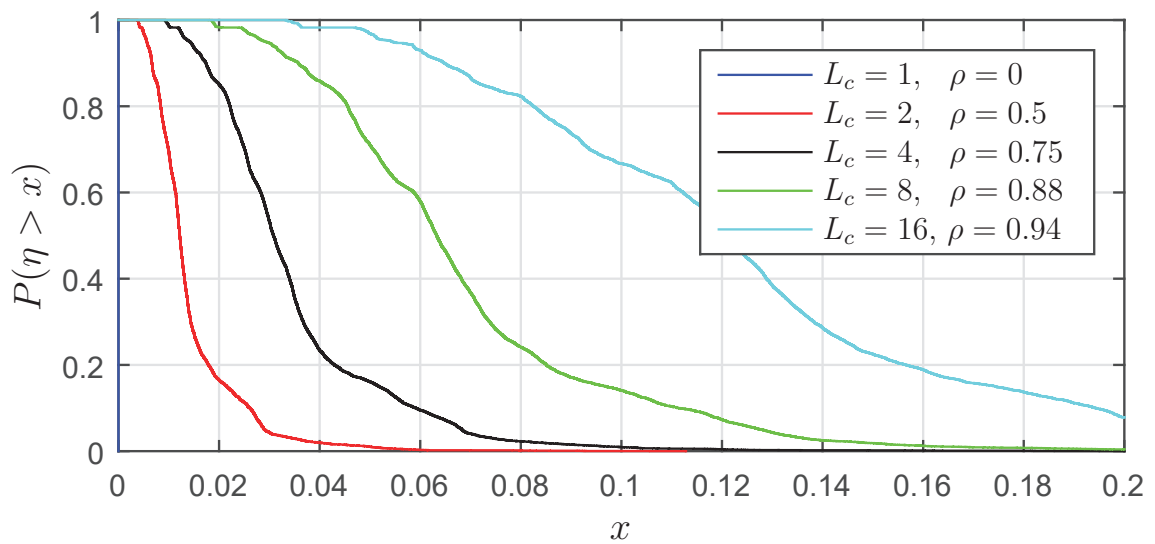
$L_c$	1	2	4	8	16
$P(\eta > 0.05)$	0	0.01	0.20	0.76	0.98
$\rho$	0	0.5	0.75	0.88	0.94

the computational complexity reduction ratio ( $\rho$ ) for the same chunk lengths. Note that if  $L_c = 1$ , then the SCRA technique yields the optimal data rate. In all frequency bands, the  $L_c$  value drives the trade off between  $\eta$  and  $\rho$ . Also, the higher  $L_c$  is, the higher the data rate loss ratio and the computational complexity reduction ratio are. Table 8 illustrates this trade off for  $W_{30}$ . As an example, if  $L_c = 2$ , then in 1% of the data set occurs data rate loss higher than 5% and the computational complexity reduces in 50%, since the number of chunks is half of the number of subcarriers. On the other hand, if  $L_c = 8$ , then in 76% of the data set occurs data rate loss ratio higher than 5%, but the computational complexity reduces in 88%. Overall, the plots of Fig. 22 show that the SCRA technique yields similar results for all frequency bands when the  $L_c$  value is constant.

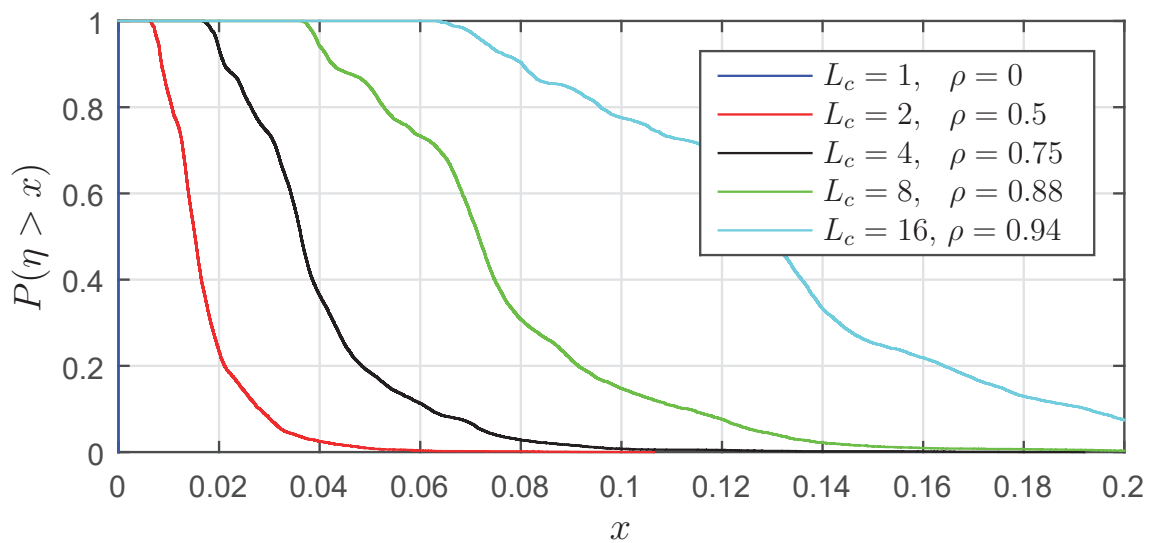
Fig. 23 shows the performance of the SCRA technique in terms of  $\eta$  and  $\rho$  when the chunk length is adaptive ( $L_c = B_{c,\bar{\gamma}}/B_s$ ). As  $B_{c,\bar{\gamma}}$  varies with  $\alpha$ , the results are in terms of  $\alpha \in \{1, 0.98, 0.95, 0.90, 0.85\}$ . Note that if  $\alpha = 1$ , then the SCRA technique returns the optimal resource allocation, since  $L_c = 1$ . Figs. 23a-23c show the obtained results for  $W_{30}$ ,  $W_{50}$ , and  $W_{100}$ , respectively. Also, note that  $\alpha$  drives the trade off between the data rate loss ratio and the computational complexity reduction ratio (i.e., the higher is  $\alpha$ , the lower are the values of  $\eta$  and  $\rho$ ). For instance, if  $W_{30}$  and  $\alpha = 0.9$ , then  $P(\eta > 0.05) = 0.78$  and  $\rho = 0.92$ . On the other hand, if  $W_{30}$  and  $\alpha = 0.95$ , then  $P(\eta > 0.05) = 0.42$  and  $\rho = 0.87$ . A careful observation of Figs. 23a-23c reveals that the SCRA technique offers more gains



(a)



(b)



(c)

Figure 22: The CCDFs of the data rate loss ratio ( $\eta$ ) when the  $L_c$  value is constant. (a)  $W_{30}$ , (b)  $W_{50}$ , and (c)  $W_{100}$ .

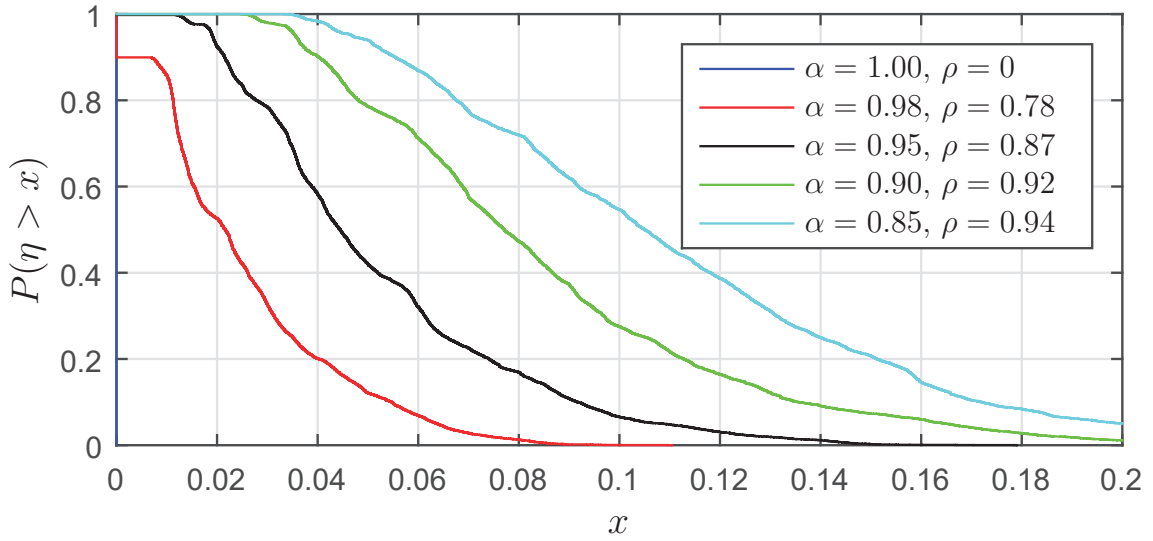
when the frequency bands increase and the  $L_c$  value is adaptive. As an example, if  $\alpha = 0.9$ , then  $P(\eta > 0.05) = 0.78$ ,  $P(\eta > 0.05) = 0.84$  and  $P(\eta > 0.05) = 0.87$  for  $W_{30}$ ,  $W_{50}$ , and  $W_{100}$ , respectively.

Finally, Figs. 24a-24c show the attained result with the SCRA technique when the  $L_c$  value is constant or adaptive. Values of  $\alpha$  were chosen in order to guarantee that the computational complexity reduction ratio is similar for both constant and adaptive modes. Fig. 24a-24c show the results for  $W_{30}$ ,  $W_{50}$ , and  $W_{100}$ , respectively. Note that the adaptive mode of the SCRA technique may offer considerable improvement in comparison with the constant mode, mainly if  $L_c$  increases.

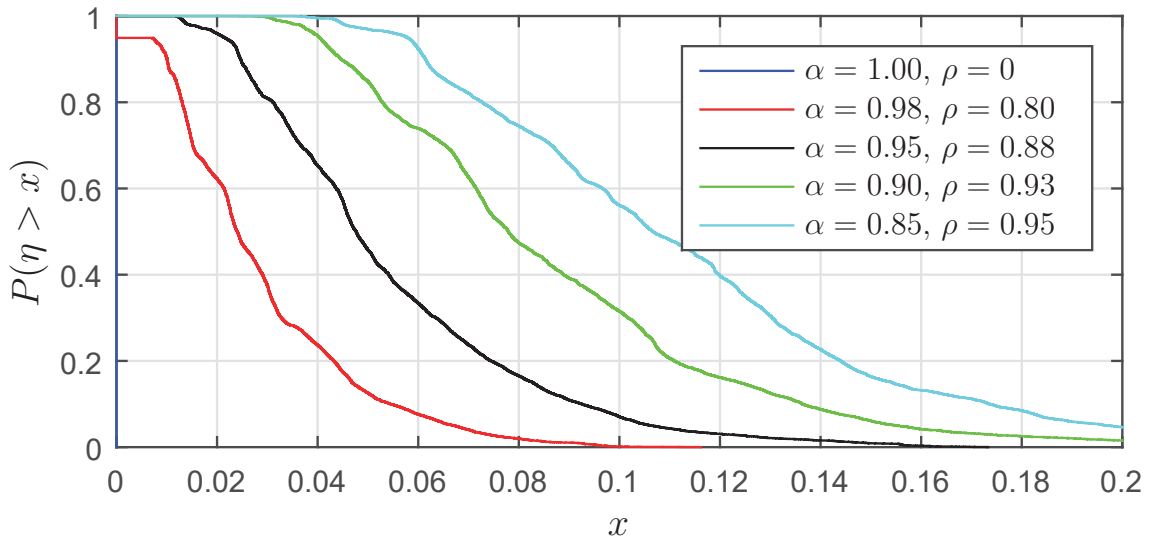
#### 4.3.3 Comparison between the nSNR coherence bandwidth and the coherence bandwidth

The SCRA technique working in the adaptive mode uses the nSNR coherence bandwidth ( $B_{c,\bar{\gamma}}$ ) for determining the number of adjacent subcarriers to constitute a chunk. It follows Chapter 3, which claims that the nSNR coherence bandwidth is the correct parameter to be used in resource allocation techniques for PLC systems and the use of the coherence bandwidth can result in mistakes. In order to reinforce the correctness of this claim, this section discusses the SCRA technique performance when the nSNR coherence bandwidth is used in (4.9) (as proposed in Chapter 3) and when it uses the coherence bandwidth.

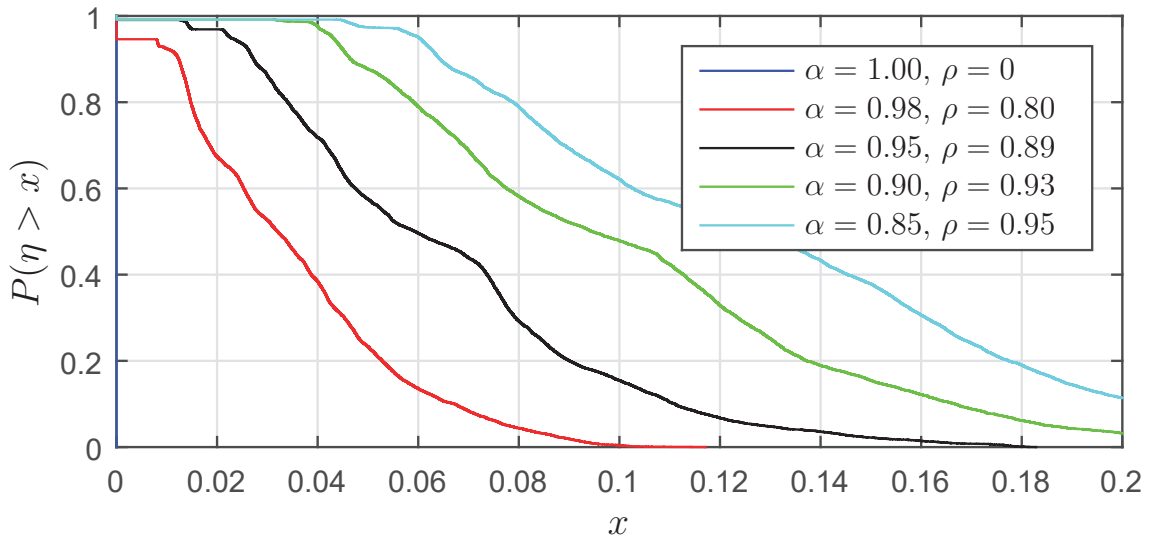
Fig. 25 shows the attained performance of the SCRA technique based on  $B_{c,\bar{\gamma}}$  for  $\alpha \in \{0.98, 0.90, 0.5\}$ . In addition, this figure shows the SCRA technique performance for the same  $\alpha$ , when  $B_{c,H}$  replaces  $B_{c,\bar{\gamma}}$  in (4.9). Figs. 25a-25c depict the results for  $W_{30}$ ,  $W_{50}$ , and  $W_{100}$ , respectively. Note that if  $\alpha$  is high ( $\alpha \rightarrow 1$ ), then the performance is similar for both coherence bandwidths in all frequency bands. This occurs due to the fact that a high value of  $\alpha$  produces a small coherence bandwidth and, consequently, a small  $L_c$  value for both coherence bandwidths. Thus, the data rate loss ratio is small for both of them and there is no significant difference between the use of them. On the other hand, for a small  $\alpha$  ( $\alpha \rightarrow 0$ ), the data rate loss ratio is high and the use of the nSNR coherence bandwidth offers a better compromise between data rate loss ratio and computational complexity reduction ratio. Table 9 illustrate this kind of behavior for  $W_{100}$ . Note that  $P(\eta > 0.15) = 0$  for  $\alpha = 0.5$  when the nSNR coherence bandwidth is considered, which is very close to  $P(\eta > 0.15) = 0.002$  for the coherence bandwidth. If  $\alpha = 0.98$ , then  $P(\eta > 0.15) = 0.948$  for the nSNR coherence bandwidth, which is 0.037 smaller than  $P(\eta > 0.15) = 0.985$  when the coherence bandwidth applies. Moreover, the same  $\alpha$  generates a similar computational complexity loss ratio when both nSNR coherence bandwidth and coherence bandwidth apply, see last line of Table 9.



(a)

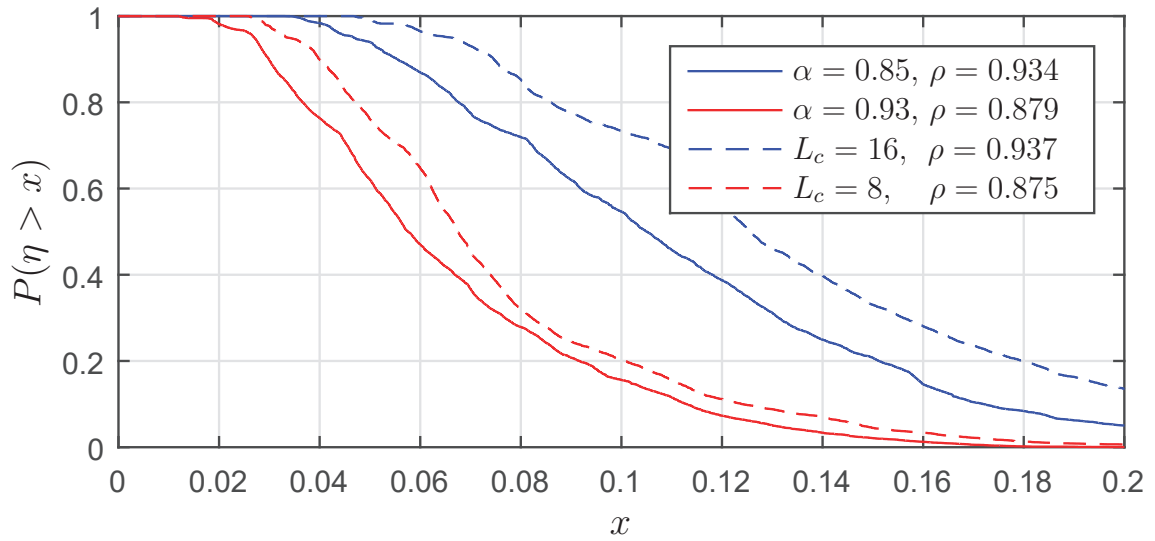


(b)

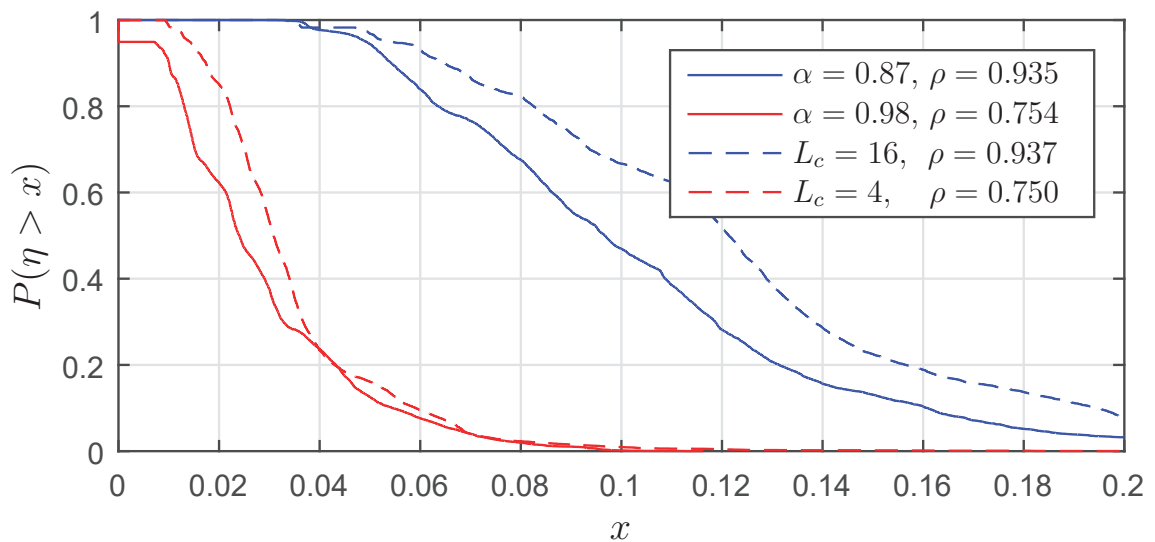


(c)

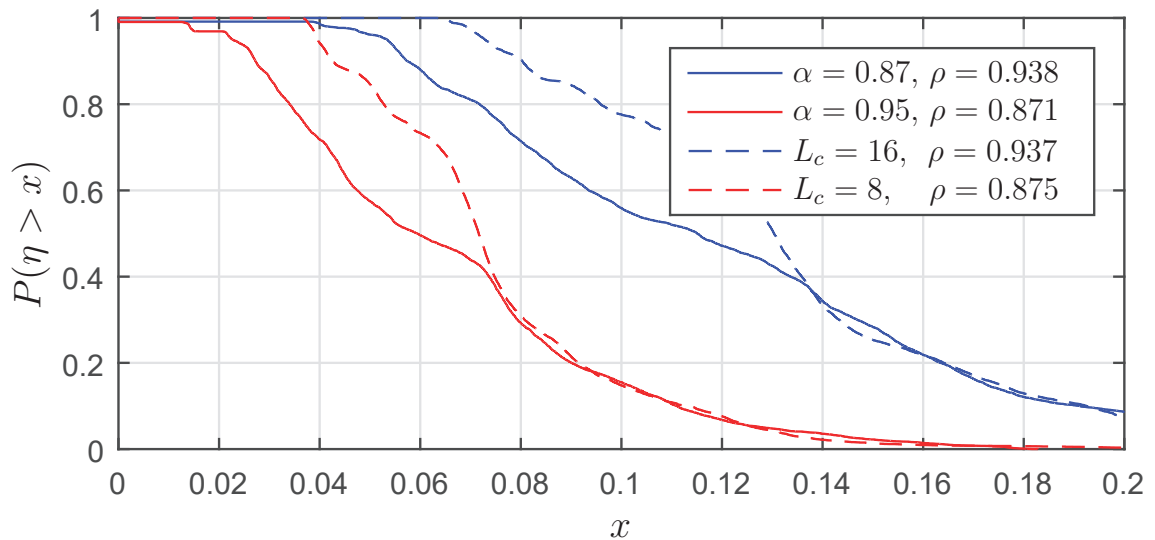
Figure 23: The CCDFs of the data rate loss ratio ( $\eta$ ) when the  $L_c$  value is adaptive. (a)  $W_{30}$ , (b)  $W_{50}$ , and (c)  $W_{100}$ .



(a)

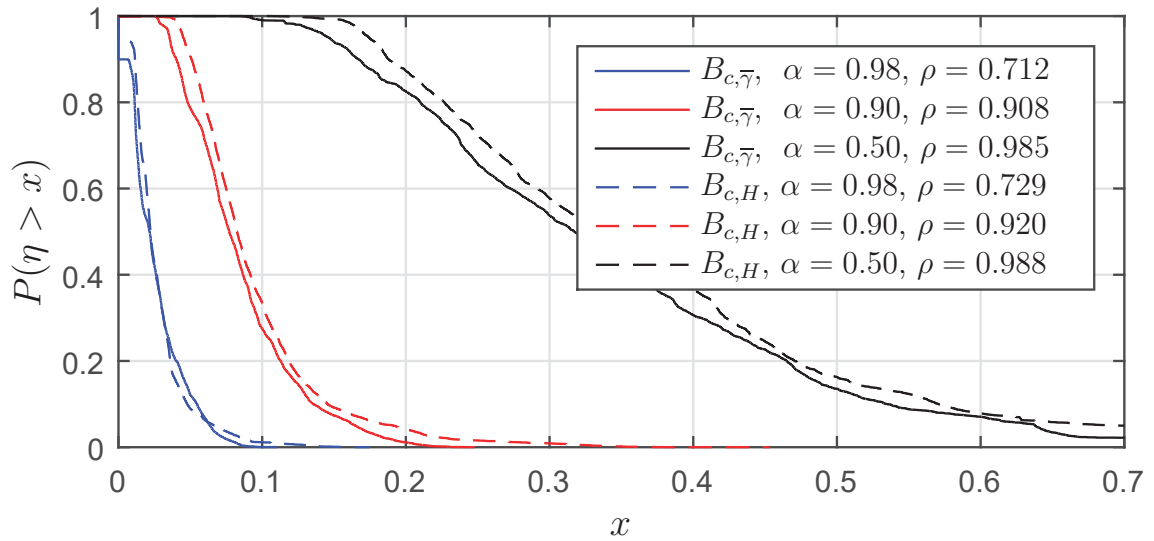


(b)

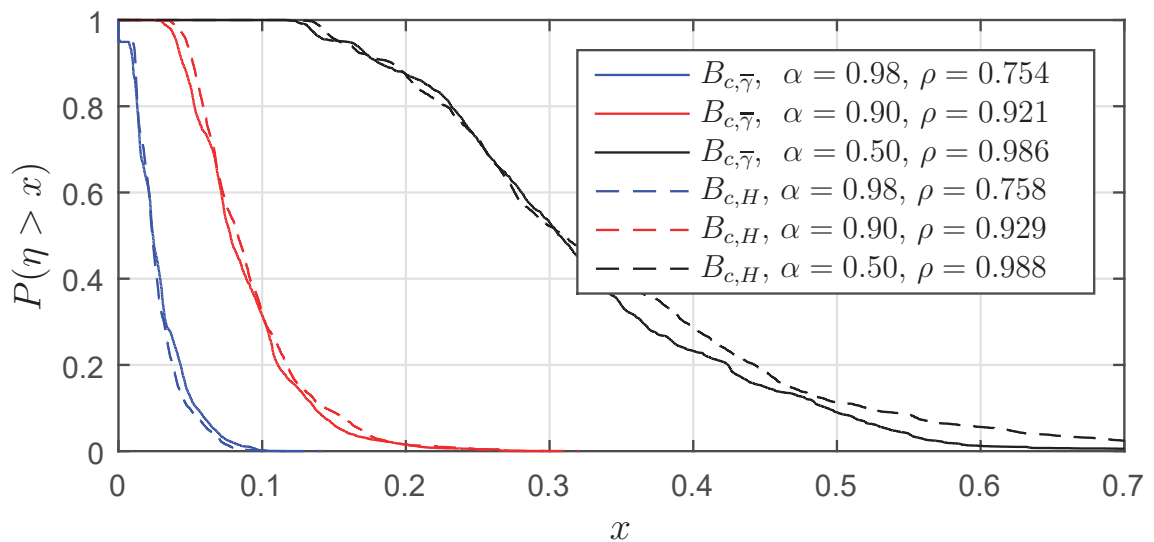


(c)

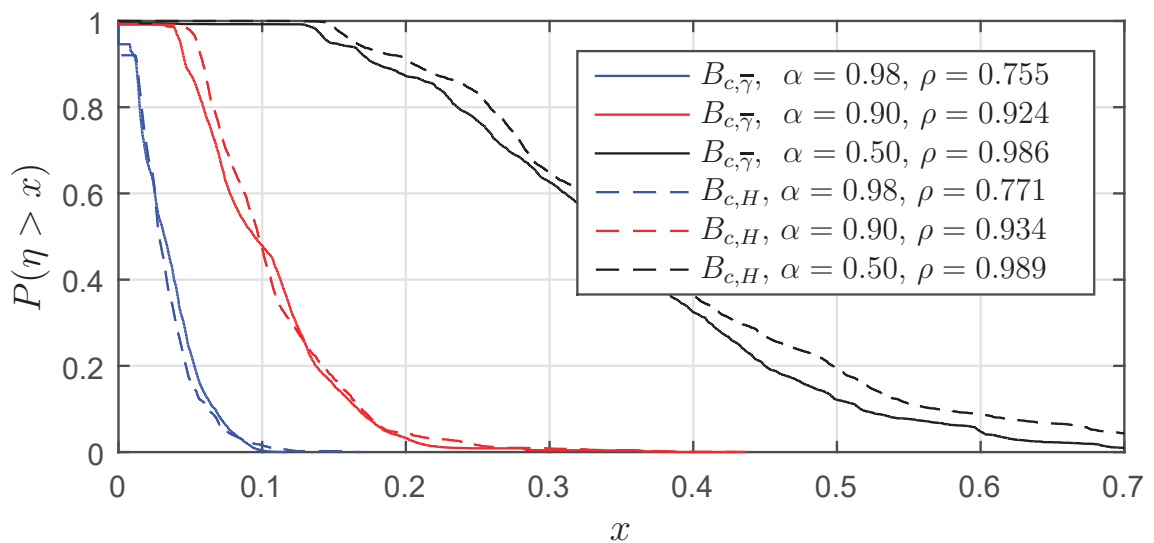
Figure 24: The CCDFs of the data rate loss ratio ( $\eta$ ) when the  $L_c$  value is constant and adaptive. (a)  $W_{30}$ , (b)  $W_{50}$ , and (c)  $W_{100}$ .



(a)



(b)



(c)

Figure 25: The CCDFs of the data rate loss ratio ( $\eta$ ) when the  $L_c$  value is chosen based on the nSNR coherence bandwidth and the coherence bandwidth. (a)  $W_{30}$ , (b)  $W_{50}$ , and (c)  $W_{100}$ .

Table 9: Comparison between the SCRA technique feeds by  $B_{c,\bar{\gamma}}$  and  $B_{c,H}$  for  $W_{100}$ .

	$B_{c,\bar{\gamma}}$			$B_{c,H}$		
$\alpha$	0.98	0.90	0.50	0.98	0.90	0.50
$P(\eta > 0.15)$	0	0.154	0.948	0.002	0.170	0.985
$\rho$	0.755	0.924	0.986	0.771	0.934	0.989

#### 4.4 SUMMARY

The main conclusions of this chapter are summarized as follows:

- The introduction of the SCRA technique, which groups adjacent subcarriers in order to reduce the computational complexity of resource allocation techniques for OFDM-based PLC systems.
- Only the minimal nSNR to represent a chunk, among those analyzed in this work, guarantees the SER constraint. Thereby, it is the best way of choosing the nSNR representative of a chunk, despite obtaining the highest data rate loss ratio.
- If the chunk bandwidth is constant, then the chunk length drives a trade off between the computational complexity reduction ratio and the data rate loss ratio. On the other hand, if it is adaptive, then this trade off is driven by the threshold of the nSNR coherence bandwidth.
- A comparison between the SCRA technique working with constant and adaptive chunk length/bandwidth with a similar computational complexity reduction ratios shows that the adaptive mode yields lower data rate loss ratio than the constant one.
- If the nSNR coherence bandwidth is used, in the adaptive mode, to specify the chunk length/bandwidth, then the SCRA technique results in less data rate loss ratio than the use of the coherence bandwidth.

## 5 AN ORTHOGONAL TIME-FREQUENCY DIVISION MULTIPLEXING SCHEME

According to Chapters 2 and 4, the exploitation of the existing relationship among microslots and among subchannels can individually yield low-cost resource allocation techniques with reduced data rate loss in OFDM-based PLC systems, mainly because the number of subcarriers and/or the number of users are large and the PLC channel is LPTV. Different from the optimal resource allocation technique introduced in [22], TCRA and SCRA techniques can trade data rate loss with computational complexity reduction and their attained results showed that if the OFDM scheme is adopted, then each of them can be separately deployed to considerably reduce the computational complexity associated with resource allocation techniques.

Regarding the SCRA technique, Chapter 4 showed that the computational complexity savings is relevant with significant data rate loss because the choice of the representative nSNR for the chunk is in favor of the minimum value, disregarding the fact that the chunk bandwidth is lower than the nSNR bandwidth. The minimum value of nSNR is the most appropriate choice because it assures that the target symbol error probability is not violated. As a consequence, the SCRA technique may yield substantial data rate loss in order to considerably reduce the computational complexity of resource allocation techniques applied to OFDM-based PLC systems. In this context, the introduction of strategies, approaches or techniques that could somehow curtail such data rate loss can notably benefit the use of the SCRA with a resource allocation technique.

Given the aforementioned context, this chapter introduces a new multicarrier scheme that is capable of maximizing the usefulness of the SCRA technique for computational complexity reduction purpose in a multicarrier-based PLC systems. The new multicarrier scheme is called orthogonal time-frequency division multiplexing (OTFDM). The core of this new multicarrier scheme is the discrete orthogonal Stockwell transform (DOST) [69], which is capable of offering tiles in the time-frequency domain with different geometries and, as a consequence, provides a novel perspective for grouping subcarriers for computational complexity reduction as suggested by the SCRA technique. Moreover, the OTFDM scheme can be applied to both baseband and passband data communications. The main contributions of this chapter are summarized as follows:

- The introduction of an OTFDM scheme in the baseband, which is required for PLC systems, and its passband variation. This scheme organizes the information to be transmitted in tiles with geometry, which is different from the tiles used for an OFDM scheme. Therefore, it offers flexibility to achieve high performance in terms of data rate loss ratio, compared with the OFDM-based schemes, if the SCRA technique applies.

- Analyses in terms of SER of the OTFDM scheme for PLC systems, considering additive noise with different components, such as the background noise, impulsive noise and NBI.
- A comparison analysis between OFDM and OTFDM schemes in terms of SER and data rate loss ratio, when both of them are used together with the SCRA technique for reducing the computational complexity of resource allocation techniques.

## 5.1 PROBLEM FORMULATION

Let a PLC system based on OFDM scheme be working within a frequency band from 0 to  $B$  Hertz. Assume sampling frequency  $F_s = 2B$ ; OFDM symbol interval  $T_{\text{sym}} = (2N + L_{cp})/F_s$ , where  $N$  is the number of subcarriers; and subchannel bandwidth  $B_s = B/N$ . Also, let  $\{h[n]\}_{n=0}^{L_h-1}$  be the CIR of an LTI PLC channel with length  $L_h$  and time and frequency domain vectorial representation given, respectively, by  $\mathbf{h} = [h[0], h[1], \dots, h[L_h-1]]^T \in \mathbb{R}^{L_h \times 1}$  and  $\mathbf{H} = [H_0, H_1, \dots, H_{2N-1}]^T = \mathbf{W}_{2N} [\mathbf{h}^T \mathbf{0}_{2N-L_h}^T]^T$ , where  $\mathbf{W}_{2N} \in \mathbb{C}^{2N \times 2N}$  is the  $2N$ -size DFT matrix,  $\mathbf{0}_{2N-L_h}$  is the  $(2N - L_h)$ -length column vector composed of zeros and  $(\cdot)^T$  denotes the transposition operator. Let  $\mathbf{H}$  have a matrix representation given by  $\mathbf{\Lambda}_H = \mathbf{diag}\{H_0, H_1, \dots, H_{2N-1}\}$ , where  $\mathbf{diag}\{\cdot\}$  denotes a diagonal matrix. Now assume that the PLC signal is impaired by an additive noise, which can be expressed by [10, 28, 29, 70]

$$v[n] = v_{bkg}r[n] + v_{ps}[n] + v_{imp}[n] + v_{nbi}[n], \quad (5.1)$$

where  $v_{bkg}r[n] \sim \mathcal{N}(0, \sigma^2)$  denotes the background noise modeled as AWGN;  $v_{ps}[n] \sim \mathcal{N}(0, K\sigma^2)$  denotes a periodic component with arrival interval  $t_{arr,ps} = (1/2f_0)$  ( $f_0$  is the mains frequency of the power system and  $K$  parameterizes different levels of severity of the impulsive noise components) and time duration  $T_{w,ps}$ ;  $v_{imp}[n] \sim \mathcal{N}(0, K\sigma^2)$  represents an impulsive component with inter-arrival time  $t_{arr,imp}$  modeled as an exponential random variable with mean  $\bar{t}_{arr,imp}$  and duration  $T_{w,imp}$ ; and  $v_{nbi}[n]$  denotes an NBI component. The NBI component is modeled by [29]

$$v_{nbi}[n] = \sum_{o=-(\Upsilon-1)/2}^{(\Upsilon-1)/2} A_o \cos(2\pi k_o n/2N), \quad (5.2)$$

in which  $\Upsilon$  is the number of single-tone signals that constitute the NBI component,  $A_o = \frac{-2A_c}{\Upsilon+1}|o| + A_c$  is the amplitude of the  $o^{th}$  single-tone signal,  $A_c$  is the amplitude of the central single-tone signal,  $k_o = k_c + o$ , and  $k_c \in \mathbb{Z}$ . Note that the frequency of the  $o^{th}$  single-tone signal is expressed by  $f_o = k_o F_s/2N$  and the power of the central single-tone signal is  $P_{nbi,c} = A_c^2/2$ . Moreover, let  $\mathbf{V}_i = \frac{1}{2N} \mathbf{W}_{2N} \mathbf{v}_i \in \mathbb{C}^{2N \times 1}$  be the vectorial representation in the frequency domain of the PLC additive noise, where  $\mathbf{v}_i$  is the  $i^{th}$   $2N$ -length window of  $\{v[n]\}$ ;  $\mathbb{E}\{\mathbf{V}_i\} = 0$ , in which  $\mathbb{E}\{\cdot\}$  denotes the expectation operator.

Now, let  $\mathbf{X}_i = [X_{i,0}, X_{i,1}, \dots, X_{i,N-1}]^T \in \mathbb{C}^{N \times 1}$  be the vectorial representation of the  $i^{\text{th}}$  OFDM symbol in the frequency domain. The vectorial representation of the  $i^{\text{th}}$  OFDM symbol in the time domain is expressed by  $\mathbf{x}_i = (1/2N)\mathbf{W}_{2N}^\dagger \mathbf{X}_{\text{hs},i}$ , where  $\dagger$  denotes the hermitian operator and the  $k^{\text{th}}$  element of the vector  $\mathbf{X}_{\text{hs},i}$  is obtained with

$$X_{\text{hs},i,k} = \begin{cases} \Re\{X_{i,N-1}\}, & k = 0 \\ X_{i,k-1}, & k = 1, \dots, N-1 \\ \Im\{X_{i,N-1}\}, & k = N \\ X_{i,2N-1-k}^*, & k = N+1, \dots, 2N-1 \end{cases}, \quad (5.3)$$

in which  $\Re\{\cdot\}$  and  $\Im\{\cdot\}$  denote the real and imaginary components of a complex number, respectively, and  $*$  denotes the complex conjugation operation, since the data communication is performed in the baseband. The vectorial representation of the  $i^{\text{th}}$  OFDM symbol after the cyclic prefix insertion is given by

$$\mathbf{x}_{cp,i} = \begin{bmatrix} \mathbf{0} & \mathbf{I}_{L_{cp}} \\ & \mathbf{I}_{2N} \end{bmatrix} \mathbf{x}_i, \quad (5.4)$$

in which  $L_{cp} \geq L_h - 1$  is the cyclic prefix length,  $\mathbf{0} \in \mathbb{R}^{L_{cp} \times 2N - L_{cp}}$  is a matrix constituted by zeros and  $\mathbf{I}_a \in \mathbb{R}^{a \times a}$  is a  $a$ -size identify matrix.

Following this framework, the transmitted signal, in the time domain, is the infinite succession of OFDM symbols extended with their cyclic prefix. Its expression is given by

$$x[n] = \sum_{i=-\infty}^{\infty} \sum_{p=0}^{2N+L_{cp}-1} x_{cp,i,p} \delta[n - i2N - j], \quad (5.5)$$

where  $x[n] \in \mathbb{R}$ ,  $x_{cp,i,p}$  is the  $p^{\text{th}}$  element of  $\mathbf{x}_{cp,i}$  and  $\{\delta[n]\}$  is the impulsive sequence. Then, the channel output can be expressed by

$$\begin{aligned} r[n] &= \tilde{r}[n] + v[n] \\ &= h[n] \star x[n] + v[n]. \end{aligned} \quad (5.6)$$

where  $\star$  denotes the convolution operator,  $\tilde{r}[n]$  is the PLC channel output free of noise and  $v[n]$  is the additive noise at the PLC channel output. By assuming perfect synchronism and removing the cyclic prefix, the vectorial representation of the  $i^{\text{th}}$  received OFDM symbol can be expressed by  $\mathbf{y}_i \in \mathbb{R}^{2N \times 1}$ . An estimate of  $\mathbf{X}_{\text{hs},i}$  can be obtained by applying a frequency-domain equalization (FDE) based on zero-forcing (ZF) or minimum mean square error (MMSE) criteria [71, 72]. By applying FDE based on ZF criterion, one obtains

$$\begin{aligned} \hat{\mathbf{X}}_{\text{hs},i} &= \mathbf{\Lambda}_H^{-1} \mathbf{Y}_i \\ &= \mathbf{\Lambda}_H^{-1} (\mathbf{\Lambda}_H \mathbf{X}_{\text{hs},i} + \mathbf{V}_i) \\ &= \mathbf{X}_{\text{hs},i} + \mathbf{\Lambda}_H^{-1} \mathbf{V}_i, \end{aligned} \quad (5.7)$$

in which  $\mathbf{Y}_i = (1/2N)\mathbf{W}_{2N}\mathbf{y}_i$ . Finally, by using the inverse of the mapping performed by (5.3), then  $\hat{\mathbf{X}}_i \in \mathbb{C}^{N \times 1}$ , which is an estimate of  $\mathbf{X}_i$ , is obtained. Based on such formulation, the normalized SNR in each subchannel can be expressed as

$$\begin{aligned} \mathbf{\Lambda}_{\bar{\gamma}, 2N} &= \mathbf{diag}\{\bar{\gamma}_0, \bar{\gamma}_1, \dots, \bar{\gamma}_{2N-1}\} \\ &= \frac{\mathbf{\Lambda}_{|H|^2} \mathbf{\Lambda}_{S_v}^{-1}}{B_s}, \end{aligned} \quad (5.8)$$

where  $\bar{\gamma}_k$  is the nSNR at the  $k^{th}$  subchannel,  $\mathbf{\Lambda}_{|H|^2} = \mathbf{\Lambda}_H \mathbf{\Lambda}_H^\dagger$  and  $\mathbf{\Lambda}_{S_v} = \mathbb{E}\{\mathbf{V}_i \mathbf{V}_i^\dagger\}/2B = \mathbf{diag}\{S_{v,0}, S_{v,1}, \dots, S_{v,2N-1}\}$ , in which  $S_{v,k}$  is the PSD noise associated with  $k^{th}$  subchannel. Note that the data transmission is performed in the baseband; therefore, the total transmission power and the bits are allocated only to  $N$  subchannel and not to  $2N$  ones. Therefore, the nSNR vector can be expressed by  $\bar{\boldsymbol{\gamma}} = [\bar{\gamma}_0 \ \bar{\gamma}_1 \ \dots \ \bar{\gamma}_{N-1}]^T$  and the nSNR diagonal matrix can, on the other hand, be expressed by  $\mathbf{\Lambda}_{\bar{\boldsymbol{\gamma}}} = \mathbf{diag}\{\bar{\gamma}_0, \bar{\gamma}_1, \dots, \bar{\gamma}_{N-1}\}$ , which is used in the resource allocation problem. Furthermore, the SNR diagonal matrix is expressed by

$$\begin{aligned} \mathbf{\Lambda}_{\boldsymbol{\gamma}} &= \mathbf{diag}\{\gamma_0, \gamma_1, \dots, \gamma_{N-1}\} \\ &= \frac{1}{2} \mathbf{\Lambda}_P \mathbf{\Lambda}_{\bar{\boldsymbol{\gamma}}}, \end{aligned} \quad (5.9)$$

in which  $\gamma_k$  is the SNR at the  $k^{th}$  subchannel,  $\mathbf{\Lambda}_P = \mathbf{diag}\{P_0, P_1, \dots, P_{N-1}\}$ ,  $P_k$  is the portion of the total transmission power allocated for transmitting data through the  $k^{th}$  subchannel and  $\text{Tr}(\mathbf{\Lambda}_P)$  is the total transmission power.

The data rate maximization is obtained by solving a resource allocation problem, which allocates portions of the total transmission power and bits to each subcarrier. For the sake of simplicity, the operator that returns these allocations can be expressed by

$$[\mathbf{\Lambda}_{b^o}, \mathbf{\Lambda}_{P^o}] = f(\mathbf{\Lambda}_{\bar{\boldsymbol{\gamma}}}, P_t, \Gamma), \quad (5.10)$$

where  $\text{Tr}(\mathbf{\Lambda}_P) \leq P_t$ ,  $\Gamma$  denotes a gap factor from the Shannon capacity curve that accounts for the deployment of practical modulation and coding schemes [39, 42, 44];  $\mathbf{\Lambda}_{b^o} = \mathbf{diag}\{b_0^o, b_1^o, \dots, b_{N-1}^o\}$ ;  $\mathbf{\Lambda}_{P^o} = \mathbf{diag}\{P_0^o, P_1^o, \dots, P_{N-1}^o\}$ ;  $b_k^o$  and  $P_k^o$  are the optimal number of bits and the portion of the total transmission power allocated to the  $k^{th}$  subcarrier, respectively. Hence, the optimal data rate is  $R^o = \text{Tr}(\mathbf{\Lambda}_{b^o})/T_{\text{sym}}$ .

The exploitation, in Chapter 4, of existing relationship among the elements of (5.8) resulted in the introduction of the SCRA technique. As it is well-known, the choice of the representative nSNR of the chunk may considerably influence the output of the resource allocation technique. For the sake of simplicity, the operator that implements the SCRA technique for the OFDM scheme can be expressed by

$$[\mathbf{\Lambda}_b, \mathbf{\Lambda}_P] = g(\mathbf{\Lambda}_{\bar{\boldsymbol{\gamma}}}, N, P_t, \Gamma, L_c), \quad (5.11)$$

where  $g(\cdot)$  denotes the implementation of the algorithm shown in Fig. 19 and  $L_c$  is the chunk length. Moreover, the data rate obtained using this technique is  $R = \text{Tr}(\mathbf{\Lambda}_b)/T_{\text{sym}}$  and the corresponding data rate loss ratio is  $\eta = 1 - R/R^o$ , as addressed in Chapter 4.

The optimal resource allocation technique applied to the OFDM scheme exploits the fact that the nSNR does not vary in the time domain during one OFDM symbol interval, since it is assumed that the PLC channel is LTI and the PLC additive noise is stationary within an OFDM symbol. Fig. 26a shows the time-frequency representation of the nSNR during an OFDM symbol interval for  $2N = 16$ , in which different texture for each tile represents a distinct nSNR value. Note that each tile (subcarrier) for the OFDM scheme is supposed to have a different nSNR. Therefore, if the SCRA technique is applied in order to reduce the computational complexity of a resource allocation technique, then subcarriers are grouped in a chunk, which is represented by the minimal nSNR of all subchannels associated with the subcarriers belonging to the chunk, in order to ensure that the SER constraint is not violated. Thus, the subchannels with the nSNR values, which are higher than the minimal nSNR, will transmit fewer bits than they potentially could transmit and, as a consequence, more data rate loss is observed. However, if the tiles could have geometries with distinct trade off between time and frequency spreads, then the data rate loss could occasionally decrease.

Fig. 26b illustrates a tile geometry that is different from the one obtained by the DFT within an OFDM symbol. Note that it is not possible guarantee that the nSNR of the tiles are equal or not to the nSNR of the tiles associated with OFDM scheme. However, if there is, or can be designed, a time-frequency transform that could, under some constraints, offer tile geometries within an OFDM symbol different from the one obtained with the DFT and distinct tiles with the same nSNR, as illustrated Fig. 26b. In that situation, this time-frequency transform could be exploited to introduce a new multicarrier scheme, which can be combined with the SCRA technique in order to reduce the computational complexity with a data rate loss ratio lower than the one obtained with the SCRA technique applied to the OFDM scheme.

In this context, the following research question arises:

*Is it possible to come up with low-cost multicarrier scheme that is capable of offering different tile geometries from the DFT in order to reduce the computational complexity of resource allocation in PLC systems with smaller data rate loss than that one attained with the SCRA technique applied to the OFDM scheme?*

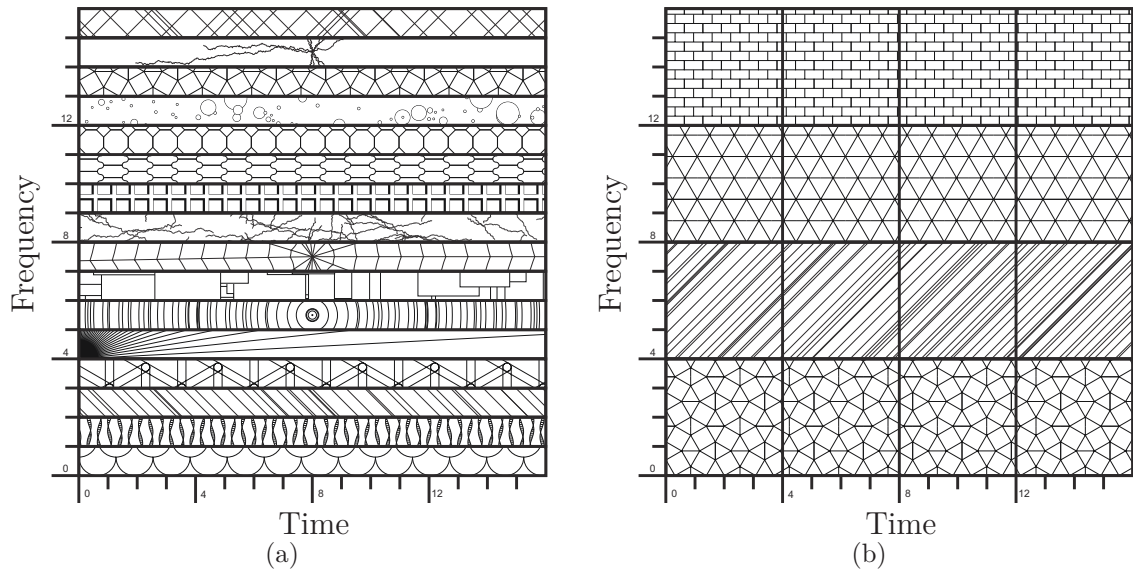


Figure 26: Examples of tile geometry at the time-frequency domain for (a) OFDM scheme and (b) hypothetic time-frequency representation when  $2N = 16$ .

## 5.2 THE OTFDM SCHEME BASED ON THE DOST

In order to answer the research question posed at the end of Section 5.1, this section outlines a new multicarrier scheme that can offer different trade offs between time and frequency resolution of the tiles. Due to its inherent characteristics, the following advantages are offered by the OTFDM scheme based on the discrete orthogonal Stockwell transform (DOST):

- The DOST can be efficiently implemented with the fast Fourier transform (FFT) [73, 74].
- Similar to the OFDM scheme, the OTFDM scheme can exploit the properties of the circulant channel convolution matrix and, as a consequence, the FDE can be easily implemented.
- The DOST is capable of yielding tiles in the time-frequency domain with different geometries in a very efficient way.
- Similar to OFDM scheme, the OTFDM scheme can be adapted to operate in the baseband or passband. If the OTFDM scheme operates in the baseband, then it can be named hermitian symmetric OTFDM (HS-OTFDM).

In order to describe the OTFDM scheme, this section is organized as follows: Subsection 5.2.1 deals with the DOST; Subsection 5.2.2 focuses on the OTFDM scheme; the SNR and the nSNR in each tile are deduced in Subsection 5.2.3; and Subsection 5.2.4 discusses a strategy to apply the SCRA technique in the OTFDM scheme.

### 5.2.1 The discrete orthogonal Stockwell transform

The DOST is a time-frequency transform proposed in [69]. The usefulness of the DOST has been recognized in image compression [73,75], face recognition [76], and image restoration [77]. Recently, a fast algorithm to efficiently implement the DOST using the FFT has been introduced in [73,74].

According to the DOST, each tile yielded by the DOST is localized in the time-frequency space based on a set of three parameters:  $\nu \in \mathbb{Z}$ , which specifies the tile center frequency;  $\beta \in \mathbb{Z}_*$ , which represents the tile bandwidth; and  $\tau \in \mathbb{Z}$ , which determines the tile location in the time domain. The basis function associated with the tile located at the coordinates  $[\nu, \beta, \tau]$  is given by [69,73]

$$D[n]_{[\nu, \beta, \tau]} = \frac{1}{\sqrt{\beta}} \sum_{k=\nu-\lfloor \beta/2 \rfloor}^{\nu+\lfloor \beta/2 \rfloor-1} e^{-i2\pi \frac{\nu}{M}k} e^{i2\pi \frac{\tau}{\beta}k} e^{-i\pi\tau}, \quad (5.12)$$

where  $M$  denotes the length of the transform. Moreover, the set of all tiles with same  $\nu$  is named voice. In other words, the voice is the set of tiles with the same frequency band. It is important to mention that to correctly apply the DOST and, as a consequence, to ensure orthogonality in the time-frequency domain, the following rules must be applied to specify the tile geometries [69]:

- $\nu$  and  $\beta$  must be selected so that each sample in the frequency domain is used only once.
- $\tau = 0, 1, \dots, \beta - 1$ .

The inner product between  $D[n]_{[\nu, \beta, \tau]}$  and a discrete-time sequence with  $M$  coefficients  $\{\dot{x}[n]\}_{n=0}^{M-1}$  (a dot over the lower case letter is used to indicate a coefficient in the time domain from the DOST) results in the DOST coefficient located at the coordinates  $[\nu, \beta, \tau]$  that can be expressed by

$$\begin{aligned} \ddot{X}_{[\nu, \beta, \tau]} &= \langle D[n]_{[\nu, \beta, \tau]}, \dot{x}[n] \rangle \\ &= \frac{1}{\sqrt{\beta}} \sum_{n=0}^{M-1} \dot{x}[n] \sum_{k=\nu-\lfloor \beta/2 \rfloor}^{\nu+\lfloor \beta/2 \rfloor-1} e^{-i2\pi \frac{\nu}{M}k} e^{i2\pi \frac{\tau}{\beta}k} e^{-i\pi\tau}, \end{aligned} \quad (5.13)$$

where two dots over the upper case letter is used to indicate a coefficient in the DOST domain and  $\langle a[n], b[n] \rangle$  denotes the inner product between  $a[n]$  and  $b[n]$ . Note that (5.13) can be rewritten as

$$\begin{aligned} \ddot{X}_{[\nu, \beta, \tau]} &= \frac{1}{\sqrt{\beta}} \sum_{k=\nu-\lfloor \beta/2 \rfloor}^{\nu+\lfloor \beta/2 \rfloor-1} \left[ \sum_{n=0}^{M-1} \dot{x}[n] e^{-i2\pi \frac{\nu}{M}k} \right] e^{i2\pi \frac{\tau}{\beta}k} e^{-i\pi\tau} \\ &= \frac{1}{\sqrt{\beta}} \sum_{k=\nu-\lfloor \beta/2 \rfloor}^{\nu+\lfloor \beta/2 \rfloor-1} \dot{X}[k] e^{i2\pi \frac{\tau}{\beta}k} e^{-i\pi\tau} \\ &= \langle \bar{D}[k]_{[\nu, \beta, \tau]}, \dot{X}[k] \rangle, \end{aligned} \quad (5.14)$$

where a dot over the upper case letter is used to indicate a coefficient in the frequency domain from the DOST (i.e.,  $\dot{X}[k]$  is the  $k^{\text{th}}$  coefficient of the  $M$ -length DFT of  $\{\dot{x}[n]\}$ ) and

$$\bar{D}[k]_{[\nu, \beta, \tau]} = \begin{cases} \frac{1}{\sqrt{\beta}} e^{i2\pi \frac{\tau}{\beta} k} e^{-i\pi \tau} & \nu - \lfloor \beta/2 \rfloor \leq k \\ & \leq \nu + \lceil \beta/2 \rceil - 1 \\ 0, & \text{otherwise} \end{cases} \quad (5.15)$$

It is important to emphasize that the representation of the sequence in the time-frequency domain, based on the DOST, can be obtained from the time domain by using  $D[n]_{[\nu, \beta, \tau]}$ ,  $n = 0, 1, \dots, M-1$ , or from the frequency domain by using  $\bar{D}[k]_{[\nu, \beta, \tau]}$ ,  $k = 0, 1, \dots, M-1$ . This information is very important because each of them leads to a different way to implement the OTFDM scheme.

Also, the time-frequency representation of a signal can be obtained by using a matrix formulation. To do so,  $\{\dot{x}[n]\}_{n=0}^{M-1}$  is replaced by the vector  $\dot{\mathbf{x}} = [\dot{x}[0], \dot{x}[1], \dots, \dot{x}[M-1]]^T \in \mathbb{C}^{M \times 1}$ , so that the DOST coefficients are obtained with  $\ddot{\mathbf{X}} = \mathbf{D}\dot{\mathbf{x}}$ , where  $\ddot{\mathbf{X}} = [\ddot{X}_0, \ddot{X}_1, \dots, \ddot{X}_{M-1}]^T$ ;  $\ddot{X}_l = \ddot{X}_{[\nu_l, \beta_l, \tau_l]}$  is the DOST coefficient associated with the  $l^{\text{th}}$  tile, which is located at the coordinates  $[\nu_l, \beta_l, \tau_l]$ ;  $\mathbf{D} = [\mathbf{D}_0, \mathbf{D}_1, \dots, \mathbf{D}_{M-1}]^T \in \mathbb{C}^{M \times M}$ ; and  $\mathbf{D}_l = [D[0]_{[\nu_l, \beta_l, \tau_l]}, D[1]_{[\nu_l, \beta_l, \tau_l]}, \dots, D[M-1]_{[\nu_l, \beta_l, \tau_l]}]^T \in \mathbb{C}^{M \times 1}$  [73]. As the DOST basis functions are orthogonal, then one can write  $\mathbf{D}\mathbf{D}^\dagger = \mathbf{M}\mathbf{I}_M$  and thereby  $\dot{\mathbf{x}} = \frac{1}{M}\mathbf{D}^\dagger\ddot{\mathbf{X}}$ . Furthermore, one obtain the time-frequency representation of a signal from its frequency domain representation by using  $\ddot{\mathbf{X}} = \bar{\mathbf{D}}\dot{\mathbf{X}}$ , where  $\dot{\mathbf{X}} = \mathbf{W}_M\dot{\mathbf{x}}$ ,  $\bar{\mathbf{D}} = [\bar{\mathbf{D}}_0, \bar{\mathbf{D}}_1, \dots, \bar{\mathbf{D}}_{M-1}]^T \in \mathbb{C}^{M \times M}$  and  $\bar{\mathbf{D}}_l = [\bar{D}[0]_{[\nu_l, \beta_l, \tau_l]}, \bar{D}[1]_{[\nu_l, \beta_l, \tau_l]}, \dots, \bar{D}[M-1]_{[\nu_l, \beta_l, \tau_l]}]^T \in \mathbb{C}^{M \times 1}$  [73]. As  $\bar{\mathbf{D}}\bar{\mathbf{D}}^\dagger = \mathbf{I}_M$ , then one can write  $\dot{\mathbf{X}} = \bar{\mathbf{D}}^\dagger\ddot{\mathbf{X}}$ . Note that if  $\beta_l = 1$  for  $l = 0, 1, \dots, M-1$ , then  $\bar{\mathbf{D}} = \mathbf{I}_M$  and  $\mathbf{D} = \mathbf{W}_M$ , which means that the DFT is a particular case of the DOST.

To ensure that  $\ddot{\mathbf{X}} \in \mathbb{C}^{M \times 1}$  is hermitian symmetric when  $\dot{\mathbf{x}} \in \mathbb{R}^{M \times 1}$  (or vice versa), the following rules must be applied [73]:

- $l$  must be symmetric in the frequency domain as illustrated in Fig. 27 for  $M = 16$ .
- $M$  and  $\beta$  must be powers of two.
- $\beta_0 = 1$  and  $\beta_{M/2} = 1$ .

In the literature, the most used tile geometry in the DOST is the octave geometry (also known as ‘‘octave sampling’’ [69, 73]), see Fig. 27a. However, any valid tile geometry (i.e., following the aforementioned rules) can be used. In this context, another tile geometry that can be used is the so-called  $\mathcal{B}$  geometry, where  $\{\mathcal{B} \in \mathbb{N} | 1 \leq \mathcal{B} \leq M\}$ . This tile geometry is illustrated in Fig. 27b for  $\mathcal{B} = 2$  and  $M = 16$ . Note that the  $\mathcal{B}$  geometry is similar to the octave geometry, but if  $\beta_l > \mathcal{B}$  in the octave geometry, then  $\beta_l = \mathcal{B}$  in the  $\mathcal{B}$  geometry. In other words, if  $\beta_l > \mathcal{B}$ , then the  $l^{\text{th}}$  tile is divided so that  $\beta_l = \mathcal{B}$ . On the

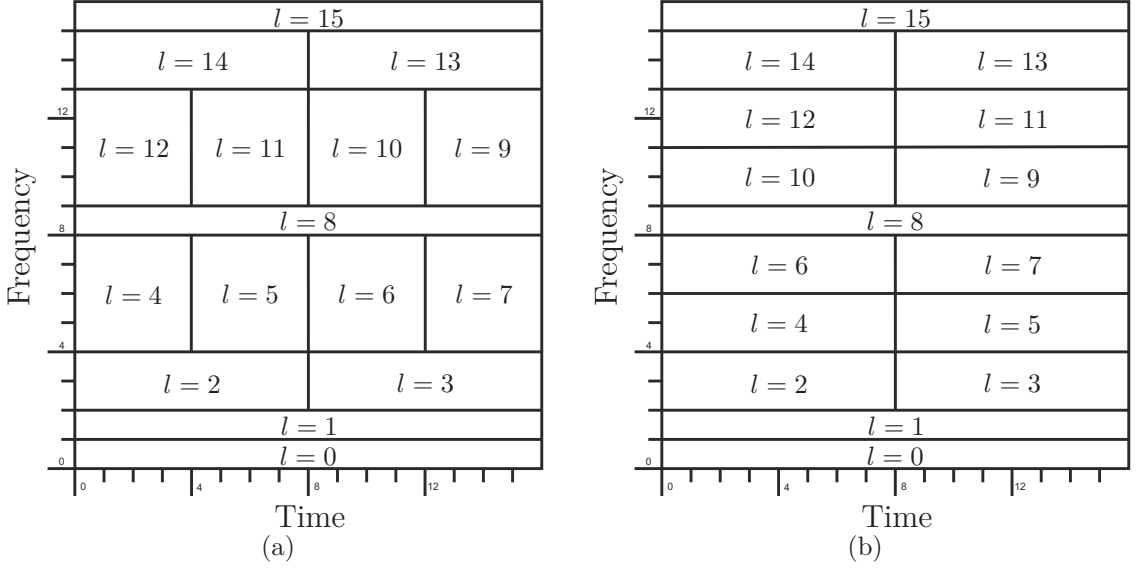


Figure 27: Examples of tile geometries of the time-frequency domain for  $M = 16$  and hermitian symmetric. (a) Octave geometry and (b)  $\mathcal{B}$  geometry with  $\mathcal{B} = 2$ .

other hand, if the  $l^{\text{th}}$  tile has  $\beta_l \leq \mathcal{B}$ , then this tile is equal at both tile geometries. The main advantage of the  $\mathcal{B}$  geometry is the fact that the majority of the tiles has the same bandwidth.

### 5.2.2 The OTFDM scheme

Fig. 28 illustrates a block diagram of a transmitter for the OTFDM scheme for working in the baseband, where  $\check{\mathbf{X}}_i = [\check{X}_{i,0}, \check{X}_{i,1}, \dots, \check{X}_{i,N-1}]^T \in \mathbb{C}^{N \times 1}$  is the  $i^{\text{th}}$  OTFDM symbol. The  $i^{\text{th}}$  OTFDM symbol with hermitian symmetry is obtained by applying the mapping described by (5.3) and its vectorial representation at the output of the block  $\mathcal{M}$  is expressed by  $\check{\mathbf{X}}_{\text{hs},i} = [\check{X}_{\text{hs},i,0}, \check{X}_{\text{hs},i,1}, \dots, \check{X}_{\text{hs},i,2N-1}]^T \in \mathbb{C}^{2N \times 1}$ . Next, assume  $\check{X}_{i,l}$ ,  $l = 0, 1, \dots, 2N - 1$ , is the signal information in the time-frequency domain associated with the  $l^{\text{th}}$  tile of a DOST of length  $M = 2N$  using any valid tile geometry. Note that the  $l^{\text{th}}$  tile occupies a bandwidth of  $\beta_l B_s$ . The time-domain representation of  $\check{\mathbf{X}}_i$  can be expressed by  $\dot{\mathbf{x}}_i = \frac{1}{\sqrt{2N}} \mathbf{D}^\dagger \check{\mathbf{X}}_{\text{hs},i}$ , in which  $\dot{\mathbf{x}}_i \in \mathbb{R}^{2N \times 1}$ . The  $L_{cp}$ -length cyclic prefix is included in this vector by using

$$\dot{\mathbf{x}}_{cp,i} = \begin{bmatrix} \mathbf{0} & \mathbf{I}_{L_{cp}} \\ & \mathbf{I}_{2N} \end{bmatrix} \dot{\mathbf{x}}_i, \quad (5.16)$$

which is represented by the CP-block in Fig. 28. Following this framework, the transmission signal is the infinite succession of OTFDM symbols with cyclic prefix in the discrete time domain, this step is represented by the parallel to serial (P/S) block of Fig. 28 and can be expressed by

$$\dot{x}[n] = \sum_{i=-\infty}^{\infty} \sum_{p=0}^{2N+L_{cp}-1} \dot{x}_{cp,i,p} \delta[n - i2N - j], \quad (5.17)$$

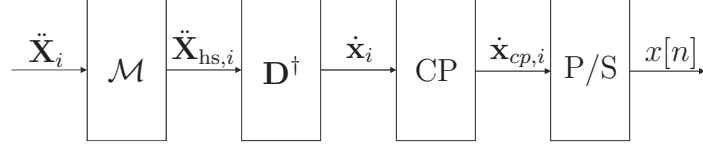


Figure 28: A block diagram to implement the transmitter of the OTFDM scheme in the baseband.

where  $\dot{x}[n] \in \mathbb{R}$  and  $\dot{x}_{cp,i,p}$  is the  $p^{\text{th}}$  element of the vector  $\dot{\mathbf{x}}_{cp,i}$ . Therefore, the OTFDM symbol interval is  $T_{\text{sym}} = (2N + L_{cp})/F_s$ .

Assuming perfect synchronization and CSI available at the receiver side, Fig. 29 illustrates two different receivers for the OTFDM scheme operating in the baseband, where  $\dot{r}[n]$  is the signal at the channel output. Both receivers (of Figs 29a and 29b) obtain the vector  $\dot{\mathbf{r}}_i \in \mathbb{R}^{2N+L_{cp} \times 1}$  and its corresponding vectorial representation, after the cyclic prefix removal. The  $i^{\text{th}}$  received OFDM symbol is expressed by  $\dot{\mathbf{y}}_i \in \mathbb{R}^{2N \times 1}$ . Therefore, the frequency-domain representation of vector  $\dot{\mathbf{y}}_i$  is given by

$$\begin{aligned} \dot{\mathbf{Y}}_i &= \frac{1}{\sqrt{2N}} \mathbf{W} \dot{\mathbf{y}}_i \\ &= \mathbf{\Lambda}_H \dot{\mathbf{X}}_{hs,i} + \mathbf{V}_i. \end{aligned} \quad (5.18)$$

The use of FDE based on ZF criterion (could be other criterion, such as the MMSE criterion) yields an estimate of the transmitted OTFDM symbol in the frequency domain, which is expressed by

$$\begin{aligned} \hat{\mathbf{X}}_{hs,i} &= \mathbf{\Lambda}_H^{-1} \dot{\mathbf{Y}}_i \\ &= \dot{\mathbf{X}}_{hs,i} + \mathbf{\Lambda}_H^{-1} \mathbf{V}_i. \end{aligned} \quad (5.19)$$

Note that this estimate is in the frequency domain and, of course, it does not represent  $\ddot{\mathbf{X}}_{hs,i}$ . In order to obtain an estimate of  $\ddot{\mathbf{X}}_{hs,i}$ , one of the following options may be used:

- The first option is illustrated by the block diagram showed in Fig. 29a. The main idea is to first evaluate an estimate of  $\hat{\dot{\mathbf{x}}}_i = (1/\sqrt{2N}) \mathbf{W}_{2N}^\dagger \hat{\mathbf{X}}_{hs,i}$  and, next, to obtain  $\hat{\mathbf{X}}_{hs,i}$  by applying the DOST, i.e.,  $\hat{\mathbf{X}}_{hs,i} = (1/\sqrt{2N}) \mathbf{D} \hat{\dot{\mathbf{x}}}_i$ . Note that this option makes use of the  $\mathbf{D}$  matrix.
- The second option to obtain  $\hat{\mathbf{X}}_{hs,i}$  is illustrated in Fig. 29b. Basically, it replaces the matrix  $\mathbf{D}$  by the  $\bar{\mathbf{D}}$  matrix because  $\bar{\mathbf{D}} = (1/2N) \mathbf{D} \mathbf{W}_{2N}^\dagger$  and, as a consequence, the need for applying the  $\mathbf{W}_{2N}^\dagger$  matrix in the vector  $\hat{\mathbf{X}}_{hs,i}$  and the  $\mathbf{W}_{2N}$  matrix together with the  $\mathbf{D}$  matrix is eliminated. In other words,

$$\begin{aligned} \hat{\mathbf{X}}_{hs,i} &= \bar{\mathbf{D}} \hat{\mathbf{X}}_{hs,i} \\ &= \bar{\mathbf{D}} \dot{\mathbf{X}}_{hs,i} + \bar{\mathbf{D}} \mathbf{\Lambda}_H^{-1} \mathbf{V}_i \\ &= \dot{\mathbf{X}}_{hs,i} + \bar{\mathbf{V}}_{h,i}, \end{aligned} \quad (5.20)$$

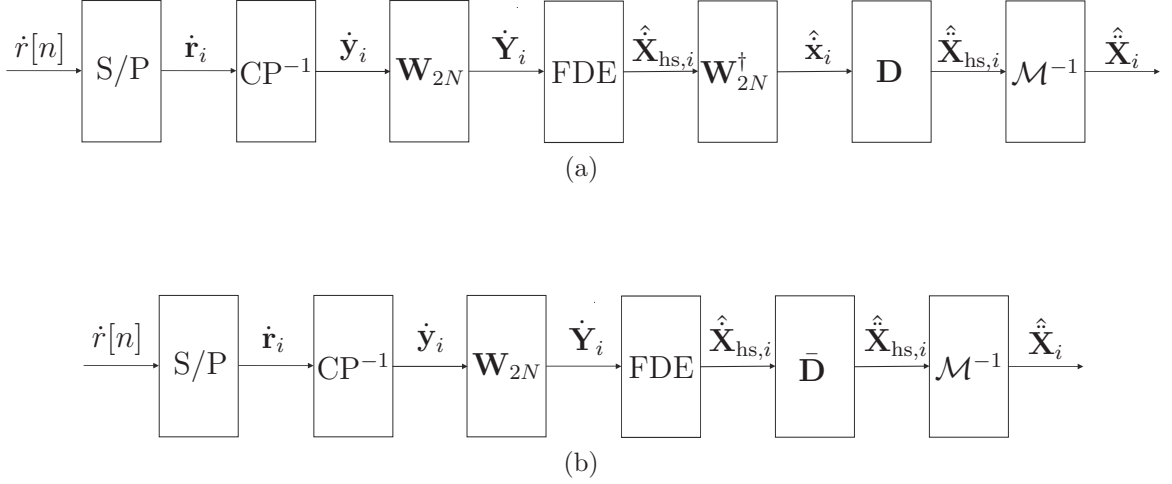


Figure 29: Block diagram of two options to implement the receiver of the OTFDM scheme in the baseband. (a) with high computational complexity and (b) with low computational complexity.

where  $\ddot{\mathbf{V}}_{h,i} = \bar{\mathbf{D}}\mathbf{\Lambda}_H^{-1}\mathbf{V}_i$  is the filtered noise in the time-frequency domain during the  $i^{th}$  OTFDM symbol interval.

Note that the second option demands lower computational complexity than the first one, since the later does not execute the inverse discrete Fourier transform (IDFT) and the DFT, as the former does. Also, the later uses the  $\bar{\mathbf{D}}$  matrix that, different from the full matrix  $\mathbf{D}$ , is a sparse matrix. Finally,  $\hat{\mathbf{X}}_i$ , which is an estimate of  $\ddot{\mathbf{X}}_i$ , is obtained by applying the inverse of (5.3) in  $\hat{\mathbf{X}}_{hs,i}$ , which is represented by the  $\mathcal{M}^{-1}$ -block in both Fig. 29a and Fig. 29b.

Note that, if the OTFDM scheme uses the  $\mathcal{B}$  geometry with  $\mathcal{B} = 1$ , then  $\bar{\mathbf{D}} = \mathbf{I}_{2N}$  and the OTFDM scheme becomes the OFDM scheme. Therefore, the OFDM scheme can be considered as a particular case of the OTFDM scheme. Finally, but not the least, the block diagrams for the OTFDM in baseband can be adapted to implement the OTFDM scheme in the passband. To do so, remove the  $\mathcal{M}$ -block and the  $\mathcal{M}^{-1}$ -block, then  $\ddot{\mathbf{X}}_{hs,i} = \ddot{\mathbf{X}}_i$  and all equations are valid by replacing  $2N$  by  $N$ .

### 5.2.3 The SNR in the OTFDM scheme

This subsection deduces the SNR of each tile of the OTFDM scheme and provides a relationship between it and the SNR of the tiles (subcarriers) of the OFDM scheme. Following the formulation for the OTFDM scheme, one notes that the power of the filtered noise in all tiles can be defined by

$$\begin{aligned} \mathbf{\Lambda}_{P_{v_h}} &\triangleq \mathbf{diag}\{P_{v_h,0}, P_{v_h,1}, \dots, P_{v_h,2N-1}\} \\ &= \mathcal{Z} \left( \frac{\mathbb{E}\{\ddot{\mathbf{V}}_{h,i} \ddot{\mathbf{V}}_{h,i}^\dagger\}}{2B} \right) B_s \end{aligned} \quad (5.21)$$

in which  $\mathcal{Z}(\cdot)$  is a function that sets off-diagonal elements to zero and  $P_{v_h,l}$  is the power of the filtered noise at the  $l^{\text{th}}$  tile. Note that if  $\check{\mathbf{V}}_{h,i}$  is replaced by  $\mathbf{V}_i$  in (5.21), then it returns the power of the noise in all tiles of the OFDM scheme. Rewriting (5.21), one can obtain

$$\begin{aligned}\Lambda_{P_{v_h}} &= \mathcal{Z} \left( \frac{\mathbb{E}\{\bar{\mathbf{D}}\Lambda_H^{-1}\mathbf{V}_i(\bar{\mathbf{D}}\Lambda_H^{-1}\mathbf{V}_i)^\dagger\}}{2B} \right) B_s \\ &= \mathcal{Z} \left( \bar{\mathbf{D}}\Lambda_H^{-1} \frac{\mathbb{E}\{\mathbf{V}_i\mathbf{V}_i^\dagger\}}{2B} \Lambda_H^{-1\dagger}\bar{\mathbf{D}}^\dagger \right) B_s \\ &= \mathcal{Z} \left( \bar{\mathbf{D}}\Lambda_{|H|^2}^{-1} \Lambda_{S_v} \bar{\mathbf{D}}^\dagger \right) B_s \\ &= \mathcal{Z} \left( \bar{\mathbf{D}}\Lambda_{\bar{\gamma},2N}^{-1} \bar{\mathbf{D}}^\dagger \right)\end{aligned}\tag{5.22}$$

and, as a consequence,  $P_{v_h,l}$  can be expressed by

$$\begin{aligned}P_{v_h,l} &= \sum_{k=\nu_l-\lfloor\beta_l/2\rfloor}^{\nu_l+\lceil\beta_l/2\rceil-1} |\bar{d}_{lk}|^2 \bar{\gamma}_k^{-1} \\ &= \frac{1}{\beta_l} \sum_{k=\nu_l-\lfloor\beta_l/2\rfloor}^{\nu_l+\lceil\beta_l/2\rceil-1} \bar{\gamma}_k^{-1},\end{aligned}\tag{5.23}$$

where  $\bar{\gamma}_k$  is the nSNR at the  $k^{\text{th}}$  subcarrier (see (5.8));  $\bar{d}_{lk}$  is the element of the  $\bar{\mathbf{D}}$  matrix in the  $l^{\text{th}}$  row and the  $k^{\text{th}}$  column; and, from (5.15),  $|\bar{d}_{lk}|^2 = 1/\beta_l$ . Note that the power of the filtered noise at the  $l^{\text{th}}$  tile is equal to the average of the inverse nSNR of all subcarriers occupying the time-frequency space covered by a voice of the DOST.

It is important to mention that the normalized SNR diagonal matrix for the OTFDM scheme can be defined by

$$\begin{aligned}\Lambda_{\check{\gamma},2N} &\triangleq \mathbf{diag}\{\check{\gamma}_0, \check{\gamma}_1, \dots, \check{\gamma}_{2N-1}\} \\ &= \left[ \mathcal{Z} \left( \bar{\mathbf{D}}\Lambda_{\bar{\gamma},2N}^{-1} \bar{\mathbf{D}}^\dagger \right) \right]^{-1} \\ &= \Lambda_{P_{v_h}}^{-1},\end{aligned}\tag{5.24}$$

where  $\check{\gamma}_l = 1/P_{v_h,l}$  is the nSNR at the  $l^{\text{th}}$  tile. Surprisingly, one can note that  $\check{\gamma}_l$  is the harmonic mean of  $\bar{\gamma}_k$  for  $\nu_l - \lfloor\beta_l/2\rfloor \leq k \leq \nu_l + \lceil\beta_l/2\rceil - 1$ .

The data transmission in PLC systems is performed in the baseband. Similar to the OFDM scheme operating in the baseband, the total transmission power and the bits are allocated only to  $N$  tiles and not to  $2N$  ones. Therefore, the nSNR vector for the OTFDM scheme can be expressed by  $\dot{\boldsymbol{\gamma}} = [\dot{\gamma}_0 \ \dot{\gamma}_1 \ \dots \ \dot{\gamma}_{N-1}]^T$  and the nSNR diagonal matrix can be expressed by  $\Lambda_{\dot{\boldsymbol{\gamma}}} = \mathbf{diag}\{\dot{\gamma}_0, \dot{\gamma}_1, \dots, \dot{\gamma}_{N-1}\}$ , which is the information to feed the resource allocation technique when the data transmission is over the baseband.

Finally, the SNR diagonal matrix for the OTFDM scheme is expressed by

$$\begin{aligned}\Lambda_{\dot{\boldsymbol{\gamma}}} &= \mathbf{diag}\{\dot{\gamma}_0, \dot{\gamma}_1, \dots, \dot{\gamma}_{N-1}\} \\ &= \frac{1}{2} \Lambda_{\dot{P}} \Lambda_{\bar{\boldsymbol{\gamma}}},\end{aligned}\tag{5.25}$$

where  $\dot{\gamma}_l$  is the SNR at the  $l^{\text{th}}$  tile;  $\mathbf{\Lambda}_{\dot{P}} = \mathbf{diag}\{\dot{P}_0, \dot{P}_1, \dots, \dot{P}_{N-1}\}$ ;  $\dot{P}_l$  is the portion of the total transmission power allocated for transmitting data through the  $l^{\text{th}}$  tile; and  $\text{Tr}(\mathbf{\Lambda}_{\dot{P}})$  is the total transmission power.

In order to illustrate the discussion about the SNR and the nSNR yielded by both OFDM and OTFDM schemes, it was assumed a measured in-home PLC channel with magnitude spectrum depicted in Fig. 30a, an additive noise modeled as AWGN with PSD of -109 dBW/Hz, and a total transmission power of -3 dBW uniformly distributed among the  $2N = 4096$  tiles of both OTFDM and OFDM schemes. The choice of the  $\mathcal{B}$  geometry with  $\mathcal{B} = 128$  for OTFDM scheme is made to facilitate the understanding.

Aiming to differentiate the behavior of the SNR associated with the OTFDM and the OFDM schemes, Fig. 30b shows the SNR value of each tile of the OTFDM scheme for  $\mathcal{B} = 128$  and the SNR of each tile (subcarrier) of the OFDM scheme. The  $l^{\text{th}}$  tile of the OTFDM scheme is compared to the  $k^{\text{th}}$  tile of the OFDM scheme due to the fact that both of them are related according to (5.23). Also, this plot shows the mean value of the SNR, in which the mean value is evaluated from all tiles of the OFDM within a voice of the DOST. The plot shows that the difference between such mean value and the SNR value associated with the OTFDM scheme can be relevant when the spread of the SNR amplitude associated with the OFDM scheme, inside one voice, is big. Based on the curves in Fig. 30b, it is clear that OTFDM scheme yields a constant value of SNR for all tiles within a voice when the noise is AWGN and it is always lower than the mean value and higher than the minimum value of the SNR associated with the OFDM scheme. This behavior of the OTFDM scheme is predicted by (5.24).

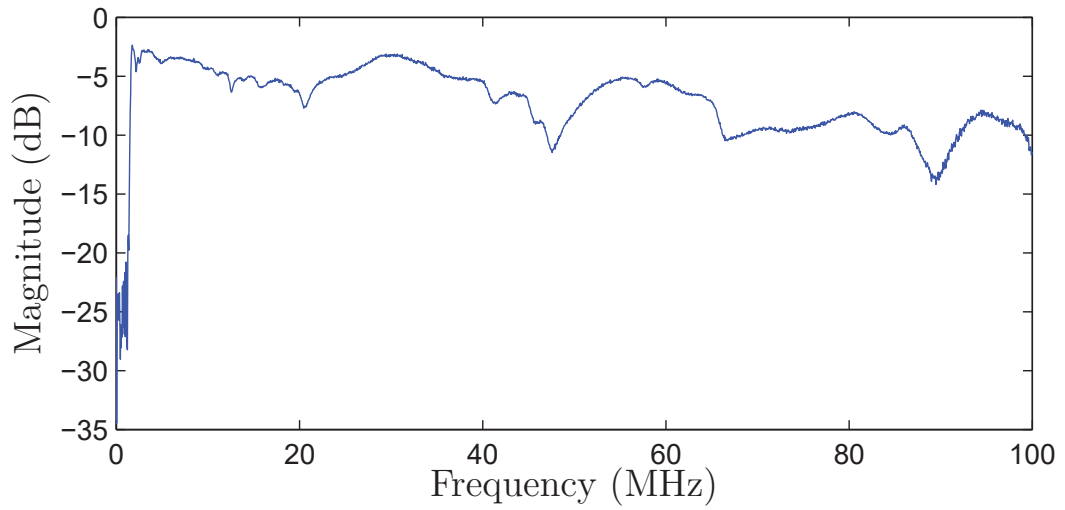
Finally, but not the least, Fig. 30c shows the performance in terms of SER at each tile for the OTFDM scheme ( $\mathcal{B} = 128$ ) with a 4-QAM modulation and the SNR for each tile is given by Fig. 30b. The curves show the SER analytically calculated with (5.24) for the OTFDM scheme and its corresponding results obtained with numerical simulations. These curves show that the results analytically or numerically obtained are almost the same. Such agreement confirms that (5.24) is correct.

#### 5.2.4 The resource allocation in the OTFDM scheme

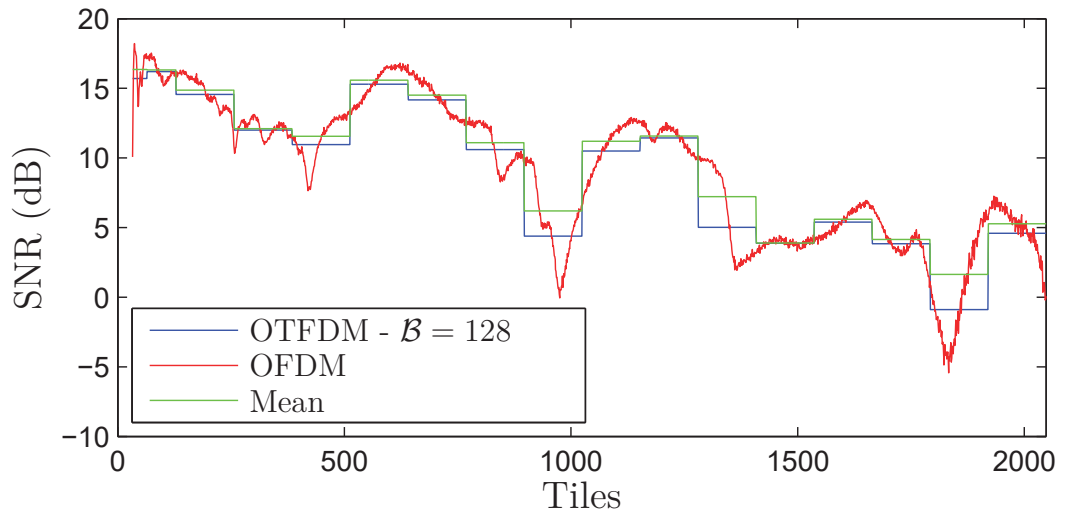
The OTFDM symbol is composed of independent and orthogonal tiles, thereby, any resource allocation technique initially design for an OFDM-based scheme can be directly applied to the OTFDM scheme, including the optimal and the SCRA techniques. In this context, the optimal resource allocation applied to the OTFDM scheme can be expressed by

$$[\mathbf{\Lambda}_{\dot{b}^o}, \mathbf{\Lambda}_{\dot{P}^o}] = f(\mathbf{\Lambda}_{\dot{\gamma}}, P_t, \Gamma), \quad (5.26)$$

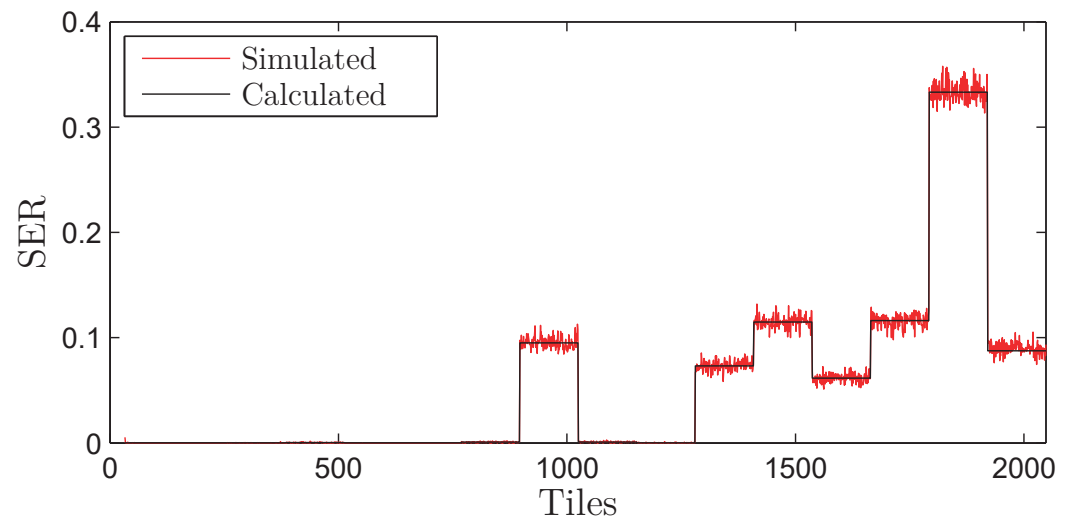
where  $\mathbf{\Lambda}_{\dot{b}^o} = \mathbf{diag}\{\dot{b}_0^o, \dot{b}_1^o, \dots, \dot{b}_{N-1}^o\}$ ;  $\mathbf{\Lambda}_{\dot{P}^o} = \mathbf{diag}\{\dot{P}_0^o, \dot{P}_1^o, \dots, \dot{P}_{N-1}^o\}$ ;  $\dot{b}_l^o$  and  $\dot{P}_l^o$  are the optimal number of bits and the portion of the total transmission power allocated to the



(a)



(b)



(c)

Figure 30: Comparison between the OFDM and OTFDM (using  $\mathcal{B}$  geometry with  $\mathcal{B} = 128$ ) schemes. (a) the CFR of the PLC channel (b) the SNR per tile and (c) the SER per tile of the OTFDM scheme.

$l^{\text{th}}$  tile, respectively. Therefore, the optimal data rate is  $\dot{R}^o = \text{Tr}(\mathbf{\Lambda}_{\dot{b}^o})/T_{\text{sym}}$ . Note that this result is optimal for the OTFDM scheme; however,  $\dot{R}^o$  is smaller than  $R^o$ , which is the optimal data rate for the OFDM scheme. In fact, simulation results, discussed in Section 5.3, show that  $\dot{R}^o \leq R^o$ , since the data rate loss ratio expressed by  $\eta = 1 - \dot{R}^o/R^o$  is such that  $0 \leq \eta \leq 1$ . Moreover, the computational complexity of the optimal resource allocation technique applied to both schemes is the same, since the number of tiles in both schemes is equal.

To exploit the fact that the nSNR is equal in all tiles within a voice, the use of the SCRA technique is strongly recommended. This resource allocation technique applied to the OTFDM scheme can be expressed by

$$[\mathbf{\Lambda}_{\dot{b}}, \mathbf{\Lambda}_{\dot{p}}] = g(\mathbf{\Lambda}_{\dot{\gamma}}, N, P_t, \Gamma, L_c), \quad (5.27)$$

where  $\mathbf{\Lambda}_{\dot{b}} = \mathbf{diag}\{\dot{b}_0, \dot{b}_1, \dots, \dot{b}_{N-1}\}$ ;  $\dot{b}_l$  is the number of bits allocated to the  $l^{\text{th}}$  tile. Similar to what was discussed in Chapter 4, the SCRA technique yields data rate  $\dot{R} = \text{Tr}(\mathbf{\Lambda}_{\dot{b}})/T_{\text{sym}}$  and the data rate loss ratio relative to the optimal data rate obtained with the OFDM scheme is evaluated by  $\eta = 1 - \dot{R}/R^o$ . Moreover, the gain in terms of computational complexity can be evaluated by  $\rho = 1 - 1/L_c$ .

Based on Chapter 4 and supported by simulation results, discussed in Section 5.3, the following rules must be applied to the SCRA technique properly work together with the OTFDM-based scheme to obtain the best trade off between computational complexity reduction ratio and the data rate loss ratio:

- The SCRA technique must be configured to use the minimal value of the nSNR that represents a chunk (set of tiles), in order to ensure the SER constraint is not violated.
- The OTFDM must use the  $\mathcal{B}$  geometry with  $\mathcal{B} = L_c$  being a power of two, in order to obtain the minimal data rate loss ratio. It is mandatory because the SCRA technique in the constant mode assumes all chunks with the same length and the number of tiles occupying a time-frequency region of a voice of a valid geometry.
- The SCRA technique must be configured to work in the constant mode, since the adaptive mode implies in  $L_c = B_{c,\bar{\gamma}}/B_s$ , where  $B_{c,\bar{\gamma}}$  is defined in Chapter 3, and, as a consequence,  $L_c$  may not be power of two.
- $\mathcal{B}$  must be chosen based on statistical analyses of the nSNR coherence bandwidth by taking into account that the largest bandwidth in  $\mathcal{B}$  geometry is equal to  $\mathcal{B}B_s$ . This is important because the voice with bandwidth higher than the nSNR coherence bandwidth results in a high data rate loss ratio.

### 5.3 PERFORMANCE ANALYSES

This section addresses performance analyses of the OTFDM scheme in baseband by adopting octave and  $\mathcal{B}$  geometries. These geometries are analyzed, since the first one is the most used in the literature for DOST applications and the second one is an interesting suggested tile geometry because the majority of the voices have the same number of tiles, something that facilitates the use of the concept of chunk for the SCRA technique.

#### 5.3.1 The transmitter without CSI

This subsection analyzes the performance in terms of SER of PLC systems based on the OTFDM scheme when the CSI is not available at the transmitter side. Moreover, it compares the results with PLC systems based on the OFDM scheme, under the same conditions. To do so, the simulations assume ideal channel, i.e.,  $h[n] = \delta[n]$ , in order to analyze only the PLC additive noise effect on the performance of the OTFDM scheme. Moreover,  $B = 100$  MHz,  $2N = 4096$ , 4-QAM and the total transmission power of -10 dBW. As the transmitter does not know the CSI, then the total transmission power is uniformly distributed among the subcarriers/tiles (OFDM scheme) and among the tiles (OTFDM scheme), in order to obtain the SER performance.

Fig. 31 shows the OFDM and OTFDM schemes performances in terms of SER, when the additive noise is modeled as AWGN, i.e.  $v[n] = v_{bkgr}[n]$ . In this figure,  $E_b/N_0$  denotes the energy per bit to background noise power spectral density ratio. Also, in the legend of this figure the expressions “Octave”, “ $\mathcal{B} = 8$ ” and “ $\mathcal{B} = 128$ ” make reference to the tile geometries used to implement the OTFDM scheme. Note that the OFDM scheme and OTFDM scheme, disregarding the tile geometries, attain the same performance in terms of SER. It means that the SER performance is not modified by the tile geometry when the additive noise is AWGN, since such noise is equally spread all over time-frequency domain.

Fig. 32 illustrates the SER performance of the OFDM and OTFDM schemes, when the additive noise is composed of background noise and NBI components, i.e.  $v[n] = v_{bkgr}[n] + v_{nbi}[n]$ , where  $v_{nbi}[n]$  is modeled by (5.2) with  $\Upsilon = 7$ ,  $k_c = 1638$  and  $P_{nbi,c} = 7$  dB. Note that the performance in terms of SER depends on the tile geometry and the OTFDM scheme can yield better SER performance than the OFDM scheme. Among the OTFDM schemes, the worst SER performance was achieved by the OTFDM scheme with  $\mathcal{B} = 128$ . On the other hand, the OTFDM scheme with octave geometry and  $\mathcal{B}$  geometry (with  $\mathcal{B} = 8$ ) attained better performance, in terms of SER, than the OFDM scheme. Moreover, the OTFDM scheme with octave geometry does not show an error floor for SER higher than  $10^{-6}$ . Actually, for the octave geometry the OTFDM scheme performance is impressive. Overall, the plots in Fig. 32 show that, for a given tile geometry, the OTFDM scheme can be a good alternative for designing multicarrier based PLC systems when the

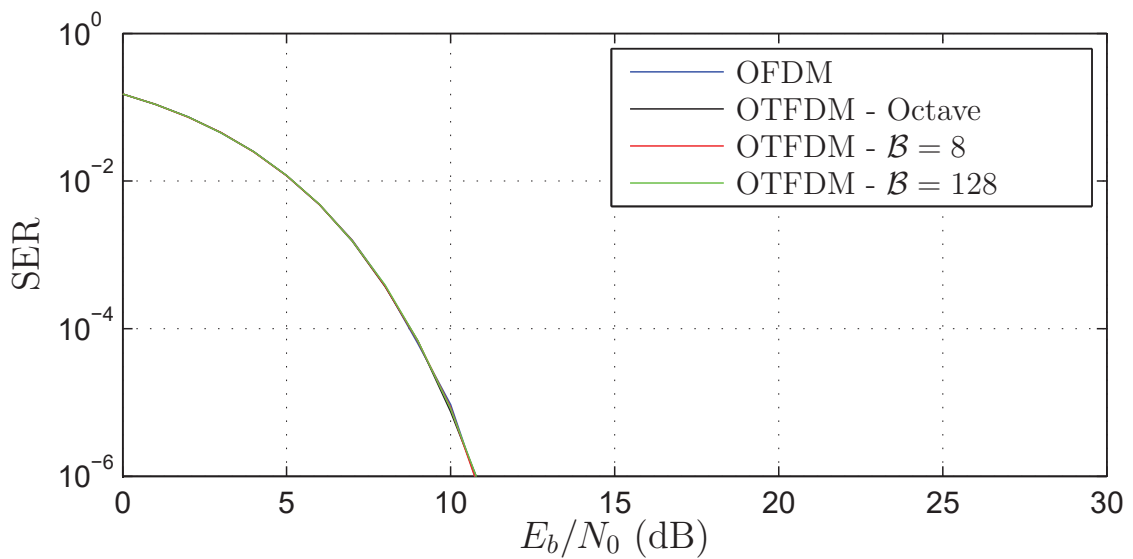


Figure 31: The SER performances of the OFDM and the OTFDM schemes impaired by the background noise modeled as AWGN.

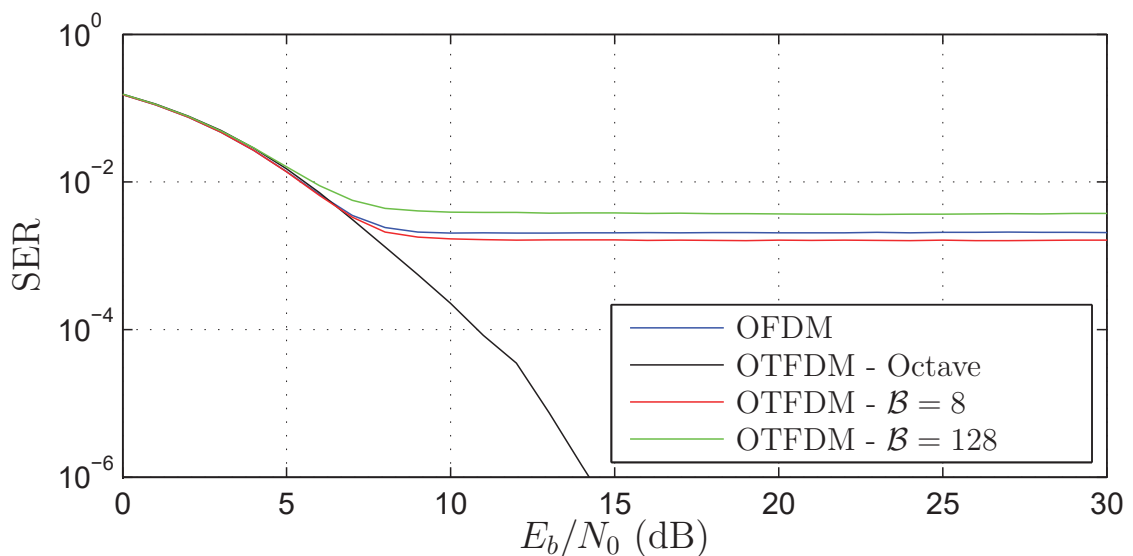


Figure 32: The SER performances of the OFDM and the OTFDM schemes impaired by the background noise modeled as AWGN and the NBI component.

additive noise is composed of AWGN and NBI components.

Fig. 33 shows the SER performance of the OFDM and OTFDM schemes impaired by an additive noise constituted by background and impulsive (synchronous and asynchronous) components, i.e.,  $v[n] = v_{bkgr}[n] + v_{ps}[n] + v_{imp}[n]$ . To obtain these curves, the impulsive noise component were modeled using  $K = 1000$ ,  $T_{w,ps} = T_{w,imp} = 1 \mu s$  and  $\bar{t}_{arr,imp} = 10$  ms. Note that the chosen tile geometry for the OTFDM scheme offers distinct SER performances. The curves show that the OTFDM scheme yields larger error floor than the OFDM scheme. Moreover, OTFDM obtains better performance in terms of SER for some  $E_b/N_0$  values than the OFDM scheme, whereas the latter achieves bet-

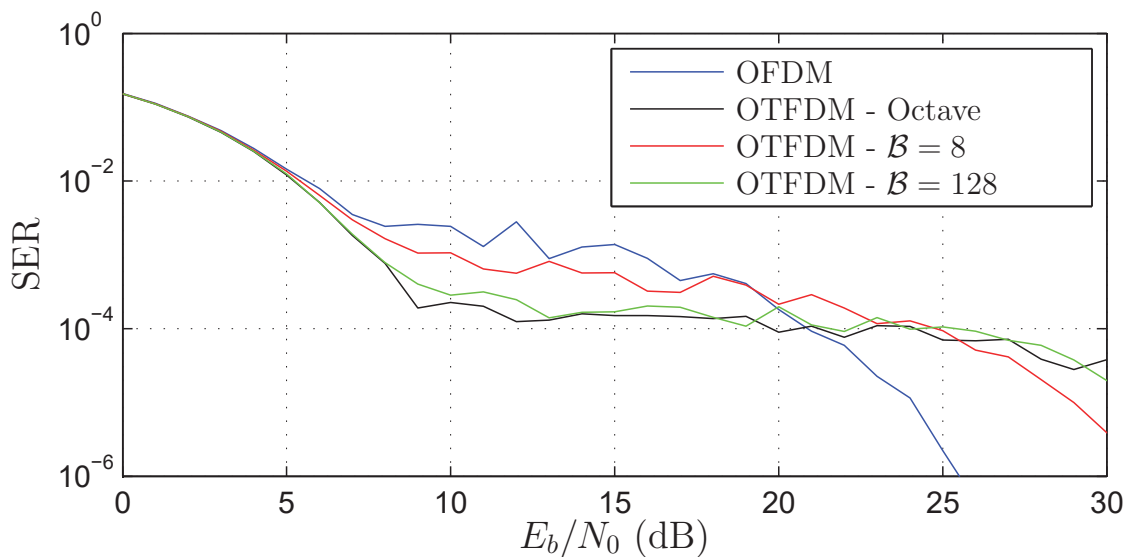


Figure 33: SER performance of the OFDM and OTFDM schemes impaired by the background noise and impulsive noise components.

ter performance in terms of SER for high  $E_b/N_0$  values. These results indicate that the OFDM scheme offers the best performance for high  $E_b/N_0$  when the PLC additive noise is composed of impulsive noise and the CSI is not available at the transmitter side.

The results discussed in this section makes clear that the lack of the CSI at the transmitter side may not benefit the data communication based on the OTFDM scheme.

### 5.3.2 The transmitter with CSI

This subsection analyzes the performance of the optimal resource allocation and the SCRA technique in terms of SER, data rate loss ratio and computational complexity reduction ratio, when the OTFDM scheme is applied with CSI. Also, it discusses a comparison with the OFDM scheme, under the same conditions. This analysis is very important because it addresses the real conditions of a multicarrier-based PLC system operation dedicated to broadband data communication. For this analysis,  $\Gamma(\text{dB}) = 9.3$  dB is adopted to ensure that the peak SER is lower than  $10^{-6}$ . Furthermore, this analysis is based on the same data set used in Section 3.3.1.

Fig. 34 shows the CCDF of the data rate loss ratio relative to the optimal resource allocation for the OFDM scheme and for the OTFDM scheme (see (5.26)) with different tile geometries. For this plot, the frequency band is from 1.7 MHz up to 100 MHz,  $P(\eta > x)$  indicates the probability of the data rate loss ratio being higher than  $x$ , and the reference data rate is the optimal data rate obtained when the OFDM scheme applies. Note that the optimal resource allocation technique applied to the OTFDM scheme results in a data rate loss ratio for all data set independent from the tile geometry. It means that the OTFDM scheme achieves smaller data rate than the OFDM scheme, under the same

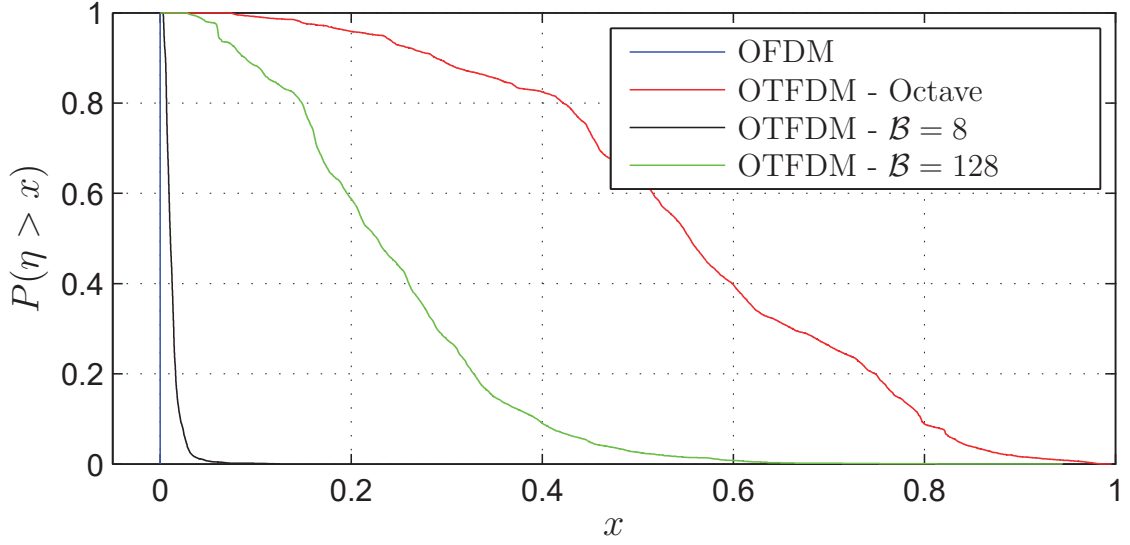


Figure 34: The CCDFs of the data rate loss ratio ( $\eta$ ) when the optimal resource allocation technique is applied to the OFDM scheme and to the OTFDM scheme considering several tile geometries.

conditions. This makes sense by taking a look at the curves showed in Fig 30b. Moreover, the tile geometry with the smallest data rate loss ratio is the  $\mathcal{B}$  geometry when  $\mathcal{B} = 8$ . It occurs because the largest voice bandwidth is 390.4 kHz, because  $B_s = 48.8$  kHz, and, based on the Chapter 3, the nSNR coherence bandwidth for in-home PLC channel has mean value around 600 kHz. It means that all voices having bandwidth smaller than the mean value of the nSNR coherence bandwidth will yield small data rate loss ratio in comparison with other geometries. Note that if  $\mathcal{B} = 128$ , then the largest voice bandwidth is 6.24 MHz, which does not comply with the nSNR coherence bandwidth.

Fig. 35 shows the performance of the SCRA technique in terms of data rate loss ratio applied to the OTFDM scheme, for different values of  $L_c$ , and to the OFDM scheme. For this plot, the frequency band is from 1.7 MHz up to 100 MHz;  $\mathcal{B}$  geometry assumes  $\mathcal{B} = 8$ ; and the SCRA technique makes use of the minimal value of nSNR to represent the chunk. The curve with  $L_c = 1$  correspond to the optimal resource allocation applied to the OTFDM scheme. Note that it yields data rate loss ratio, since the ratio compares the data rate of the OTFDM scheme with respect to the optimal data rate obtained with the OFDM scheme. Moreover, the SCRA technique with  $L_c = 16$  achieves the highest data rate loss ratio, because each chunk groups tiles of two voices, since each voice has only 8 tiles ( $\mathcal{B} = 8$ ). Note that tiles of different voices can have distinct nSNRs. Another interesting result is the fact that the SCRA technique offers the same data rate loss ratio for  $L_c = 1$ ,  $L_c = 4$  and  $L_c = 8$ , when the tile geometry is  $\mathcal{B} = 8$ . It means that all tiles with the same voice can be grouped in a chunk without increasing the data rate loss ratio. However,  $L_c = 8$  attains the highest computational complexity reduction ratio ( $\rho = 0.88$ ). In other words, if  $L_c = \mathcal{B}$  such that  $\mathcal{B}B_s \leq B_{c,\overline{\gamma}}$ , then the SCRA technique yields the best

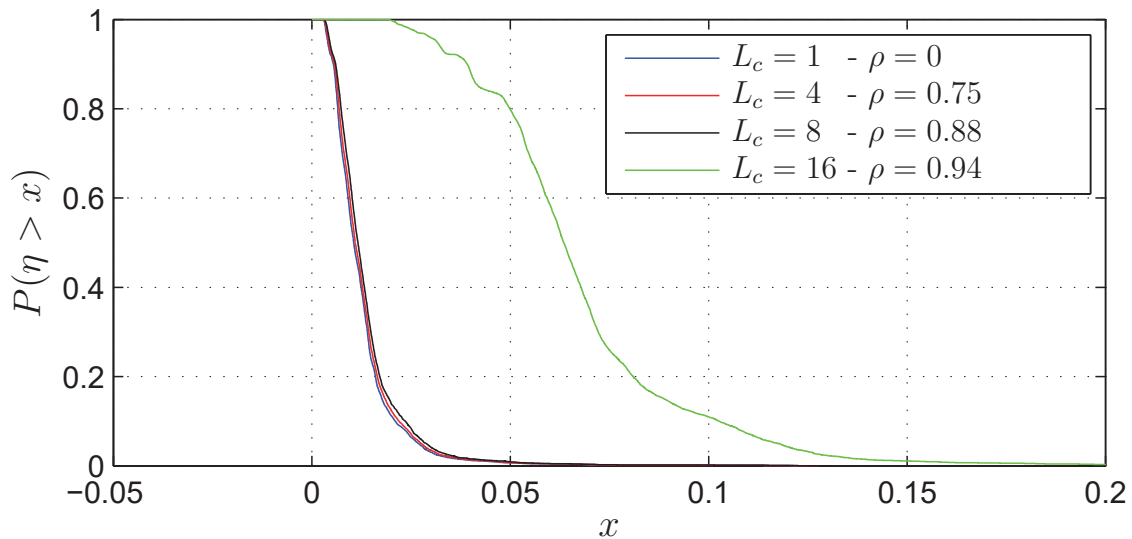


Figure 35: The CCDFs of the data rate loss ratio ( $\eta$ ) when the SCRA technique is applied to the OTFDM scheme with  $\mathcal{B} = 8$  and several  $L_c$  values.

trade off between data rate loss ratio and computational complexity reduction ratio.

Finally, but not the least, Fig. 36 shows the CCDF of the data rate loss ratio, when the SCRA technique is applied to OFDM and OTFDM schemes for frequency bands 1.7-30 MHz, 1.7-50 MHz and 1.7-100 MHz, which are, for the sake of simplicity, named  $W_{30}$ ,  $W_{50}$  and  $W_{100}$ , respectively. To obtain this curves,  $2N = 4096$  tiles are considered, meaning that the frequency resolution  $B_s$  is 14.6 kHz, 24.4 kHz and 48.8 kHz for  $W_{30}$ ,  $W_{50}$  and  $W_{100}$ , respectively. For all frequency bands the SCRA technique takes into account the minimal nSNR value in the chunk to ensure the SER constraint is not violated. Also, for the OTFDM scheme,  $L_c = \mathcal{B} = 8$  because it offers the highest computational complexity reduction ratio and the smallest data rate loss ratio, whereas for the OFDM scheme  $L_c = 8$ . The choice of  $L_c = 8$  for both schemes ensure that they achieves the same computational complexity reduction ratio, i.e.,  $\rho = 0.88$ . The curves in Fig. 36 show that the OTFDM scheme yields a considerable improvement in comparison with the OFDM scheme. As an example, for the frequency band  $W_{100}$ ,  $P(\eta > 0.05) = 0.009$  if the OTFDM scheme applies, whereas  $P(\eta > 0.05) = 0.797$  if the OFDM scheme applies. Furthermore, these curves show that the frequency band 1.7-100 MHz achieves more data rate loss ratio than the frequency bands 1.7-30 MHz and 1.7-50 MHz, which attain slightly different results.

#### 5.4 SUMMARY

The main conclusions of this chapter are summarized as follows:

- The OTFDM scheme can efficiently be implemented to transmit data in the passband or in the baseband with computational complexity similar to the OFDM scheme because the DOST can be efficiently implemented with the FFT. Also, the

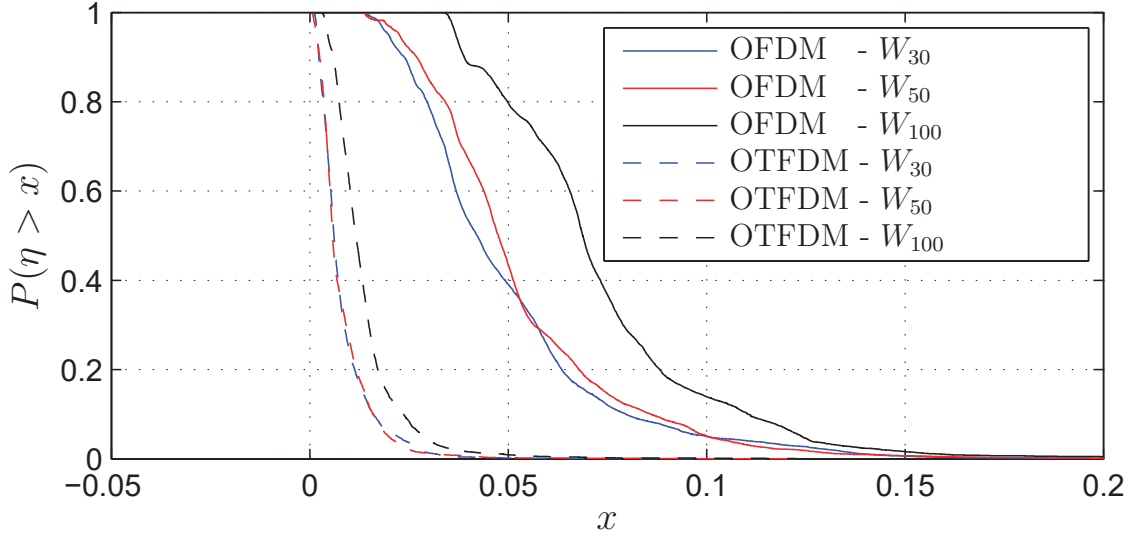


Figure 36: The CCDFs of the data rate loss ratio ( $\eta$ ) when the SCRA technique is applied using  $L_c = 8$  to the OFDM scheme and to the OTFDM scheme with  $\mathcal{B} = 8$ .

OTFDM can inherit the benefits associated with the circulant convolution matrix for implementing frequency domain equalization.

- If the CSI is not available at the transmitter side, then the OTFDM scheme can, under the presence of NBI components, offer better SER performance than the OFDM scheme, whereas it can achieve worse SER performance than the OFDM scheme for the additive noise composed of impulsive components and high  $E_b/N_0$ .
- The OTFDM scheme always achieves worse data rate in comparison with the OFDM scheme when the optimal resource allocation technique applies. However, the use of the SCRA technique results in an expressive reduction of the data rate loss ratio in comparison with the use of the SCRA technique together with the OFDM scheme, if the same computational complexity reduction applies.

## 6 CONCLUSIONS

This thesis proposed techniques to reduce the computational complexity of resource allocation technique in multicarrier-based PLC systems, since the optimal resource allocation technique is unfeasible in practical multicarrier-based PLC systems. Furthermore, this thesis proposes a novel multicarrier scheme, which offers a considerable computational complexity reduction of resource allocation techniques that takes into account the existent relationship among the microslots and among the subchannels.

Chapter 2 showed, based on a measurement campaign carried out on indoor and low-voltage electric power grids, that nm-SNR and data rate in microslots are cyclostationary random processes. Thereafter, it introduced a resource allocation technique that exploits the cyclostationary behavior of PLC channel to trade computational complexity reduction and data rate loss. The novelty in the proposed technique is the fact that it exploits the relationship among microslots within a cycle of the mains signal (**case #1**), among cycles of the mains signal (**case #2**), and the combination of them altogether (**case #3**). Performance analyses showed that the best results in terms of data rate loss ratio and computational complexity reduction ratio are attained with **case #2** and **case #3**. Additionally, Chapter 2 verified that the data rate offered with  $\Upsilon[m] = \bar{\gamma}[m]$  is very close to that ones obtained when  $\Upsilon[m] = R^o[m]$ . Therefore, the use of  $\Upsilon[m] = \bar{\gamma}[m]$  is strongly recommended, because it demands less computational complexity. Additionally, a comparison analysis showed that the proposed technique can offer improvement of as much as 15% (in terms of data-rate loss ratio) over IEEE 1901 standard, considering sets of 8 microslots. Improvements in comparison with previous bit loading technique for LPTV channels were also reported. Additionally, the proposed technique with  $\alpha_1 = \alpha_2 = 1$  attains the same result (optimal data rate) provided by the  $2^{nd}$  bit loading technique described in [22].

Chapter 3 introduced the nSNR coherence bandwidth, which can be useful for proposing low computational complexity resource allocation techniques for OFDM-based PLC systems. First of all, this chapter brought the motivations for adopting such parameter instead of the coherence bandwidth for resource allocation purposes. Additionally, it discussed several numerical analyses based on measured data sets constituted by in-home, outdoor and hybrid PLC-wireless PLC channels to show that the proposed parameter is effective when PLC channels is impaired by a colored Gaussian random noise process. Moreover, it focused on statistical modeling the PDF of such parameter by taking into account three important frequency bands (1.7-30 MHz, 1.7-50 MHz and 1.7-100 Hz) and three types of PLC channels (in-home, outdoor and hybrid PLC-wireless).

Chapter 4 detailed a novel chunk-based resource allocation technique that is suitable for reducing the computational complexity and the signaling overhead associated

with the intensive use of the bit loading algorithm in PLC systems based on OFDM scheme. Also, it discusses two modes of choosing the chunk length/bandwidth: (i) constant chunk length/bandwidth, in which the chunk length/bandwidth has the same value regardless of the nSNR coherence bandwidth; (ii) adaptive chunk length/bandwidth, in which the chunk length/bandwidth depends on the nSNR coherence bandwidth and, as a consequence, the chunk length/bandwidth may change every time that a new estimate of the nSNR is provided. Furthermore, this chapter investigated the data rate loss and the SER performance of the SCRA technique for different ways of choosing the representative nSNR of a chunk (i.e. minimal, mean, median and maximum values of the nSNR belonging to the chunk). In sequel, it investigated the SCRA technique performance, when the coherence bandwidth controls the adaptive chunk length/bandwidth, and compares the use of  $B_{c,H}$  and  $B_{c,\bar{\gamma}}$ . Numerical analyses based on a data set, obtained in a measurement campaign carried out in several residences covering the frequency bands 1.7-30, 1.7-50, and 1.7-100 MHz, showed that the best way of choosing the representative nSNR of a chunk is to take the minimal nSNR belongs to the chunk, since it ensure the SER constraint is not violated, with the drawback of obtaining the highest data rate loss. Moreover, when the SCRA technique is adaptive, it can offer significant less data rate loss for a similar computational complexity reduction in comparison with constant chunk length/bandwidth mode. Furthermore, by choosing the chunk length/bandwidth (for constant mode) or the threshold  $\alpha$  (for adaptive mode), it is possible to obtain the best trade off between the data rate loss and the computational complexity reduction. The numerical analyses showed that the SCRA technique working as adaptive and being based on the nSNR coherence bandwidth is trustful, agreeing with Chapter 3, since the SCRA technique offers smaller performance losses in terms of data rate loss than based on the coherence bandwidth.

Chapter 5 proposed a new multicarrier scheme (OTFDM scheme) and its hermitian symmetric variation to cover both baseband and passband data communications. This new scheme is based on the DOST, which is a time-frequency orthogonal transform. In this scheme, the information to be transmitted during an OTFDM symbol is allocated in orthogonal tiles of the time-frequency domain. These tiles can be less localized in the frequency domain and more localized in the time domain than the tiles of the OFDM scheme. The performance analyses shows that if the CSI is not available at the transmitter sides, then the OTFDM scheme achieves, compared with the OFDM scheme, the same SER performance when the additive noise is modeled as AWGN; better SER performance when the additive noise is composed of NBI components; and worse SER performance when the additive noise is composed of impulsive noise. On the other hand, if the CSI is available at the transmitter sides, then the SCRA technique together with the OTFDM scheme yields smaller data rate loss (with the same computational complexity reduction) than the SCRA technique together with the OFDM scheme.

## 6.1 FUTURE WORKS

Future efforts can be addressed in order to:

- Analyze the performance of the SCRA technique for outdoor PLC channels and hybrid PLC-wireless channels. Also, it could be useful to propose a variation of the SCRA technique considering chunk with different length/bandwidth.
- Analyze the performance of the TCRA and SCRA techniques applied together, when in-home, outdoor and hybrid PLC-wireless channels are considered.
- Propose techniques to improve the SER performance of the OTFDM scheme impaired by impulsive noise.
- Propose an optimal tile geometry to be used in PLC systems based on OTFDM scheme.

## REFERENCES

- [1] S. Galli, A. Scaglione, and Z. Wang, "For the grid and through the grid: The role of power line communications in the smart grid," *Proceedings of the IEEE*, vol. 99, no. 6, pp. 998–1027, Jun. 2011.
- [2] S.-G. Yoon, S. Jang, Y.-H. Kim, and S. Bahk, "Opportunistic routing for smart grid with power line communication access networks," *IEEE Trans. on Smart Grid*, vol. 5, no. 1, pp. 303–311, Jan. 2014.
- [3] W. Liu, H. Widmer, and P. Raffin, "Broadband PLC access systems and field deployment in european power line networks," *IEEE Communications Magazine*, vol. 41, no. 5, pp. 114–118, May 2003.
- [4] D. P. F. Moller and H. Vakilzadian, "Ubiquitous networks: Power line communication and internet of things in smart home environments," in *Proc. IEEE International Conference on Electro/Information Technology*, Jun. 2014, pp. 596–601.
- [5] H. C. Hsieh and C. H. Lai, "Internet of things architecture based on integrated PLC and 3G communication networks," in *Proc. IEEE 17th International Conference on Parallel and Distributed Systems*, Dec. 2011, pp. 853–856.
- [6] S. Baig and N. D. Gohar, "A discrete multitone transceiver at the heart of the PHY layer of an in-home power line communication local-area network," *IEEE Communications Magazine*, vol. 41, no. 4, pp. 48–53, Apr. 2003.
- [7] R. Nakkeeran and A. Rajesh, "Performance analysis of powerline communication for local area networking," in *Proc. International Conference on Control, Automation, Communication and Energy Conservation*, Jun. 2009, pp. 1–5.
- [8] Y. H. Kim, "Multipath parameter estimation for PLC channels using the GESE algorithm," *IEEE Trans. on Power Delivery*, vol. 25, no. 4, pp. 2339–2345, Oct. 2010.
- [9] G. S., H. B. Celebi, and H. Arslan, "Statistical characterization of the paths in multipath plc channels," *IEEE Trans. on Power Delivery*, vol. 26, no. 1, pp. 181–187, Jan. 2011.
- [10] M. Zimmermann and K. Dostert, "Analysis and modeling of impulsive noise in broadband powerline communications," *IEEE Trans. on Electromagnetic Compatibility*, vol. 44, no. 1, pp. 249–258, Feb. 2002.
- [11] Y. H. Ma, P. L. So, and E. Gunawan, "Performance analysis of OFDM systems for broadband power line communications under impulsive noise and multipath effects," *IEEE Trans. on Power Delivery*, vol. 20, no. 2, pp. 674–682, Apr. 2005.
- [12] M. Gotz, M. Rapp, and K. Dostert, "Power line channel characteristics and their effect on communication system design," *IEEE Communications Magazine*, vol. 42, no. 4, pp. 78–86, Apr. 2004.
- [13] A. M. Tonello, F. Versolatto, and A. Pittolo, "In-home power line communication channel: Statistical characterization," *IEEE Trans. on Communications*, vol. 62, no. 6, pp. 2096–2106, Jun. 2014.

- [14] A. M. Tonello, F. Versolatto, B. Béjar, and S. Zazo, “A fitting algorithm for random modeling the PLC channel,” *IEEE Trans. on Power Delivery*, vol. 27, no. 3, pp. 1477–1484, Jul. 2012.
- [15] S. Barmada, A. Musolino, and M. Raugi, “Innovative model for time-varying power line communication channel response evaluation,” *IEEE Journal on Selected Areas in Communications*, vol. 24, no. 7, pp. 1317–1326, Jul. 2006.
- [16] M. Tlich, A. Zeddami, F. Moulin, and F. Gauthier, “Indoor power-line communications channel characterization up to 100 mhz - part II: Time-frequency analysis,” *IEEE Trans. on Power Delivery*, vol. 23, no. 3, pp. 1402–1409, Jul. 2008.
- [17] F. Versolatto and A. M. Tonello, “On the relation between geometrical distance and channel statistics in in-home PLC networks,” in *Proc. 16th IEEE International Symposium on Power Line Communications and Its Applications*, Mar. 2012, pp. 280–285.
- [18] X. Cheng, R. Cao, and L. Yang, “Relay-aided amplify-and-forward powerline communications,” *IEEE Trans. on Smart Grid*, vol. 4, no. 1, pp. 265–272, Mar. 2013.
- [19] M. V. Ribeiro, “Técnicas de processamento de sinais aplicadas à transmissão de dados via rede elétrica e ao monitoramento da qualidade da energia elétrica,” Ph.D. dissertation, UNICAMP, 2005.
- [20] S. Barmada, A. Musolino, M. Raugi, R. Rizzo, and M. Tucci, “A wavelet based method for the analysis of impulsive noise due to switch commutations in power line communication (PLC) systems,” *IEEE Trans. on Smart Grid*, vol. 2, no. 1, pp. 92–101, Mar. 2011.
- [21] M. A. Tunc, E. Perrins, and L. Lampe, “Reduced complexity LPTV-aware bit loading for channel adaptation in broadband PLC,” in *Proc. IEEE International Symposium on Power Line Communications and Its Applications*, Mar. 2012, pp. 206–211.
- [22] M. A. Tunc, E. Perrins, and L. Lampe, “Optimal LPTV-aware bit loading in broadband PLC,” *IEEE Trans. on Communications*, vol. 61, no. 12, pp. 5152–5162, Dec. 2013.
- [23] K.-H. Kim, H.-B. Lee, Y.-H. Kim, and S.-C. Kim, “Channel adaptation for time-varying powerline channel and noise synchronized with AC cycle,” in *Proc. IEEE International Symposium on Power Line Communications and Its Applications*, Mar. 2009, pp. 250–254.
- [24] D. Chariag, D. Guezgouz, J. C. Le Bunetel, and Y. Raingeaud, “Modeling and simulation of temporal variation of channel and noise in indoor power-line network,” *IEEE Trans. on Power Delivery*, vol. 27, no. 4, pp. 1800–1808, Oct. 2012.
- [25] S. Katar, B. Mashbum, K. Afkhamie, H. Latchman, and R. Newrnan, “Channel adaptation based on cyclo-stationary noise characteristics in PLC systems,” in *Proc. IEEE International Symposium on Power Line Communications and Its Applications*, Mar. 2006, pp. 16–21.

- [26] N. Sawada, T. Yamazato, and M. Katayama, “Bit and power allocation for power-line communications under nonwhite and cyclostationary noise environment,” in *Proc. IEEE International Symposium on Power Line Communications and Its Applications*, Mar. 2009, pp. 307–312.
- [27] C. Chen, Y. Chen, N. Ding, Y. Wang, J.-C. Lin, X. Zeng, and D. Huang, “Accurate sampling timing acquisition for baseband OFDM power-line communication in non-gaussian noise,” *IEEE Trans. on Communications*, vol. 61, no. 4, pp. 1608–1620, Apr. 2013.
- [28] M. V. Ribeiro, G. R. Colen, F. P. V. de Campos, Z. Quan, and H. V. Poor, “Clustered-orthogonal frequency division multiplexing for power line communication: When is it beneficial?” *IET Communications*, vol. 8, no. 13, pp. 2336–2347, Sept. 2014.
- [29] T. Shongwe, V. Papilaya, and A. Vinck, “Narrow-band interference model for ofdm systems for powerline communications,” in *Proc. IEEE International Symposium on Power Line Communications and Its Applications*, Mar. 2013, pp. 268–272.
- [30] C. Luo, S. Cheng, L. Xiong, J. Nguimbis, Y. Zhang, and J. Ma, “A nonlinear equalization method based on multilayer perceptron for OFDM power-line communication,” *IEEE Trans. on Power Delivery*, vol. 20, no. 4, pp. 2437–2442, Oct. 2005.
- [31] P. Achaichia, M. L. Bot, and P. Siohan, “OFDM/OQAM: A solution to efficiently increase the capacity of future PLC networks,” *IEEE Trans. on Power Delivery*, vol. 26, no. 4, pp. 2443–2455, Oct. 2011.
- [32] H. Xu and S. Yang, “A loosely synchronous-coded OFDM system for power-line communications in home networks,” *IEEE Trans. on Power Delivery*, vol. 21, no. 4, pp. 1912–1918, Oct. 2006.
- [33] L. Dai, J. Fu, and J. Wang, “LDPC coded TDS-OFDM for PLC systems,” *Tsinghua Science and Technology*, vol. 15, no. 3, pp. 312–318, Jun. 2010.
- [34] A. A. M. Picorone, T. R. Oliveira, and M. V. Ribeiro, “PLC channel estimation based on pilots signal for OFDM modulation: A review,” *IEEE Latin America Transactions*, vol. 12, no. 4, pp. 580–589, Jun. 2014.
- [35] S. Morosi, D. Marabissi, E. Del Re, R. Fantacci, and N. Del Santo, “A rate adaptive bit-loading algorithm for in-building power-line communications based on DMT-modulated systems,” *IEEE Trans. on Power Delivery*, vol. 21, no. 4, pp. 1892–1897, Oct. 2006.
- [36] M. V. Ribeiro, R. R. Lopes, J. M. T. Romano, and C. A. Duque, “Impulse noise mitigation based on computational intelligence for improved bit rate in PLC-DMT,” *IEEE Trans. on Power Delivery*, vol. 21, no. 1, pp. 94–101, Jan. 2006.
- [37] H. Lin and P. Siohan, “OFDM/OQAM with hermitian symmetry: Design and performance for baseband communication,” in *Proc. IEEE International Conference on Communications*, May 2008, pp. 652–656.
- [38] G. R. Colen, “Sistemas clustered-OFDM SISO e MIMO para power line communication,” Master’s thesis, UFJF, 2012.

- [39] J. M. Cioffi, *Chapter 4: Multi-channel modulation*, accessed in July 2015. [Online]. Available: <http://web.stanford.edu/group/cioffi/book/chap4.pdf>
- [40] N. Papandreou and T. Antonakopoulos, "Resource allocation management for indoor power-line communications systems," *IEEE Trans. on Power Delivery*, vol. 22, no. 2, pp. 893–903, Apr. 2007.
- [41] N. Papandreou and T. Antonakopoulos, "Fair resource allocation with improved diversity performance for indoor power-line networks," *IEEE Trans. on Power Delivery*, vol. 22, no. 4, pp. 2575–2576, Oct. 2007.
- [42] S. D'Alessandro, A. M. Tonello, and L. Lampe, "Bit-loading algorithms for OFDM with adaptive cyclic prefix length in PLC channels," in *Proc. IEEE International Symposium on Power Line Communications and Its Applications*, Mar. 2009, pp. 177–181.
- [43] I. Isha, P. Rana, and R. Saini, "Performance of different bit loading algorithms for OFDM at PLC channel," in *Proc. 2nd International Conference on Advanced Computing Communication Technologies*, Jan. 2012, pp. 486–489.
- [44] Z. Xu, M. Zhai, and Y. Zhao, "Optimal resource allocation based on resource factor for power-line communication systems," *IEEE Trans. on Power Delivery*, vol. 25, no. 2, pp. 657–666, Apr. 2010.
- [45] T. N. Vo, K. Amis, T. Chonavel, and P. Siohan, "Achievable throughput optimization in OFDM systems in the presence of interference and its application to power line networks," *IEEE Trans. on Communications*, vol. 62, no. 5, pp. 1704–1715, May 2014.
- [46] K. S. Al-Mawali, A. Z. Sadik, and Z. M. Hussain, "Simple discrete bit-loading for OFDM systems in power line communications," in *Proc. IEEE International Symposium on Power Line Communications and Its Applications*, Apr. 2011, pp. 267–270.
- [47] S. Honda, D. Umehara, T. Hayasaki, S. Denno, and M. Morikura, "A fast bit loading algorithm synchronized with commercial power supply for in-home PLC systems," in *Proc. IEEE International Symposium on Power Line Communications and Its Applications*, Apr. 2008, pp. 336–341.
- [48] U. Noreen and S. Baig, "Modified incremental bit allocation algorithm for powerline communication in smart grids," in *Proc. 1st International Conference on Communications, Signal Processing, and their Applications*, Feb. 2013, pp. 1–6.
- [49] A. M. Wyglinski, F. Labeau, and P. Kabal, "Bit loading with BER-constraint for multicarrier systems," *IEEE Trans. on Wireless Communications*, vol. 4, no. 4, pp. 1383–1387, July 2005.
- [50] A. Maiga, J. Baudais, and J. Helard, "An efficient bit-loading algorithm with peak BER constraint for the band-extended PLC," in *Proc. International Conference on Telecommunications*, May 2009, pp. 292–297.
- [51] F. J. C. Corripio, J. A. C. Arrabal, L. D. del Rio, and J. T. E. Munoz, "Analysis of the cyclic short-term variation of indoor power line channels," *IEEE Journal on Selected Areas in Communications*, vol. 24, no. 7, pp. 1327–1338, Jul. 2006.

- [52] A. Musolino, M. Raugi, and M. Tucci, "Cyclic short-time varying channel estimation in ofdm power-line communication," *IEEE Trans. on Power Delivery*, vol. 23, no. 1, pp. 157–163, Jan. 2008.
- [53] *IEEE standard for broadband over power line networks: Medium access control and physical layer specifications (IEEE Std. 1901)*, IEEE Communications Society Std., Dec. 2010.
- [54] T. M. Cover and J. A. Thomas, *Elements of information theory*. Wiley-Interscience, 2006.
- [55] J. Campello, "Optimal discrete bit loading for multicarrier modulation systems," in *Proc. IEEE International Symposium on Information Theory*, Aug. 1998, p. 193.
- [56] H. Zhu and J. Wang, "Chunk-based resource allocation in OFDMA systems - part I: Chunk allocation," *IEEE Trans. on Communications*, vol. 57, no. 9, pp. 2734–2744, Sept. 2009.
- [57] H. Zhu and J. Wang, "Chunk-based resource allocation in OFDMA systems - part II: Joint chunk, power and bit allocation," *IEEE Trans. on Communications*, vol. 60, no. 2, pp. 499–509, Feb. 2012.
- [58] T. R. Oliveira, "The characterization of hybrid PLC-wireless and PLC channels in the frequency band between 1.7 and 100 MHz for data communication," Ph.D. dissertation, Federal University of Juiz de Fora (UFJF), Mar. 2015.
- [59] T. R. Oliveira, C. A. G. Marques, M. S. Pereira, S. L. Netto, and M. V. Ribeiro, "The characterization of hybrid PLC-wireless channels: A preliminary analysis," in *Proc. IEEE International Symposium on Power Line Communications and Its Applications*, Mar. 2013, pp. 98–102.
- [60] M. Antoniali and A. M. Tonello, "Measurement and characterization of load impedances in home power line grids," *IEEE Trans. on Instrumentation and Measurement*, vol. 63, no. 3, pp. 548–556, Mar. 2014.
- [61] ANATEL. (2009) Brazilian resolution for PLC. [Online]. Available: <http://legislacao.anatel.gov.br/resolucoes/2009/101-resolucao-527>
- [62] G. R. Colen, C. A. G. Marques, T. R. Oliveira, F. P. V. de Campos, and M. Ribeiro, "Measurement setup for characterizing low-voltage and outdoor electric distribution grids for PLC systems," in *Proc. IEEE PES Conference On Innovative Smart Grid Technologies Latin America*, Apr. 2013, pp. 1–5.
- [63] T. R. Oliveira, C. A. G. Marques, W. A. Finamore, S. L. Netto, and M. V. Ribeiro, "A methodology for estimating frequency responses of electric power grids," *Journal of Control, Automation and Electrical Systems*, vol. 25, no. 6, pp. 720–731, Sept. 2014.
- [64] C. R. B. Cabral, V. H. Lachos, and C. B. Zeller, "Multivariate measurement error models using finite mixtures of skew-student distributions," *Journal of Multivariate Analysis*, vol. 124, no. 0, pp. 179–198, Feb. 2014.

- [65] A. A. M. Picorone, “Comunicação digital em canais PLC: Técnicas de transmissão, detecção e caracterização de canais PLC outdoor brasileiros,” Ph.D. dissertation, Federal University of Juiz de Fora (UFJF), Aug. 2014.
- [66] O. G. Hooijen, “On the channel capacity of the residential power circuit used as a digital communications medium,” *IEEE Communications Letters*, vol. 2, no. 10, pp. 267–268, Oct. 1998.
- [67] J. M. Ciofli, “A multicarrier primer,” *ANSI T1E1.4*, vol. 4, pp. 91–157, 1991.
- [68] J. Campello, “Practical bit loading for DMT,” in *Proc. IEEE International Conference on Communications*, vol. 2, Jun. 1999, pp. 801–805.
- [69] R. Stockwell, “A basis for efficient representation of the s-transform,” *Digital Signal Processing*, vol. 17, no. 1, pp. 371–393, Jan. 2007.
- [70] A. A. M. Picorone, L. R. Amado, and M. V. Ribeiro, “Linear and periodically time-varying PLC channels estimation in the presence of impulsive noise,” in *Proc. IEEE International Symposium on Power Line Communications and Its Applications*, Mar. 2010, pp. 255–260.
- [71] J. Proakis, *Digital Communications*. McGraw-Hill, 1995.
- [72] M. Tuchler, A. C. Singer, and R. Koetter, “Minimum mean squared error equalization using a priori information,” *IEEE Trans. on Signal Processing*, vol. 50, no. 3, pp. 673–683, Mar 2002.
- [73] Y. Wang, “Efficient stockwell transform with applications to image processing,” Ph.D. dissertation, University of Waterloo, 2011.
- [74] Y. Wang and J. Orchard, “Fast discrete orthonormal Stockwell transform,” *SIAM J. Sci. Comput.*, vol. 31, no. 5, pp. 4000–4012, Nov. 2009.
- [75] Y. Wang and J. Orchard, “On the use of the stockwell transform for image compression,” in *Proc. SPIE*, vol. 7245, Nov 2009, pp. 724 504–724 504–7.
- [76] B. Nithya, Y. B. Sankari, K. Manikantan, and S. Ramachandran, “Discrete orthonormal Stockwell transform based feature extraction for pose invariant face recognition,” *Procedia Computer Science*, vol. 45, pp. 290–299, 2015.
- [77] Y. Wang and J. Orchard, “The discrete orthonormal Stockwell transform for image restoration,” in *Proc. 16th IEEE International Conference on Image Processing*, Nov 2009, pp. 2761–2764.
- [78] J. Wang, T. Chen, and B. Huang, “On spectral theory of cyclostationary signals in multirate systems,” *IEEE Trans. on Signal Processing*, vol. 53, no. 7, pp. 2421–2431, Jul. 2005.

## Appendix A – A Proof of the Cyclostationarity of $\Upsilon[m]$

Lets the cyclostationarity of random process be defined by [78],

$$C'_{\Upsilon[m]}[\tau] \triangleq C'_{\Upsilon[m]}[\tau + L] \quad (\text{A.1})$$

and

$$\mathbb{E}\{\Upsilon[m]\} = \mathbb{E}\{\Upsilon[m + L]\}, \quad (\text{A.2})$$

where  $C'_{\Upsilon[m]}[\tau] = \mathbb{E}\{\Upsilon[m]\Upsilon[m + \tau]\}$  and  $L$  is the smallest lag that makes (A.1) and (A.2) true.

Figs. 37 and 38 show estimates of  $C'_{\Upsilon[m]}[\tau]$ ,  $0 \leq \tau < 99$  for  $\Upsilon[m] = \bar{\gamma}[m]$  and  $\Upsilon[m] = R^o[m]$ , respectively, when measures corresponding to four cycles of the mains signal are considered. Moreover these graphs show that (A.1) can be satisfied if  $L = M = 25$ . The evidence that  $M$  is the smallest lag that verify cyclostationarity characteristic of  $\Upsilon[m]$  is the fact that  $\mathbb{E}\{\bar{\gamma}[m]\} \cong \mathbb{E}\{\bar{\gamma}[m + M]\} \cong 20$  dB,  $\mathbb{E}\{R^o[m]\} \cong \mathbb{E}\{R^o[m + M]\} \cong 5.1$  Mbps.

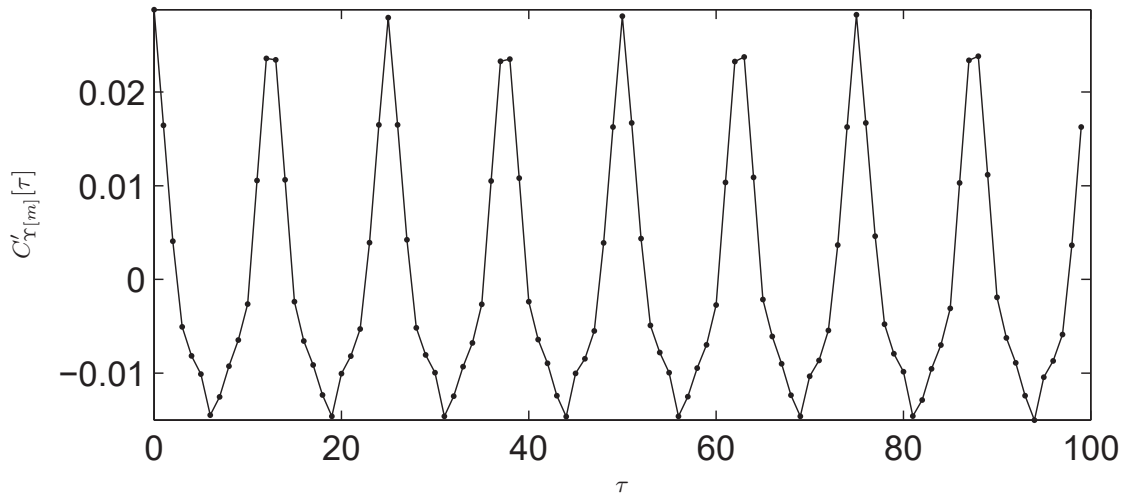


Figure 37:  $C'_{\Upsilon[m]}[\tau]$  for  $\Upsilon[m] = \bar{\gamma}[m]$  during 4 cycles of the mains signal ( $M = 25$ ).

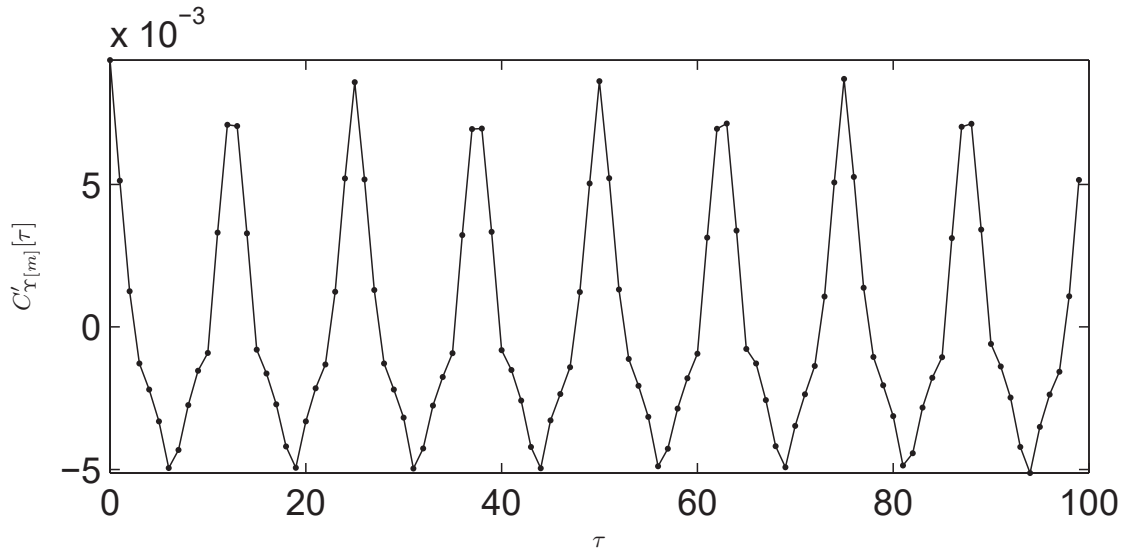


Figure 38:  $C''_{\Upsilon[m]}[\tau]$  for  $\Upsilon[m] = R^o[m]$  during 4 cycles of the mains signal ( $M = 25$ ).

## Appendix B – The Estimated Parameters

Tables 10 and 11 list estimates of parameters of, respectively, Gaussian mixture and single-component distributions used to model the histogram of the nSNR coherence bandwidth, which ones are shown in Figs. 14 to 17. For the Gaussian mixture distributions, the tables provide  $\mu$ ,  $\sigma$  and component proportion for each Gaussian component. The suffix after GMD refers to the number of Gaussian components, while the suffix after GC denotes the index of the Gaussian component. For the single-component distributions, the table lists the estimates of their respective parameters ( $a$  and  $b$  for Gamma,  $\mu$  and  $\lambda$  for Inverse Gaussian,  $\mu$  and  $\sigma$  for Log-Normal and Log-Logistic, and  $\mu$  and  $\omega$  for Nakagami).

Table 10: The parameter estimates of the Gaussian mixture distributions.

In-home					
W <sub>30</sub>					
Distribution	Parameter	GC 1	GC 2	GC 3	GC 4
GMD 4	$\mu$	405665.17 $\pm$ 1.22%	2363439.33 $\pm$ 0.28%	779804.48 $\pm$ 1.44%	244024.93 $\pm$ 0.82%
	$\sigma$	12065770799.53 $\pm$ 5.59%	5457425740.08 $\pm$ 12.70%	84226908616.14 $\pm$ 3.50%	1352609439.37 $\pm$ 11.40%
	Proportion	0.45 $\pm$ 3.40%	0.02 $\pm$ 8.90%	0.33 $\pm$ 3.62%	0.21
W <sub>50</sub>					
Distribution	Parameter	GC 1	GC 2	GC 3	GC 4
GMD 4	$\mu$	2243791.08 $\pm$ 0.28%	281185.49 $\pm$ 1.03%	566413.33 $\pm$ 1.17%	1091662.84 $\pm$ 1.80%
	$\sigma$	6289361478.76 $\pm$ 11.65%	2902636612.28 $\pm$ 8.55%	23711541616.54 $\pm$ 5.17%	50834144619.69 $\pm$ 10.34%
	Proportion	0.02 $\pm$ 7.94%	0.29 $\pm$ 4.40%	0.51 $\pm$ 3.13%	0.18
W <sub>100</sub>					
Distribution	Parameter	GC 1	GC 2	GC 3	GC 4
GMD 4	$\mu$	311429.34 $\pm$ 1.72%	2129913.51 $\pm$ 5.55%	1233670.41 $\pm$ 1.03%	658857.31 $\pm$ 1.45%
	$\sigma$	7694094954.02 $\pm$ 8.00%	481911733630.58 $\pm$ 20.91%	23757799686.15 $\pm$ 11.30%	24279417727.67 $\pm$ 13.66%
	Proportion	0.38 $\pm$ 5.72%	0.03 $\pm$ 11.81%	0.12 $\pm$ 5.96%	0.46
Hybrid (PLC-to-wireless)					
W <sub>50</sub>					
Distribution	Parameter	GC 1	GC 2	GC 3	GC 4
GMD 4	$\mu$	177101.60 $\pm$ 2.54%	733815.73 $\pm$ 0.93%	103228.99 $\pm$ 1.09%	394763.10 $\pm$ 0.55%
	$\sigma$	2534210516.76 $\pm$ 7.16%	70600958119.23 $\pm$ 2.73%	1163246488.53 $\pm$ 3.33%	5413040056.04 $\pm$ 6.96%
	Proportion	0.21 $\pm$ 7.86%	0.25 $\pm$ 2.02%	0.37 $\pm$ 4.54%	0.18
W <sub>100</sub>					
Distribution	Parameter	GC 1	GC 2	GC 3	GC 4
GMD 4	$\mu$	183537.30 $\pm$ 2.31%	396834.27 $\pm$ 0.42%	108330.59 $\pm$ 0.72%	705583.08 $\pm$ 0.96%
	$\sigma$	2601107669.12 $\pm$ 7.85%	4207028376.56 $\pm$ 6.61%	1079861879.50 $\pm$ 2.72%	66972086902.23 $\pm$ 2.68%
	Proportion	0.18 $\pm$ 7.18%	0.19 $\pm$ 2.88%	0.39 $\pm$ 3.46%	0.25
Hybrid (wireless-to-PLC)					
Distribution	Parameter	GC 1	GC 2	GC 3	GC 4
GMD 4	$\mu$	596856.36 $\pm$ 0.68%	1077971.56 $\pm$ 1.46%	1938019.66 $\pm$ 3.83%	192670.23 $\pm$ 0.71%
	$\sigma$	37452906196.64 $\pm$ 3.20%	105409682227.80 $\pm$ 4.92%	669282873424.81 $\pm$ 8.12%	3328259647.23 $\pm$ 3.60%
	Proportion	0.50 $\pm$ 2.82%	0.32 $\pm$ 4.43%	0.02 $\pm$ 10.92%	0.15
W <sub>50</sub>					
Distribution	Parameter	GC 1	GC 2	GC 3	GC 4
GMD 4	$\mu$	790686.47 $\pm$ 3.14%	205093.59 $\pm$ 0.94%	1789278.97 $\pm$ 4.67%	1192231.08 $\pm$ 4.84%
	$\sigma$	76047665903.65 $\pm$ 8.01%	4147019864.33 $\pm$ 4.78%	330375794414.46 $\pm$ 7.60%	144548377255.56 $\pm$ 11.77%
	Proportion	0.46 $\pm$ 13.04%	0.12 $\pm$ 2.49%	0.09 $\pm$ 26.54%	0.34
W <sub>100</sub>					
Distribution	Parameter	GC 1	GC 2	GC 3	GC 4
GMD 4	$\mu$	1795671.03 $\pm$ 4.08%	195630.57 $\pm$ 1.12%	1264510.10 $\pm$ 3.72%	833432.77 $\pm$ 1.85%
	$\sigma$	388659474486.93 $\pm$ 7.71%	6936778610.52 $\pm$ 4.01%	149596966513.64 $\pm$ 9.44%	77066026509.54 $\pm$ 6.51%
	Proportion	0.07 $\pm$ 22.80%	0.14 $\pm$ 2.31%	0.30 $\pm$ 11.07%	0.48

Table 11: The parameter estimates of the single-component distributions.

<b>In-home</b>		
$W_{30}$		
Distribution	Parameter	Estimate
Inverse Gaussian	$\mu$	$530845.49 \pm 0.72\%$
	$\lambda$	$1455912.71 \pm 1.68\%$
$W_{50}$		
Distribution	Parameter	Estimate
Inverse Gaussian	$\mu$	$616365.03 \pm 0.72\%$
	$\lambda$	$1662207.20 \pm 1.68\%$
$W_{100}$		
Distribution	Parameter	Estimate
Log-Logistic	$\mu$	$13.19 \pm 0.06\%$
	$\sigma$	$0.35 \pm 0.97\%$
<b>Outdoor</b>		
$W_{30}$		
Distribution	Parameter	Estimate
Gamma	$a$	$7.26 \pm 0.87\%$
	$b$	$19103.43 \pm 0.90\%$
Nakagami	$\mu$	$2.04 \pm 0.82\%$
	$\omega$	$21743681099.54 \pm 0.44\%$
$W_{50}$		
Distribution	Parameter	Estimate
Gamma	$a$	$7.19 \pm 0.86\%$
	$b$	$19410.33 \pm 0.90\%$
Nakagami	$\mu$	$2.01 \pm 0.82\%$
	$\omega$	$22089784625.92 \pm 0.44\%$
$W_{100}$		
Distribution	Parameter	Estimate
Gamma	$a$	$6.80 \pm 0.86\%$
	$b$	$20301.10 \pm 0.90\%$
Nakagami	$\mu$	$1.92 \pm 0.82\%$
	$\omega$	$21723898422.92 \pm 0.45\%$
<b>Hybrid (PLC-to-wireless)</b>		
$W_{30}$		
Distribution	Parameter	Estimate
Inverse Gaussian	$\mu$	$177129.53 \pm 0.71\%$
	$\lambda$	$150163.05 \pm 0.92\%$
Log-Normal	$\mu$	$11.63 \pm 0.05\%$
	$\sigma$	$0.91 \pm 0.46\%$
$W_{50}$		
Distribution	Parameter	Estimate
Inverse Gaussian	$\mu$	$327836.83 \pm 0.67\%$
	$\lambda$	$312951.30 \pm 0.92\%$
$W_{100}$		
Distribution	Parameter	Estimate
Inverse Gaussian	$\mu$	$322498.26 \pm 0.63\%$
	$\lambda$	$343647.38 \pm 0.92\%$
<b>Hybrid (wireless-to-PLC)</b>		
$W_{30}$		
Distribution	Parameter	Estimate
Gamma	$a$	$2.63 \pm 0.87\%$
	$b$	$272950.03 \pm 0.96\%$
$W_{50}$		
Distribution	Parameter	Estimate
Nakagami	$\mu$	$0.89 \pm 0.80\%$
	$\omega$	$1155475154992.01 \pm 0.69\%$
$W_{100}$		
Distribution	Parameter	Estimate
Nakagami	$\mu$	$0.82 \pm 0.80\%$
	$\omega$	$1169725593056.27 \pm 0.72\%$

## Appendix C – Publications

The list of papers published during the doctoral period are as follows:

- M. V. Ribeiro, G. R. Colen, F. V. P. de Campos, Zhi Quan; H. V. Poor, “Clustered-orthogonal frequency division multiplexing for power line communication: when is it beneficial?,” *IET Communications*, vol. 8, no. 13, pp. 2336-2347, Sept. 2014.
- G. R. Colen, H. Schettino, D. Fernandes, L. M. Sirimarco, F. P. V. Campos, W. A. Finamore, H. A. Latchman, M. V. Ribeiro, “A temporal compressive resource allocation technique for complexity reduction in PLC transceivers,” *Trans. on Emerging Telecommunications Technologies*, 2015, online.
- G. R. Colen, L. G. de Oliveira, A. J. Han Vinck, M. V. Ribeiro, “A spectral compressive resource allocation technique for PLC systems,” *IEEE Trans. on Communication*, 2016, under review process.
- G. R. Colen, L. G. de Oliveira, A. A. M. Picorone, T. R. Oliveira, C. B. Zeller, A. J. Han Vinck, M. V. Ribeiro, “A new parameter to be considered in resource allocation for PLC systems,” *Trans. on Emerging Telecommunications Technologies*, 2016, to be submitted.
- G. R. Colen, M. V. Ribeiro, “An orthogonal time-frequency division multiplexing scheme for PLC systems,” *IEEE Trans. on Communication*, 2016, to be submitted.

The follow patent were required during the doctoral period:

- G. R. Colen, M. V. Ribeiro, F. P. V. de Campos, “Método de modulação e demodulação MIMO-HSOFDM de baixa complexidade para a comunicação MIMO de dados,” register number BR1020130106119, Brazil, Apr. 2013.

The list of conference papers published during the doctoral period are as follows:

- G. R. Colen, C. A. G. Marques, T. R. Oliveira, F. P. V. de Campos, M. V. Ribeiro, “Measurement setup for characterizing low-voltage and outdoor electric distribution grids for PLC systems,” in *Proc. IEEE PES Conference on Innovative Smart Grid Technologies Latin America*, Apr. 2013, pp. 1-5.
- G. R. Colen, W. A. Finamore, M. V. Ribeiro, “Traditional, lengthened and shortened LT codes comparison,” in *Proc. XXXI Simpósio Brasileiro de Telecomunicações*, Sept. 2013, pp. 1-5.

- G. R. Colen, M. V. Ribeiro, F. P. V. de Campos, T. R. Oliveira, A. A. M. Picorone, M. S. P. Facina, “Setup de medição para caracterização de redes de distribuição de energia elétrica externas para sistemas PLC,” in *Proc. Seminario Nacional de Distribuição de Energia Elétrica*, Nov. 2014, pp. 1-12.
- M. V. Ribeiro, F. P. V. Campos, G. R. Colen, H. V. Schettino, D. Fernandes, L. M. Sirimarco, V. Fernandes, A. A. M. Picorone, “A novel power line communication system for outdoor electric power grids,” in *Proc. IEEE International Symposium on Power Line Communications and its Applications*, Mar. 2015, pp. 1-6.
- G. R. Colen, F. P. V. de Campos, M. V. Ribeiro, H. A. Latchman, “A bit loading technique with reduced complexity for periodically time varying PLC channel,” in *Proc. IEEE International Symposium on Power Line Communications and its Applications*, Mar. 2015, pp. 1-5.
- G. R. Colen, T. M. Peixoto, V. Fernandes, M. V. Ribeiro, “A Frequency Domain Resource Allocation Technique with Reduced Complexity for PLC System,” in *Proc. XXXIII Simpósio Brasileiro de Telecomunicações*, Sept. 2015, pp. 1-4.
- A. J. H. Vinck, F. Rouissi, T. Shongwe, G. Colen, L. Giroto, “Impulse Noise and Narrowband PLC,” in *Proc. 9th Workshop on Power Line Communications*, Sept. 2015, pp. 1-4.
- L. G. de Oliveira, G. R. Colen, M. V. Ribeiro, A. J. H. Vinck, “Narrow-band interference error correction in coded OFDM-based PLC systems,” in *Proc. IEEE International Symposium on Power Line Communications and its Applications*, Mar. 2016, pp. 13-18.
- G. R. Colen, L. G. de Oliveira, A. J. H. Vinck, M. V. Ribeiro, “Resource allocation in OFDM-based PLC systems impaired by additive impulsive Gaussian noise,” in *Proc. IEEE International Symposium on Power Line Communications and its Applications*, Mar. 2016, pp. 70-75.